FAST METHODS FOR FULL-WAVE ELECTROMAGNETIC SIMULATIONS OF INTEGRATED CIRCUIT PACKAGE MODULES

A Dissertation
Presented to
The Academic Faculty

by

Narayanan T.V.

In Partial Fulfillment
of the Requirements for the Degree
Doctor of Philosophy in the
School of Electrical and Computer Engineering

Georgia Institute of Technology
August 2011

FAST METHODS FOR FULL-WAVE ELECTROMAGNETIC SIMULATIONS OF INTEGRATED CIRCUIT PACKAGE MODULES

Approved by:

Professor Madhavan Swaminathan,
Advisor
School of Electrical and Computer
Engineering
Georgia Institute of Technology

Professor Ioannis Papapolymerou
School of Electrical and Computer
Engineering
Georgia Institute of Technology

Professor Abhijit Chatterjee
School of Electrical and Computer
Engineering
Georgia Institute of Technology

Professor Andrew Peterson
School of Electrical and Computer
Engineering
Georgia Institute of Technology

Professor Suresh Sitaraman
School of Mechanical Engineering
Georgia Institute of Technology

Date Approved: April 18,2011

To my brother,

and parents.

ACKNOWLEDGEMENTS

TABLE OF CONTENTS

LIST OF TABLES

LIST OF FIGURES

xiii

xiv

CHAPTER I

INTRODUCTION

1.1 Background

The design of modern day integrated circuit (IC) packages is increasingly becoming complex. The initial trend was towards increasing computing capabilities, and this resulted in a drive in two directions: 1) personal computing affording increasing avenues at an individual consumer level, and 2) high performance computing, which focused on needs of supercomputing/enterprise computing. In recent times, however, the primary driver of innovation in the electronics area has been to reach goals of 1) miniaturization and 2) proving a multi-functional platform. This is reflected in Fig. 1. The drive towards smaller, reliable and low-cost solutions to functional integration has resulted in a variety of architectures being proposed, e.g., system-on-chip (SoC), system-in-package (SiP), and system-on-package (SoP) (as shown in Fig. 2), with the latest trend being the three-dimensional (3D) integration of functional modules, shown in Fig. 3.

1.2 Motivation

The nature of the novel and complex geometries involved in these architectures, along with the various relevant local and non-local electromagnetic interactions pose a significant design problem. The simulation of such packages involves the mathematical processing of large linear systems arising from the passive component models of interconnects and packages. The fast and reliable full-wave simulation of such modules is therefore a necessity to speed up the design cycle time, while maintaining accuracy of the results.
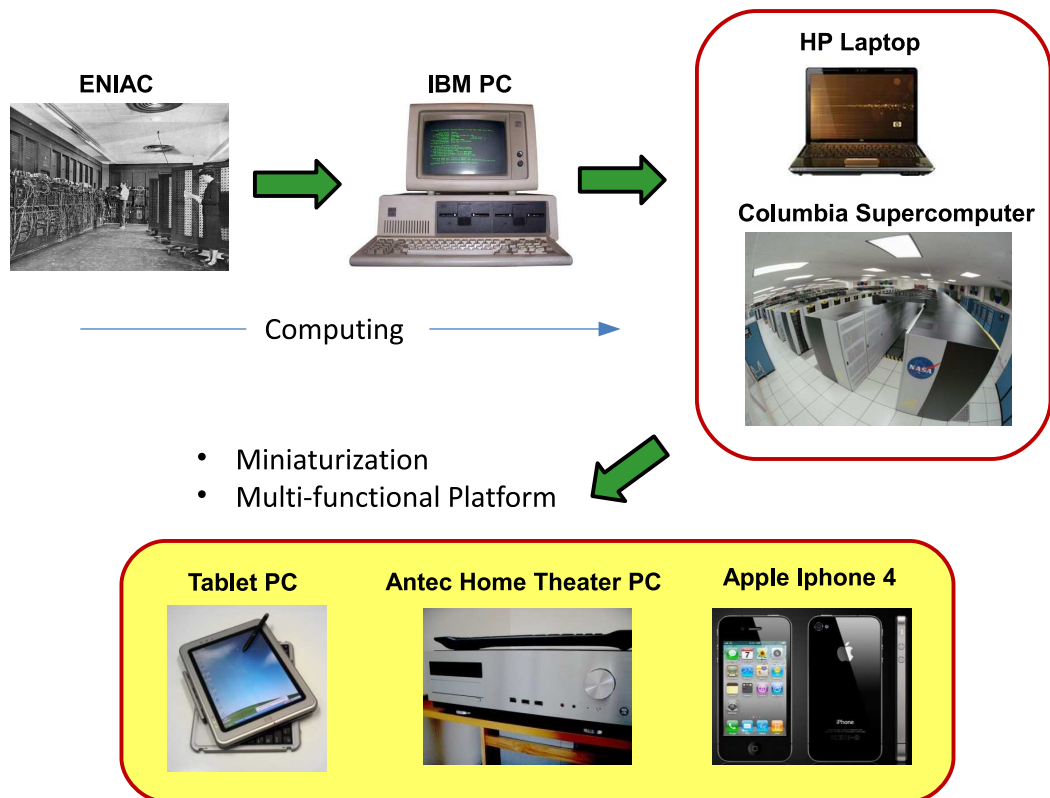
Figure 1: The progress in the integrated circuits area from the initial computing days up until today, and the primary drivers of the market.
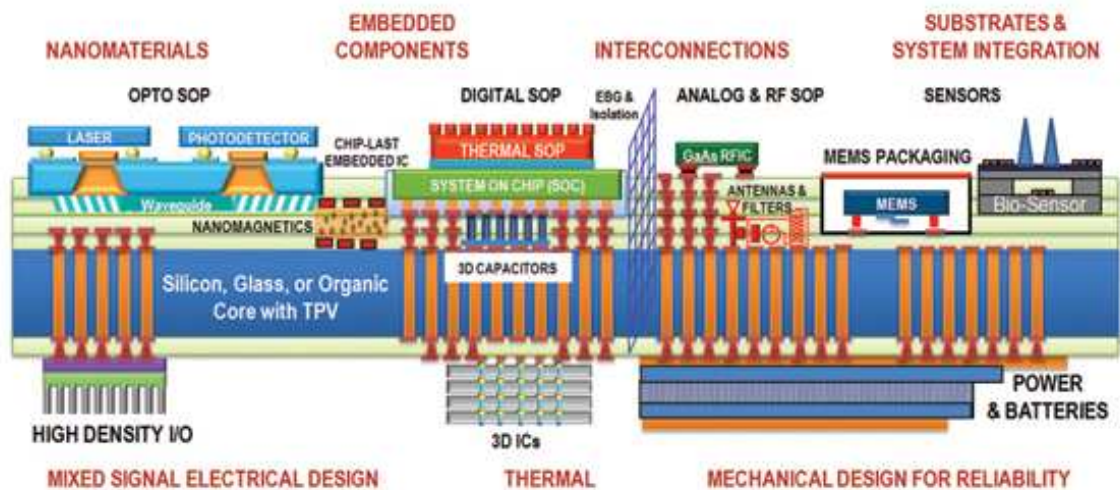
Figure 2: System on Package (SoP) integration. (Courtesy: Packaging Research Center, Georgia Institute of Technology.)

The 3D full-wave simulations, based on discretization of Maxwell's equations, forms an important and highly accurate class of solutions to such problems. In the
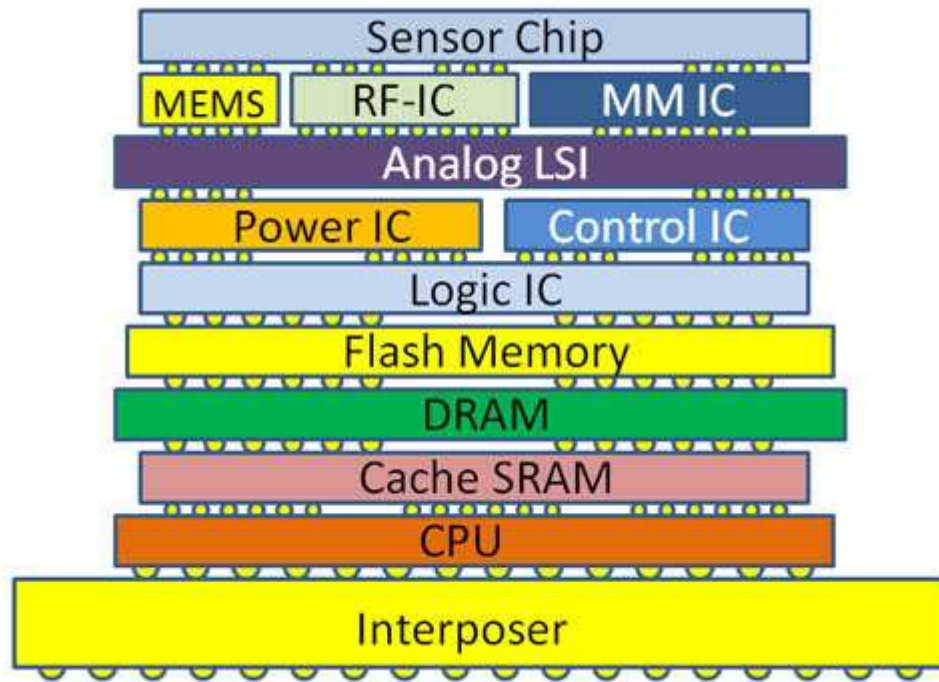
Figure 3: 3D multifunctional vertical integration. (Courtesy: Interconnect and Packaging Center, Georgia Institute of Technology.)

frequency domain, the solution involves the inversion of a large matrix, expensive in terms of both, time and memory. In the time-domain, the solution may be formulated as an explicit method, thus reducing the memory problem. However, the issue of long-time simulation still remains. In terms of the design cycle of IC packages, represented in Fig. 4, there is a need for fast frequency sweep full-wave analysis of IC package structures in the 3D simulation step. An approach relying on fast characterization of package modules based on model order reduction (MOR) is suggested in this dissertation as an intermediate step. The full-wave simulation of the complete system is retained, but is instead carried out using the fast methods (e.g., MOR) before the final test structures are sent for fabrication. The modified design flow is shown in Fig. 5.

3
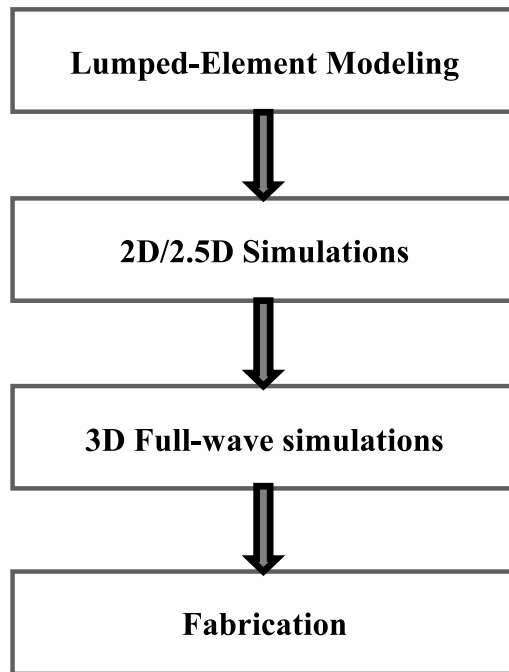
Figure 4: Hierarchical design flow for the simulation and testing of semiconductor package modules
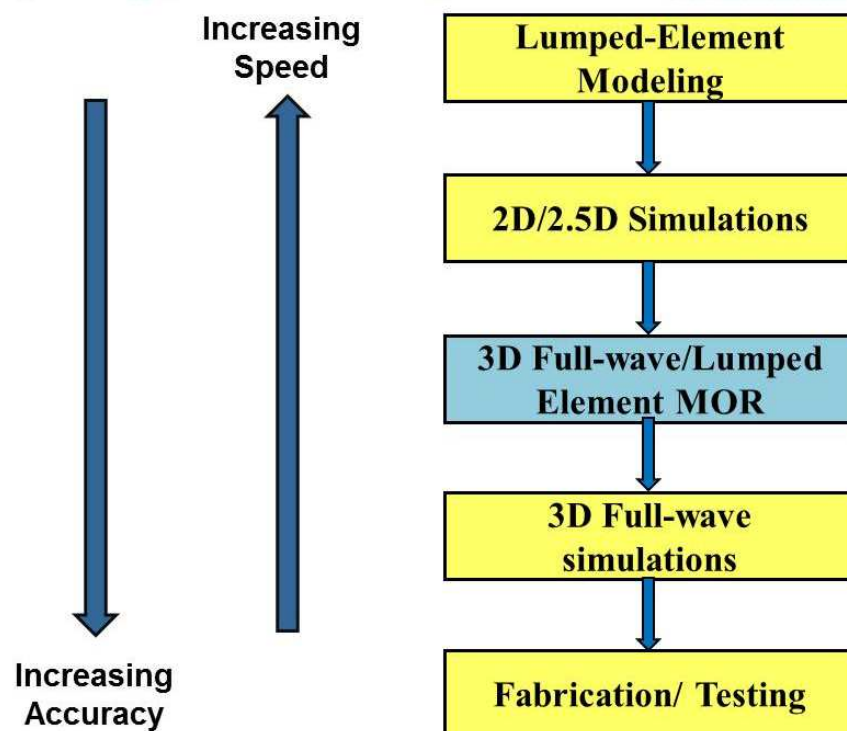
Figure 5: Modified hierarchical design flow for the simulation and testing of semiconductor package modules, inclusive of the proposed hybrid methodology

1.3 Contribution

As part of this work, a computationally fast frequency domain full-wave electromagnetic simulation scheme is developed. The contribution of the research is:

1. The development of a second order equivalent-circuit based full-wave simulation model. Here, an equivalent circuit framework for electromagnetic simulation of one-, two- and three- dimensional problems will be formulated and demonstrated with the help of suitable examples.

2. The development of model order reduction methods that maintain stability and passivity, while generating accurate network response curves. The focus here would be to develop model order reduction techniques, which can work on the equivalent circuit based electromagnetic simulation framework.

Once the above is attained, any given layout can be converted to a second order equivalent circuit based electromagnetic framework, where reduction algorithms can be applied to obtain a fast frequency response. An overview of the technical flow, resulting from the contribution is shown in Fig. 6

1.4 Organization of the Thesis

The thesis is organized as follows: chapter one provides an introduction to the research briefly describing the background and motivation, the expected contribution and the organization of the thesis. Chapter two starts with the description of the nature and origin of the problem being addressed. Susequently, the way the solution to this problem has evolved in terms of computer-aided design (CAD) approaches, and the significant fast methods involved are described. Chapter three describes the extraction of an equivalent full-wave circuit model from a given layout for one-, two-, and three -dimensions starting with the Maxwell's equations. A way of including
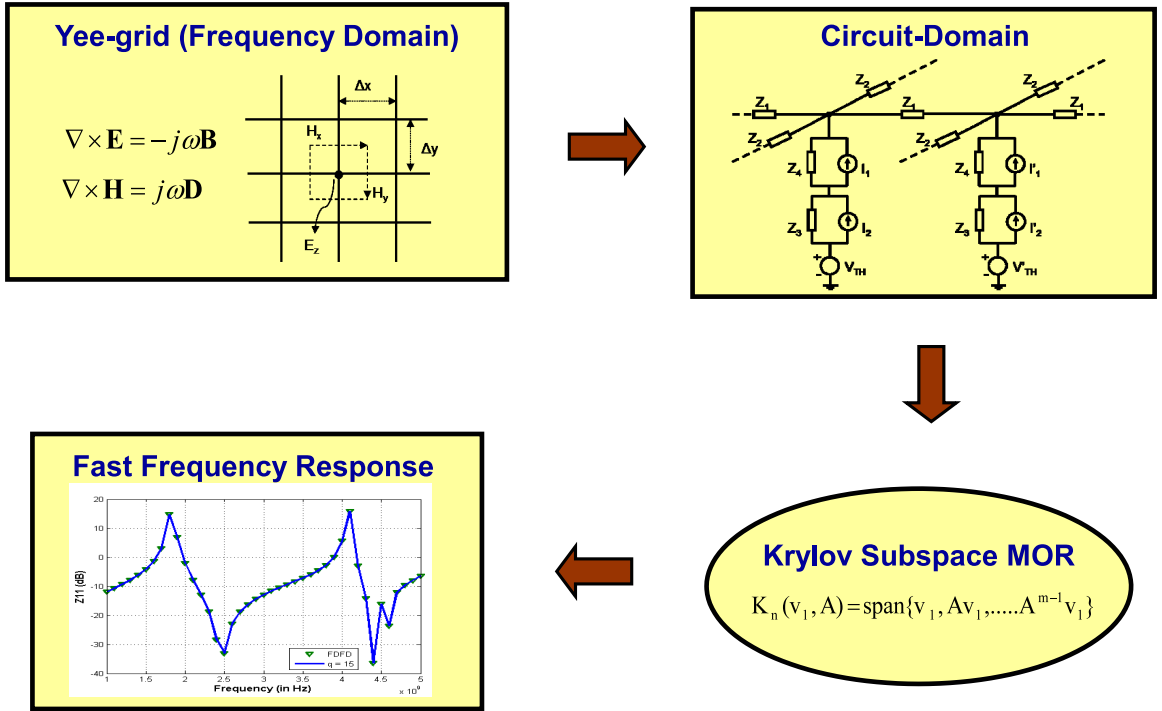
Figure 6: An overview of the proposed simulation technique covering all aspects of the contribution of this thesis.

lumped elements in this equivalent circuit based electromagnetic framework is also described.

In chapter four, model order reduction for the second order equivalent circuit framework is introduced and demonstrated with the help of examples. Chapter five describes an improvement of the algorithm presented in chapter four by using the concept of multipoint expansion. Chapter six then focuses on bilinear conformal transformation and its application in second order reduced order modeling. The corresponding multipoint extension is also introduced and demonstrated with the help of examples. Also, the challenge involved in model order reduction of the combined system is overcome, and validated by means of examples. Chapter seven provides the conclusion and summarizes the contribution of this thesis. Finally, chapter eight describes possible avenues for future work.

CHAPTER II

ORIGIN AND HISTORY OF THE PROBLEM

2.1 Design of IC Packages

The design of IC package with multilayer stack-up (see Fig. 7) while minimizing the negative electromagnetic phenomena is a challenge, as has been briefly described in chapter I. This has been primarily driven in the past by the digital computing needs. With the current and foreseen explosion in the wireless communications industry, the fast and full characterization of the electromagnetic effects in a mixed-signal package becomes imperative. In this regard, the development of radio frequency (RF) front-end modules optimized in terms of size and performance are critical as well. There are two related issues in this respect [56]: 1) Modeling and 2) Analysis. Modeling encompasses the extraction of a physically representative model of the mathematical governing equations. Analysis encompasses the domain of the solution and the method employed to solve the model. In the first section of this chapter, we describe the relevant electromagnetic effects and in the next section, we describe the various methods used to solve these models, paying particular attention to fast methods.

2.1.1 Major Electromagnetic Design Challenges

In terms of specific challenges involved in modern IC package design, the critical electromagnetic effects can be classified as [66] [8]:

1. Reflection noise: Incorrect terminations and signal path discontinuities cause overshoot, undershoot, and ringing, as shown in Fig. 8. This is primarily caused by impedance mismatch, examples of which include - change in signal trace width, branching of signal trace, and signal line crossing a gap in the
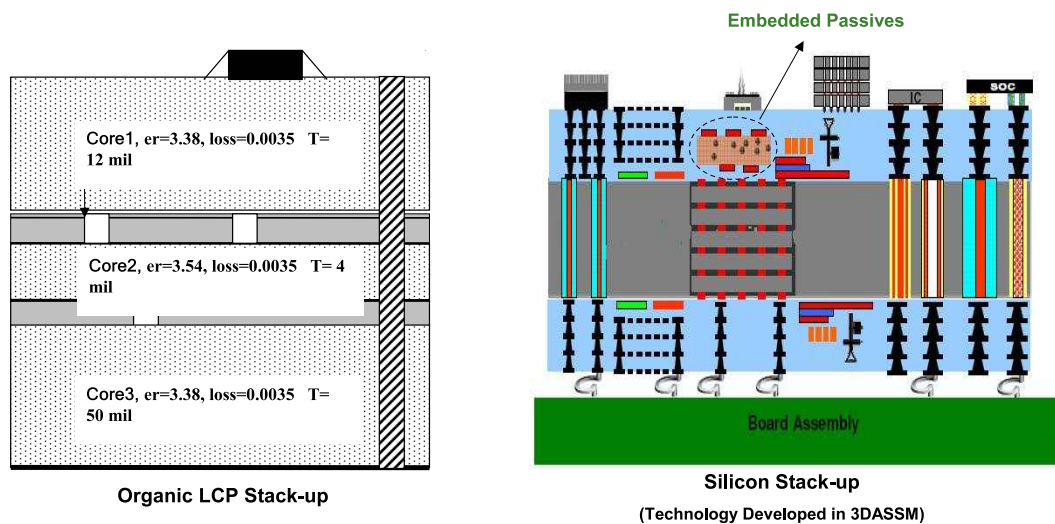
Figure 7: Typical multilayer stackups used/proposed for electronic packages. (Courtesy: Packaging Research Center, Georgia Institute of Technology.)
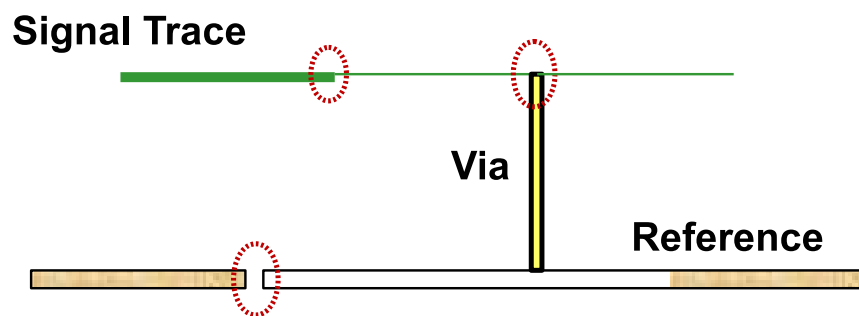
Figure 8: The sources of reflection noise in IC packages.

reference plane giving rise to return path discontinuity.

2. Simultaneous switching noise (SSN): The imperfect nature of power distribution network gives rise to parasitics causing noise, as shown in Fig. 9 reaching orders in the range of hundreds of millivolts. As indicated by the name, a large number of devices switching simultaneously cause fluctuations in the voltage between power and ground planes resulting in SSN.

3. Crosstalk noise: This is caused by the direct electromagnetic coupling between signal traces and vias, as shown in Fig. 10. This is primarily caused due the close placement of such structures resulting in the coupling of electric and magnetic
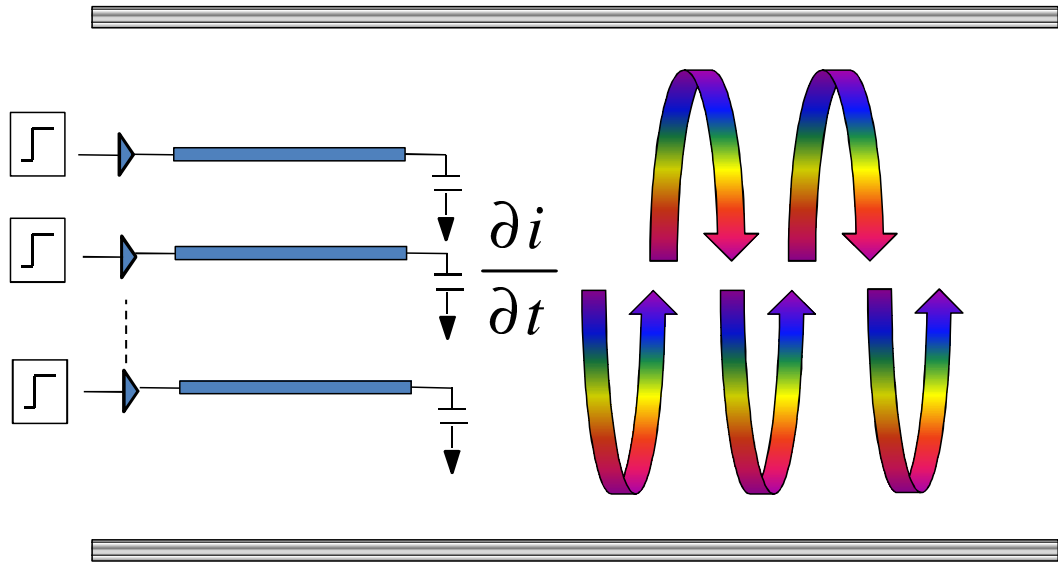
Figure 9: The source of simultaneous switching noise in IC packages.
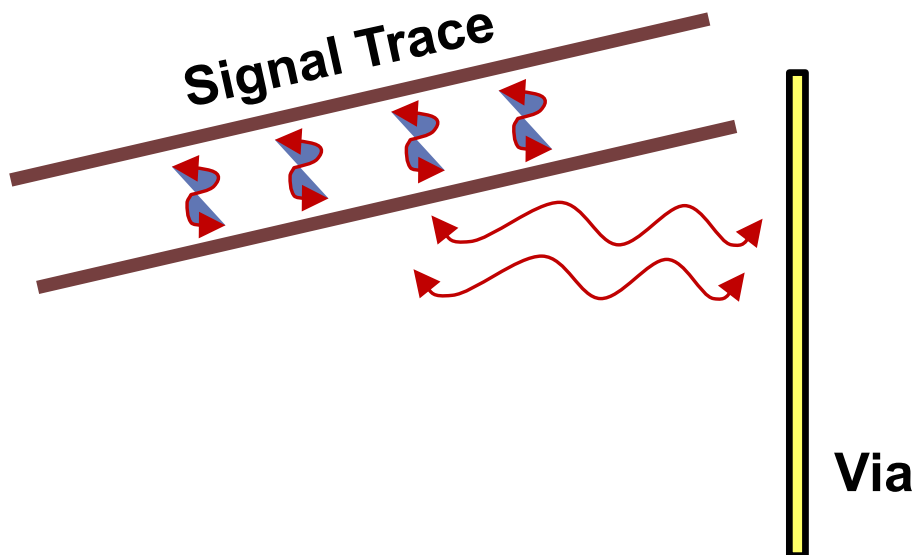
Figure 10: The source of crosstalk noise in IC packages.

fields, giving rise to mutual capacitance and mutual inductance, respectively.

4. Attenuation noise: This is the loss in the intensity of the signal being transmitted, primarily due to the material properties and the loss intrinsically associated with the substrate and the conductors.

In addition to the above effects, the mixed-signal nature of packages, inclusive of digital, analog, and RF modules, makes it even more critical that an electromagnetic solver be used to fully characterize the system.

2.2   Simulation IC Package Modules

The traditional methods for the analysis of package structures were primarily lumped circuit models. Interconnect designs were initially driven by capacitance extraction tools [67, 35]. Indeed, the motivation for modeling interconnect structures was driven by device scaling, and therefore a need for optimizing the placement and routing of interconnects. In this respect, prediction of the delay time (RC delay) was the most important aspect. The crosstalk noise can be modeled through a ratio of the coupling capacitance, C_c, to the lumped capacitance. This relies on the concept of charge-sharing [21]. More accuracy was achieved through the following lumped component models:

1. Lumped RC model (Fig. 11): Following the concept of charge sharing, the resistive component of the conductors were modeled to attain greater accuracy. The initial work involved the derivation of analytical expressions based on RC transmission line model of the interconnects [59, 70]. An illustration of the lumped RC model is shown in Fig. 11.

2. Lumped RLC model: With increasingly higher operating frequencies, the effect of inductance comes in to play, as the impedance due to inductance is directly proportional to the frequency. One should keep in mind that the highest frequency point of interest is related, not to the clock frequency, but to the rise time associated with a signal. And it is this inductive effect that results in ringing , overshoot, and reflection noise. Analytical expression for the delay based on these models have been derived [33, 31]. An illustration of the lumped RLC model is shown in Fig. 12.
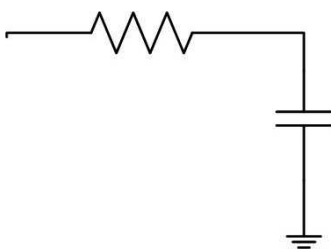
Figure 11: The lumped RC model for an interconnect.
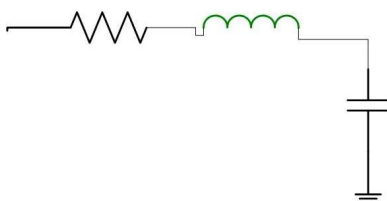
Figure 12: The lumped RLC model for an interconnect.
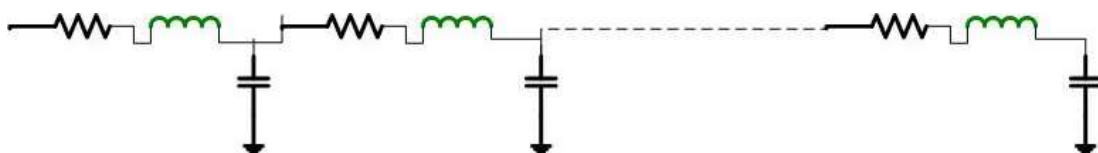
Figure 13: The distributed RLC model for an interconnect.

3. Distributed RLC model: The accurate modeling of the inductive effects inclusive of the mutual inductance effects due to the long current return paths necessitated consideration of the distributed RLC models [14, 4]. An illustration of the lumped RLC model is shown in Fig. 13.

As design complexity of integrated circuit packages increases, [66], the argument in favor of the use of full-wave three dimensional (3D) simulation increases, as against using lower dimensional simulations or lumped-circuit equivalent models. The full-wave solvers in turn can be classified as [56] (also shown in Table 1) :

1. Differential equation based: The differential equation based solvers include the finite difference method [78] and the finite element method [32]. Such methods typically rely on discretizing the entire volume of the structure under investigation and solve for the relevant electromagnetic fields throughout the layout.

In the time domain, such methods are limited by stability conditions. For the finite difference time-domain method (FDTD), the stability requirement gives rise to the well-known Courant condition [68]. In the frequency domain, these methods give rise to the *inverse problem* - the inversion of a large sparse matrix, which is time and memory intensive. A major advantage of such methods is their generality. Since the whole geometry is discretized, variations in material properties and geometrical features in a layout can be accurately captured. This can, however, result in a very large problem size due to the fine meshing of the layout. Techniques such as non-uniform meshing, adaptive refinement of the grid, multigridding and domain decomposition can be used to alleviate such concerns. In addition, efficient sparse matrix solvers, be it in terms of direct solution or iterative solution can be used.

2. Integral equations based: A useful interpretation of the electromagnetic problem is in terms of the electric field at any point in the layout as the superposition of the fields due to currents and charges elsewhere in the system. Method of moments [26] is the prevalent solver in this domain, wherein only the conductor regions are discretized. The integral equation based methods give rise to smaller dense matrices. Due to the dense nature of these matrices, if direct solvers were to be used, it would be far more expensive to solve the integral equation based solver, than the differential equation based solvers. This is because the complexity scales as $O(N^3)$ for dense matrices, as compared to $O(N^2)$ in the case of sparse matrices, N being the zie of the system matrix.

2.2.1 Fast Methods for IC Package Simulation

For integral equation based solvers, the prominent method of choice is the fast multipole method (FMM) [23, 62, 13], and has been successfully applied for capacitance extraction [43], inductance extraction [34], and for scattering from conductor as well

12

Table 1: Comparison of the electromagnetic simulation approaches based on the equations solved.

Differential Equation Based	Integral Equation Based
· Finite difference and finite element method	· Method of moments
· Volumetric discretization over entire layout	· Discretization of only conductor elements
· Generate larger sparse matrices	· Generates smaller dense matrices

as dielectric bodies [17]. For finite difference based methods, this has been addressed, amongst other methods, by means of non-uniform meshing [68, 45], multigrid techniques [73, 72], domain decomposition methods [75, 77] and reduced domain simulations with approximations for one dimension [18]. The Courant condition which imposes a limitation on the grid size for the FDTD method has been overcome through the use of unconditionally stable implicit methods [64, 44, 63]. However, the fast and full characterization of designs remains an important aspect, both in terms of validating lumped circuit models and lower dimensional simulations, and in terms of speeding the design flow. Model order reduction methods provide an alternative fast solution to the aforementioned problem.

2.3 *Equivalent Circuit based Electromagnetic Simulation*

The interpretation of the full-wave equations can also be done in terms of equivalent circuits. Equivalent circuit-based solvers have found favor due to a variety of reasons: 1) use of SPICE for electromagnetic simulation 2) use of circuit-based numerical techniques 3) ease of EM/lumped circuit element co-simulation. Some of the prominent solvers of this category are discussed below.

1. PEEC model: In [57], an equivalent circuit was extracted from the electric field

integral equation (EFIE) in terms of the capacitive and inductive interaction. This directly derives from the fact that the EFIE can be interpreted in terms of a partial inductive and partial capacitive interaction between the currents and charges present in the layout. This results in the distributed equivalent circuit network representation called the partial element equivalent circuit (PEEC) representation.

The PEEC model derivation starts with the equation for the total electric field at a point, $\mathbf{r}$, inside a conductor with conductivity, σ, as

$$\mathbf{E}_0(\mathbf{r}, t) = \frac{\mathbf{J}(\mathbf{r}, t)}{\sigma} + \frac{\partial \mathbf{A}(\mathbf{r}, t)}{\partial t} + \nabla \Phi(\mathbf{r}, t) \tag{1}$$

where, $\mathbf{E}_0$ is the applied electric field, $\mathbf{J}$ is the conductor current density, $\mathbf{A}$ is the magnetic vector potential and Φ is the electric scalar potential. Proceeding from the above equation, in conjunction with substitutions for electric scalar potential and magnetic vector potential, an integral equation can be derived for the total electric field. This equation in combination with the current continuity equation, shown below in (2), forms the basis for derivation of the PEEC model.

$$\nabla \cdot \mathbf{J} + \frac{\partial q}{\partial t} = 0. \tag{2}$$

The resulting PEEC model is shown in Fig. 14.

The resulting system of equations for PEEC is in the form of modified nodal analysis (MNA) equations, wherein the enforcement of Kirchoff's current law for the PEEC model corresponds to the solution of the current continuity equation (2).

2. Equivalent circuit model for FDTD: In [12], a circuit interpretation of the FDTD grid was provided. The FDTD grid is directly converted in terms of a network

14
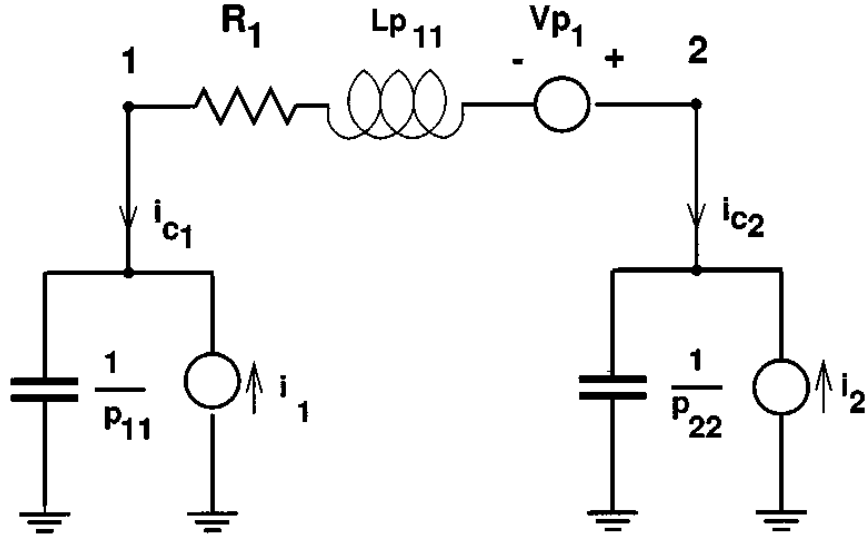
Figure 14: The partial element equivalent circuit model [57].

of interconnected gyrators and capacitors. The very nature of the derivation ensures the stability of the equivalent circuit, by satisfying the Courant condition.

3. Transmission line matrix method: A popular differential equation based equivalent circuit simulation method is the transmission line matrix (TLM) technique [28, 29, 15, 53]. It starts with the Huygens model of wave propagation. The entire layout is converted to a set of interconnected transmission lines. The excitation of the layout results in transmissions and reflections, which can be calculated based on transmission line theory. In Cartesian coordinates ,this results in a set of interconnected unit cells comprising transmission lines. Scattering parameters may be suitably calculated by measuring the transmitted and reflected waves. An illustration of the three dimensional TLM model is shown in Fig. 15.

4. Susceptance element based solvers: Susceptance elements have been recently studied as promising candidates for modeling magnetic coupling [16, 5, 79]. [16] starts with the expression for partial inductances and then proceeds to

15
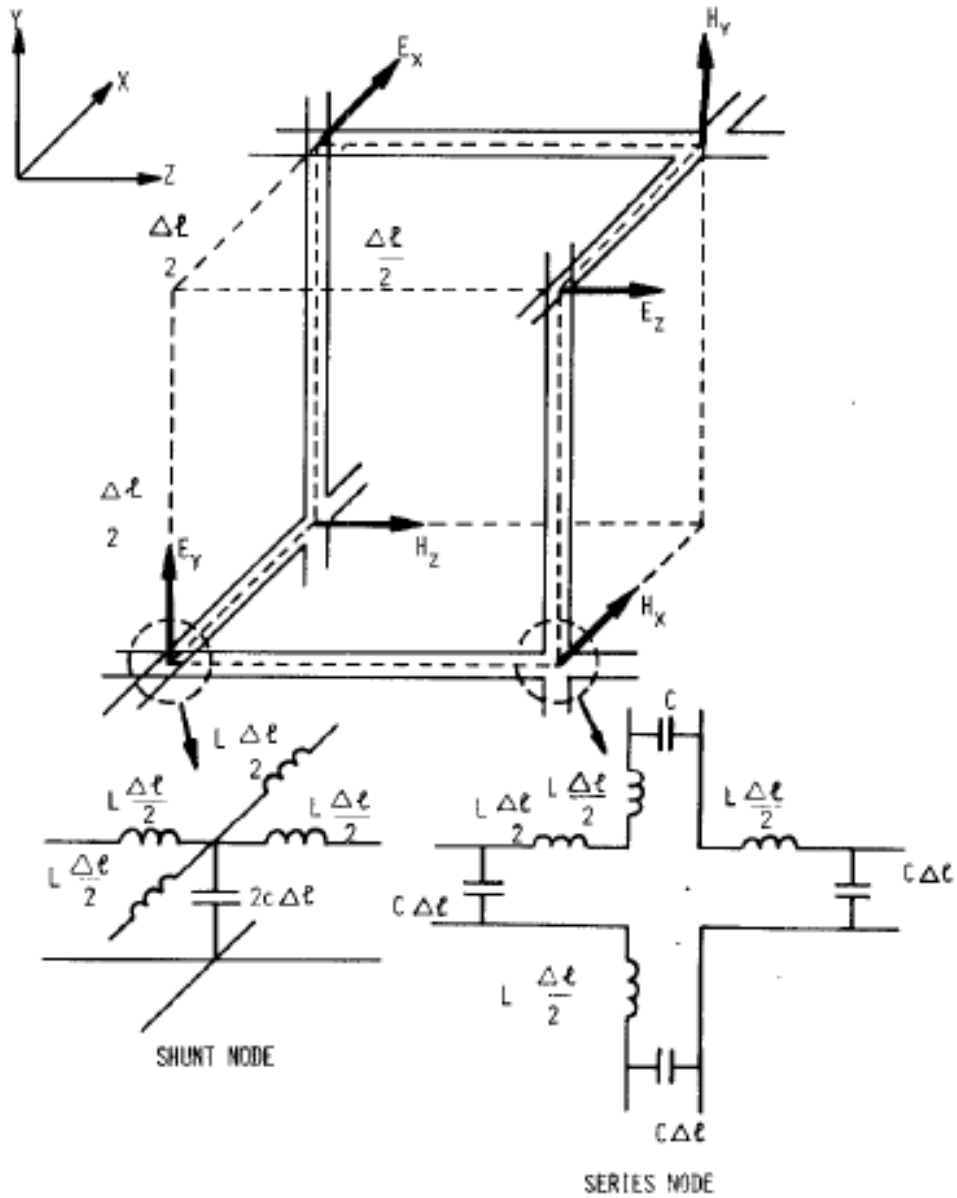
Figure 15: The three dimensional transmission line matrix model [29].

calculate the susceptance matrix. In [5], the extraction process is modified to include only partial inductance models for small localized windows. However, the extraction of equivalent circuit from layout, based on Maxwell's equations does not mitigate the huge requirement in terms of time and/or memory, and therefore necessitates the use of fast methods, more specifically, model order

16
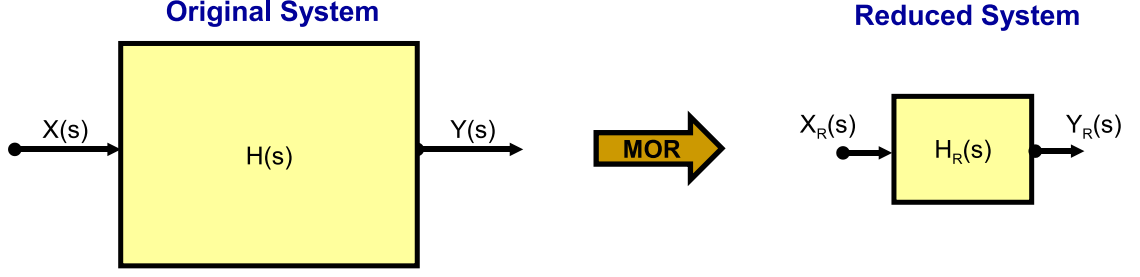
Figure 16: The basic concept of model order reduction (MOR).

reduction methods.

2.3.1 Model Order Reduction for Electromagnetic Simulation

In the frequency domain, the accelerated analysis of complex structures has been made possible through model order reduction methods [56]. Given a linear system, the aim of MOR is to create a reduced system such that the transfer function of the system is approximated with an acceptable tolerance. This is illustrated in Fig. 16, wherein the original system transfer function, $H(s) = Y(s)/X(s)$, is reduced to $H_R(s) = Y_R(s)/X_R(s)$.

To begin the discussion on model order reduction in detail, a linear circuit network is considered, composed of resistive, capacitive and inductive elements. From circuit theory [71], the corresponding analysis for this network can be done by means of the modified nodal analysis equations given as,

$$s\mathbf{C}\mathbf{X}(s) = -\mathbf{G}\mathbf{X}(s) + \mathbf{B}\mathbf{U}(s), \tag{3a}$$

$$\mathbf{Y}(s) = \mathbf{L}^T\mathbf{X}(s), \tag{3b}$$

where, $\mathbf{C}, \mathbf{G} \in \mathbb{C}^{N \times N}$, $\mathbf{B} \in \mathbb{C}^{N \times m}$ and $L \in \mathbb{C}^{N \times p}$, m being the number of inputs, and p is the number of ports, $\mathbf{U}$ is the external current or voltage excitation, $\mathbf{X}$ is the input state variable, and $\mathbf{Y}$ is the output state variable. Assuming zero initial

conditions, the transfer function for the above equations may be written as

$$\mathbf{H}(s) = \mathbf{L}^T (\mathbf{G} + s\mathbf{C})^{-1} \mathbf{B}. \tag{4}$$

The approximation to the above expression is the goal of model order reduction methods, which may be classified on the basis of their mathematical solution type as, an explicit method or as an implicit method.

In the case of explicit method, the transfer function is first expanded by the means of an infinite Taylor's series expansion as,

$$\mathbf{H}(s) = H_0 s + H_1 s + H_2 s^2 + \ldots . \tag{5}$$

The idea then is to truncate the above infinite series at a particular order as,

$$\mathbf{H}_q(s) = H_0 s + H_1 s + H_2 s^2 + \ldots + H_q s^q, \tag{6}$$

such that a good approximation of the original system is obtained. In the case of the Pade' approximation, the transfer function is represented as a rational function as shown below

$$\mathbf{H}_q(s) = \frac{P_q(s)}{Q_q(s)} = \frac{a_0 s + a_1 s + a_2 s^2 + \ldots + a_m s^m}{1 + b_0 s + b_1 s + b_2 s^2 + \ldots + b_n b^n}. \tag{7}$$

Due to its rational form, Pade' approximation is better able to capture the poles in a system than the corresponding Taylor's series expansion. Early research on these techniques focused on reducing model order of interconnects through explicit moment calculation or the Krylov-subspace counterpart thereof, resulting in compact models. In [54], the asymptotic waveform reduction algorithm (AWE) was proposed which is an explicit moment matching technique using Pade' approximations to generate reduced order models. But this method was found to be unstable when matching higher order moments. Projection based methods were studied as a numerically stable alternative, and more specifically the Krylov subspace methods were used for reduction. The basic idea in Krylov subspace reduction is to generate a set of basis

vectors, which are then used for projecting the original system to a space where the resulting transformed system is much smaller. The Krylov subspace based reduction process is illustrated in Fig. 17. The Pade' via Lancszos Iteration (PVL) [19] is one such method, where the Lanczos process is used to implicitly match moments. Issues regarding the passivity of the MOR techniques were addressed in the passive reduced order interconnect macromodeling algorithm (PRIMA) [48]. Qualitatively, a circuit is defined to be passive if the net energy generated by the circuit is zero. The task of ensuring passivity of the circuit remains non-trivial, and involves additional enforcement algorithms. Depending on the need, one may enforce strict passivity or conditional passivity [56]. The introduction of conditional passivity made it possible to use MOR of full-wave simulations for the analysis of passive structures. The model order reduction for electromagnetic governing equations has been previously presented in [9, 65, 50, 38, 76, 47]. In [27], the partial element equivalent circuit (PEEC) model extracted from an interconnect layout is suitably reduced using AWE. In [74], a comparison of the use of AWE, PVL and PRIMA for compact finite difference frequency domain (FDFD) scheme is provided. To work with susceptance element based circuits, we have to use a suitable model order reduction method which works on susceptance elements, instead of mutual inductance terms as has been the trend. Susceptance element based model order reduction have recently found increasing interest. The efficient nodal order reduction method (ENOR) [60] was used to reduce lumped models extracted from interconnect structures without the need for additional passivity enforcement algorithms. It applies an orthogonal projection on the system based on moment-matching techniques in combination with Arnoldi-like orthogonalization [61]. Stability issues during the orthogonalization process were addressed in the improved ENOR (imp-ENOR) algorithm [80].

It becomes even more involved to find a reduced model, when the response of a given layout exhibits complex behavior. One way to address the issue is by increasing

19
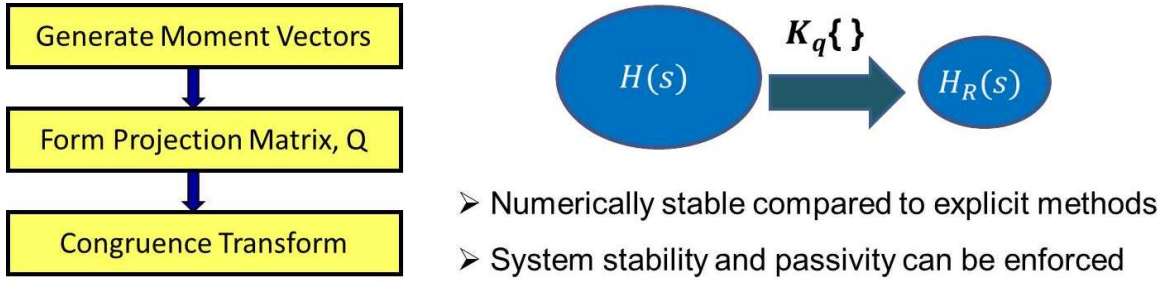
Figure 17: The concept of Krylov subspace based model order reduction method.

the order of the solution, thus in effect, matching more moments of the reduced model to the original system. But keeping in mind that for given imaginary points of expansion, Krylov projections are necessarily a localized approximation, the efficacy of the aforementioned approach can be expected to vary depending on the reduced order. In this regard, improvement can be obtained by choosing multiple points of expansion to obtain a more globally representative projection matrix. This has been demonstrated for rational functions by means of complex frequency hopping (CFH) algorithm [11], and for Krylov projections by multipoint expansion algorithms [22, 24, 30]. A significant variation of the linear model order reduction scheme was shown in [10] by performing the PVL process through a bilinear conformal transformation (BCT), which resulted in a reduction with a definite error-bound. This process was subsequently shown in [37] to be a subset of a more general projection method with a non-unity multiplicative constant in the BCT.

Another important class of MOR for package and interconnect structures is the balanced truncation method [51, 52]. The major advantage of such methods is the existence of an a priori error bound. However, such methods also suffer from a memory complexity requirement of $O(N^3)$, N being the number of unknowns. This precludes the direct application of such methods for larger problems. Table 2 shows the comparison between Krylov-subspace and balanced truncation methods.

Table 2: A comparison between the two major MOR methods.

MOR	Krylov-subspace	Balanced Truncation
Error bound	None	Exists a priori
Complexity	$O(Nlog(N))$	$O(N^3)$
Optimality	----	Near/ Exact
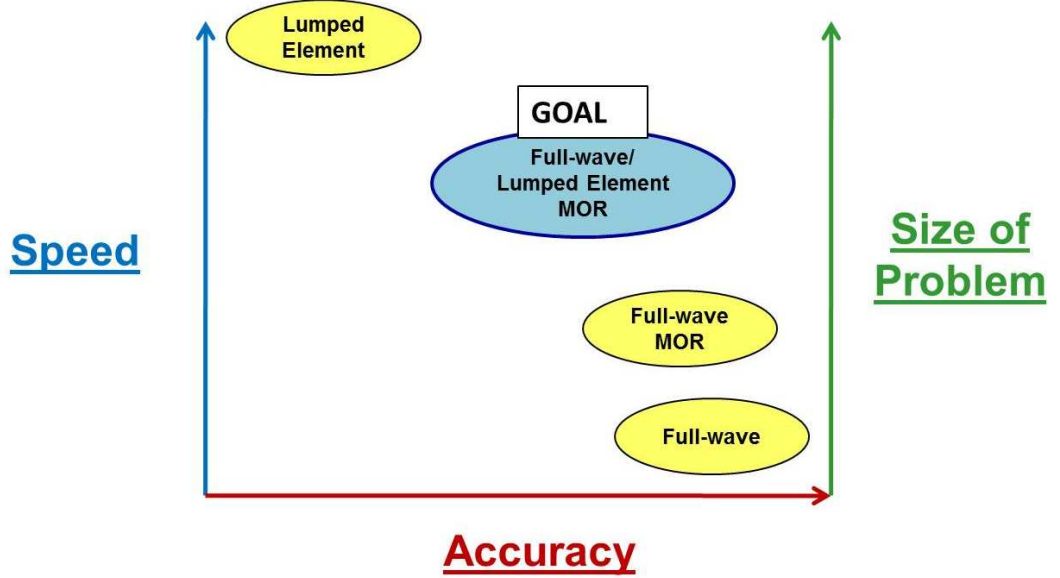
Figure 18: The contribution of this thesis in the design space of simulation methods.

2.4 *Contribution of Thesis - A Broader Perspective*

If we were to look at the design space in terms of the the size of the problem and the main parameters being the accuracy of the simulation technique and the speed with which the solution is obtained, each of these techniques can be suitably characterized. It is in this context, that we place our goal to be a hybrid approach which is able to find a suitable balance between the speed of simulation and the accuracy of the results obtained. This is shown in terms of the design space in Fig. 18.

Fig. 19 shows the goal of this thesis in terms of the primary fields involved.
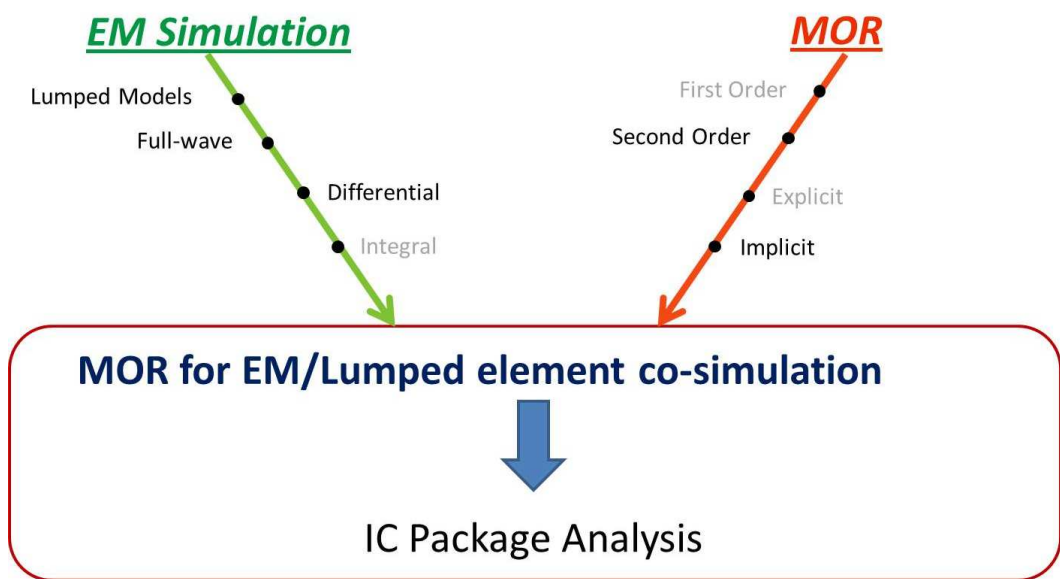
Figure 19: The goal of this thesis, in terms of electromagnetic simulation and model order reduction.

CHAPTER III

EQUIVALENT CIRCUIT BASED ELECTROMAGNETIC SIMULATION

3.1   Introduction

In this chapter a second order equivalent circuit framework for solving electromagnetic system of equations will be discussed. This framework is based on the differential equation based method, described briefly in the previous chapter.

3.2   Equivalent Circuit based Full-wave Simulation - SEEC Model

In this section the formulation for extracting the second order susceptance element equivalent circuit (SEEC) model is described, and then validated with numerical results. The concept, as illustrated in Fig. 20, is to move from layout to a second order equivalent circuit form.

3.2.1   Susceptance Element Equivalent Circuit (SEEC) Model

First, consider the differential form of Maxwell's equation in the frequency domain:

$$\nabla \times \vec{H} = j\omega \vec{D} + \sigma \vec{E} + \vec{J}_s \tag{8a}$$

$$\nabla \times \vec{E} = -j\omega \vec{B} \tag{8b}$$

$$\nabla \cdot \vec{D} = \rho \tag{8c}$$

$$\nabla \cdot \vec{B} = 0 \tag{8d}$$

where, ω is the frequency in radians, $\vec{E}$ and $\vec{H}$ are the electric and magnetic field vectors respectively, $\vec{D}$ and $\vec{B}$ are the related field/flux density vectors respectively, σ is the position-dependent conductivity of the medium, ρ is the electric charge density,
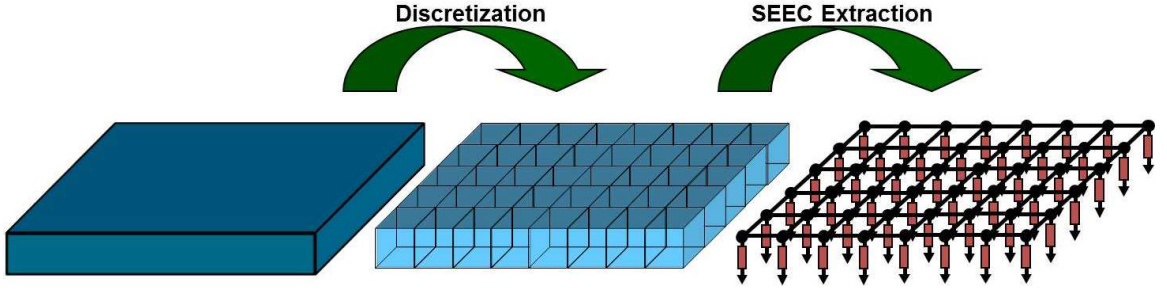
Figure 20: The susceptance element equivalent circuit, SEEC, model extraction process.

and $\vec{\mathbf{J}}_s$ is the external current density source vector. In 3D, the above vector equations for an isotropic, inhomogeneous medium can be written in scalar form, discretizing in each direction of the Cartesian coordinates. The Yee-grid [78], as shown in Fig. 21, is used so as to implicitly satisfy the divergence laws (8c) and (8d). The discretized equations can be written in block matrix form as:

$$\left(\begin{bmatrix} \mathbf{G}_\sigma & \mathbf{D}_h \\ \mathbf{D}_e & \mathbf{0} \end{bmatrix} + j\omega \begin{bmatrix} \mathbf{C}_\epsilon & \mathbf{0} \\ \mathbf{0} & \mathbf{L}_\mu \end{bmatrix} \right) \begin{bmatrix} \mathbf{E} \\ \mathbf{H} \end{bmatrix} = \begin{bmatrix} \mathbf{M}_e \\ \mathbf{M}_h \end{bmatrix} \mathbf{I}_{eh} \tag{9}$$

where, $\mathbf{D}_h$ and $\mathbf{D}_e$ are the discretized matrix forms of the curl operator for the magnetic and electric field vectors respectively, $\mathbf{G}_\sigma$ is the conductance matrix associated with losses in the media, $\mathbf{C}_\epsilon$ is the capacitance matrix associated with the dielectric permittivity of the medium, $\mathbf{L}_\mu$ accounts for the self and mutual inductances due to the magnetic permeability of the medium, $\mathbf{E}$ and $\mathbf{H}$ are the matrix forms of the electric and magnetic field vectors in Cartesian coordinates respectively, $\mathbf{M}_e$ and $\mathbf{M}_h$ are the incidence vectors for the electric and magnetic current density excitation represented by $\mathbf{I}_{eh}$.

3.2.2 1D SEEC Extraction

In a single dimension, say z, the Maxwell's equations to be considered are

$$j\omega\epsilon E_y = \frac{\partial H_x}{\partial z} - \sigma E_y \tag{10}$$

24
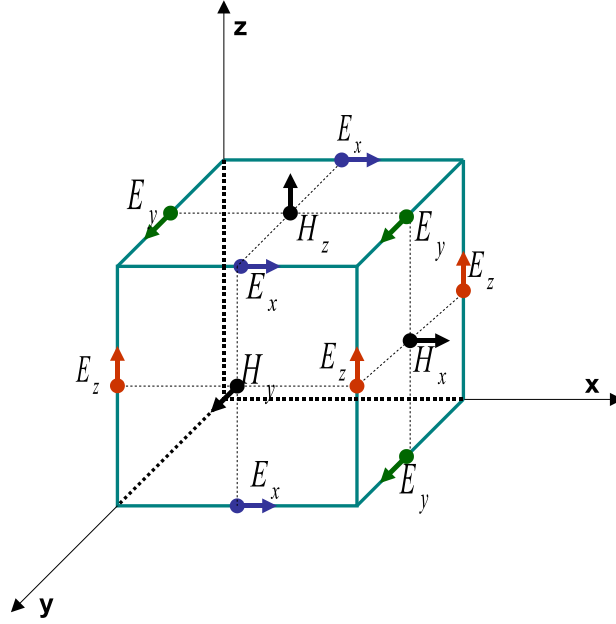
Figure 21: The Yee cell discretization, showing the dual grid placement of electric and magnetic fields.
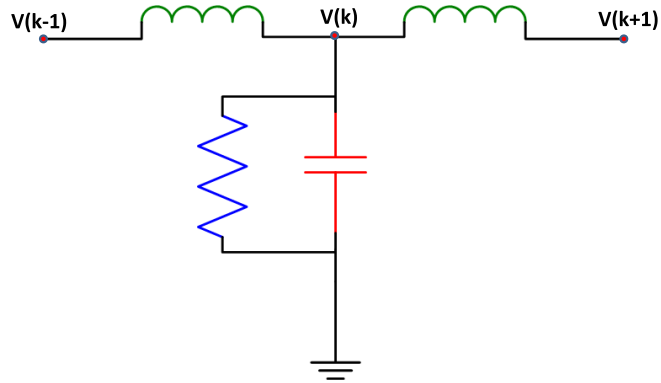
Figure 22: The one-dimensional susceptance element equivalent circuit, SEEC, model.

$$j\omega\mu H_x = \frac{\partial E_y}{\partial z} \tag{11}$$

Substituting for H_x in E_y from (11) in (10), and using the Yee-grid discretization, the SEEC model in 1D can be easily extracted. The relevant extracted model is shown in Fig. 22, where k is the index for discretization along the z- direction, Δz represents the discretization in z- direction, and the electric field at each node is mapped as the corresponding nodal voltage.

25

3.2.3 2D SEEC Extraction

The transverse magnetic mode governed as below, is considered:

$$j\omega E_x = \frac{1}{\epsilon}\left(\frac{\partial H_z}{\partial y} - \frac{\partial H_y}{\partial z} - \sigma E_x\right) \tag{12}$$

$$j\omega H_y = \frac{1}{\mu}\left(-\frac{\partial E_x}{\partial z}\right) \tag{13}$$

$$j\omega H_z = \frac{1}{\mu}\left(\frac{\partial E_x}{\partial y}\right) \tag{14}$$

Substituting (4) and (5) in (3), and discretizing using the Yee cell, the following is obtained:

$$\left(\mathbf{G}_x + s\mathbf{C}_x + \frac{\Gamma_x}{s}\right)\mathbf{V}_x = \mathbf{B}_x\mathbf{I}_x \tag{15}$$

It is to be noted that the susceptance elements can also be formulated in terms of controlled sources. The companion model for such a transformation is shown in Fig 23, where ϵ is the dielectric permittivity of the medium, and Δy and Δz are the discretization lengths in the y- and z- directions, respectively.

3.2.4 3D SEEC Extraction

The SEEC model for 3D can be extracted in a way similar to the 2D extraction process.

Here, the differential Maxwell's equations under consideration can be written as

$$j\omega\epsilon E_x = \frac{\partial H_z}{\partial y} - \frac{\partial H_y}{\partial z} - \sigma E_x \tag{16}$$

$$j\omega\epsilon E_y = \frac{\partial H_x}{\partial z} - \frac{\partial H_z}{\partial x} - \sigma E_y \tag{17}$$

$$j\omega\epsilon E_z = \frac{\partial H_y}{\partial x} - \frac{\partial H_x}{\partial y} - \sigma E_z \tag{18}$$

$$j\omega\mu H_x = -(\frac{\partial E_z}{\partial y} - \frac{\partial E_y}{\partial z}) \tag{19}$$

$$j\omega\mu H_y = -(\frac{\partial E_x}{\partial z} - \frac{\partial E_z}{\partial x}) \tag{20}$$

$$j\omega\mu H_z = -(\frac{\partial E_y}{\partial x} - \frac{\partial E_x}{\partial y}) \tag{21}$$

26

$$j\omega\varepsilon E_z = \frac{\partial H_y}{\partial x} - \frac{\partial H_x}{\partial y} - J_z$$

$$j\omega\mu H_x = -\frac{\partial E_z}{\partial y}$$

$$j\omega\mu H_y = \frac{\partial E_z}{\partial x}$$
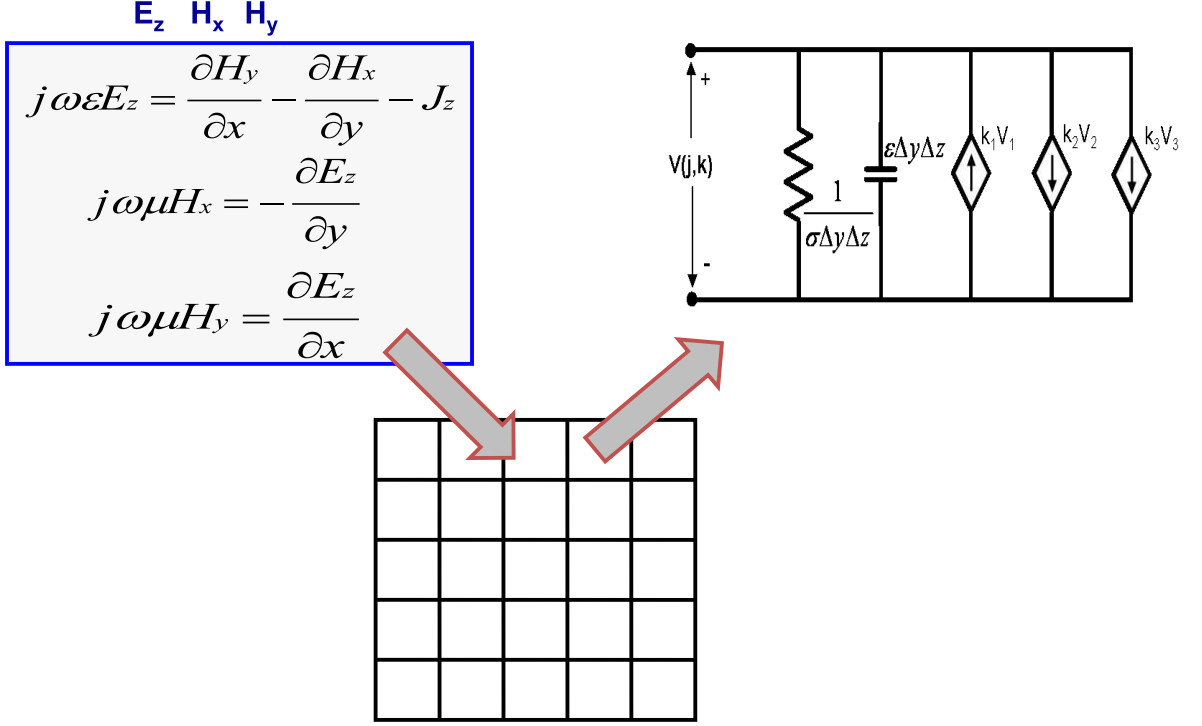
Figure 23: The susceptance element equivalent circuit, SEEC, model for a single voltage node for a x- directed transverse magnetic mode.

Discretizing the above using the Yee-grid, and then substituting for the magnetic fields in the electric field equations, the 3D SEEC model is extracted, wherein additional susceptance elements account for the interaction between all the the fields. An illustration of this process is shown in Fig. 24. Perfect electric conductor (PEC) and perfect magnetic conductor (PMC) boundary conditions are enforced by shorting and opening the nodal points along the boundaries of the simulation domain, respectively. This allows us to extract a susceptance element based equivalent circuit model directly from a given layout. The use of susceptance element for equivalent model construction is also advantageous as has been discussed previously in [5][79]. The relevant block matrix equations for the 3D simulation can then be written in a manner similar to (15) as

$$\left(\mathbf{G} + s\mathbf{C} + \frac{\Gamma}{s}\right)\mathbf{V} = \mathbf{BI} \tag{22}$$

where, $\mathbf{G}, \mathbf{C}, \Gamma \in \mathbb{R}^{N \times N}$, $\mathbf{B} \in \mathbb{R}^{N \times p}$ and $\mathbf{I} \in \mathbb{R}^{p \times p}$, N is the number of unknowns, and

27
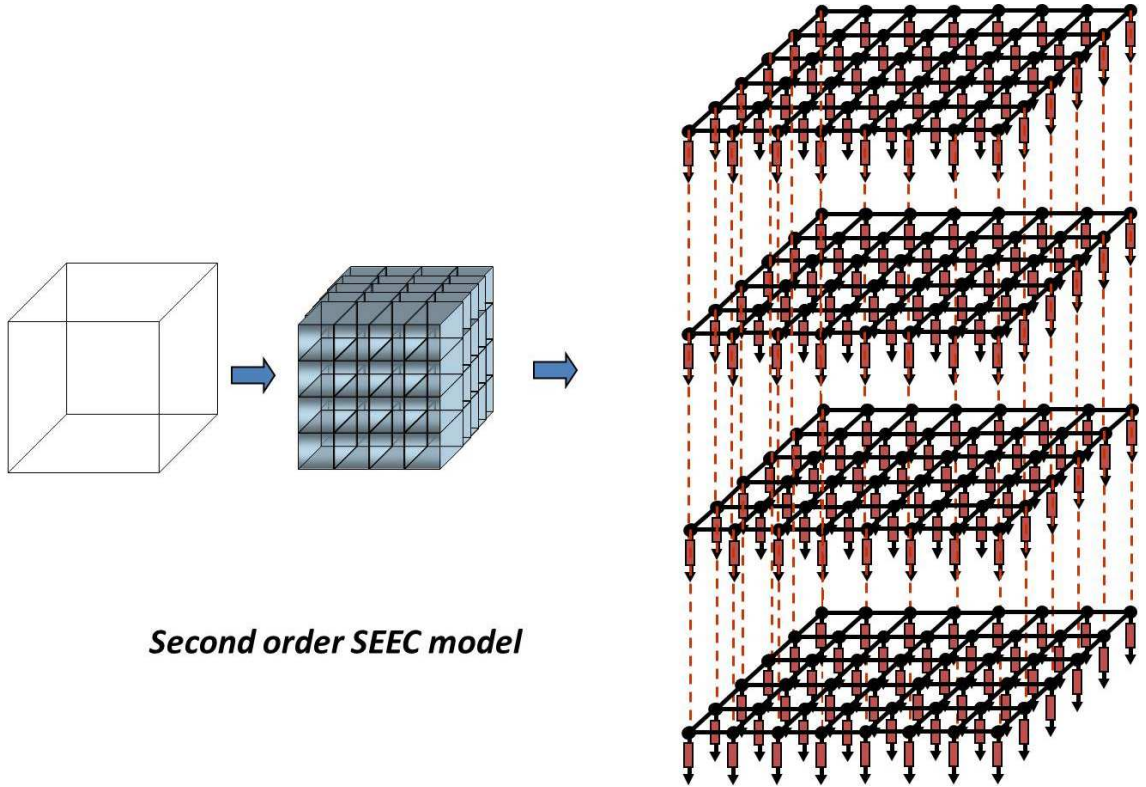
Figure 24: The three dimensional extraction of the susceptance element equivalent circuit, SEEC, model.

p is the number of ports. Essentially (22) is the nodal analysis form of the Maxwell's equation and corresponds directly to the Helmholtz equations. It is by working on this second order model that significant advantages are gained [60], as against using MOR of linear systems [74]. The susceptance matrix, along with the capacitance and conductance matrices, is symmetric positive semidefinite with a diagonal dominance, and is therefore amenable to fast iterative solution [79].

3.2.5   Inclusion of Losses

Dielectric losses can be included by changing the capacitance term in the SEEC model. Inclusion of skin effect mode has to be done taking into account the surface impedance boundary condition [6]. A representation of the modified two dimensional SEEC model accounting for the dielectric and skin effect losses is shown in Fig. 25
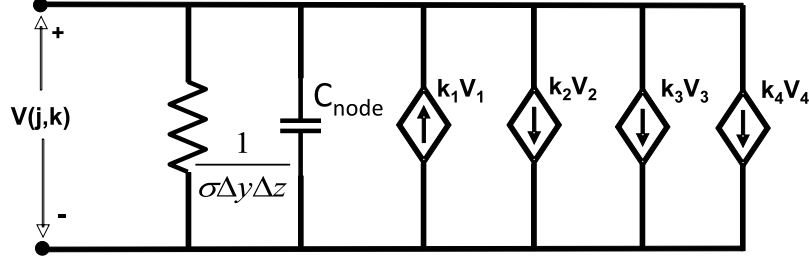
$$C_{node} = (\varepsilon_r - j\tan\delta)\Delta y\Delta z$$

$$k_1 = \frac{2}{j\omega\mu}(\Delta y + \Delta z) + 4\sqrt{\frac{\sigma}{j\omega\mu}} \quad V_1 = V(j,k)$$

$$k_2 = \frac{\Delta z}{j\omega\mu} \quad V_2 = V(j+1,k) + V(j-1,k)$$

$$k_3 = \frac{\Delta y}{j\omega\mu} \quad V_3 = V(j,k+1) + V(j,k-1)$$

$$k_4 = \sqrt{\frac{\sigma}{j\omega\mu}} \quad V_4 = V(j,k+1) + V(j,k-1) + V(j+1,k) + V(j-1,k)$$

Figure 25: The two dimensional susceptance element equivalent circuit, SEEC, model inclusive of losses.

3.3   Numerical Test Cases

3.3.0.1   Power Ground Structure with Aperture

In the introduction as well as the description of the origin and history of the problem, various reasons to motivate the need for 3D simulations in package modeling have been mentioned. With the first example of a power ground structure with aperture, we provide a physical representation of the 3D nature of the fields. The cross-section and the top view of the structure is shown in Fig. 26 and Fig. 27, respectively. A network port is defined between the top and bottom planes. The plot of the electric field distribution along the x- and y- directions along the plane of the aperture is shown in Fig. 28 and Fig. 29, respectively. The z- component of electric field is shown in Fig. 30. The presence of the fringing fields is clearly seen, which cause a coupling of the fields from the bottom layer to the top.
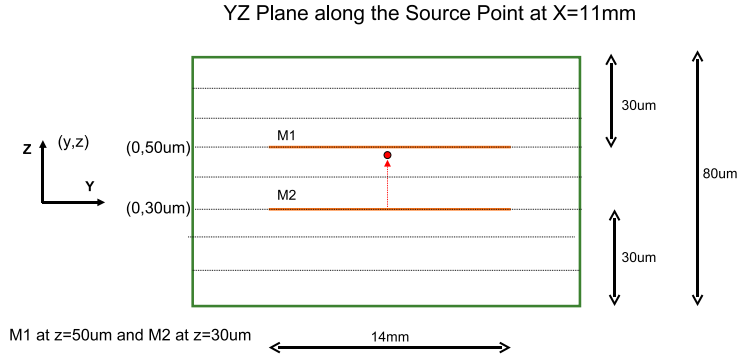
Figure 26: The cross-section of the power plane structure with aperture.
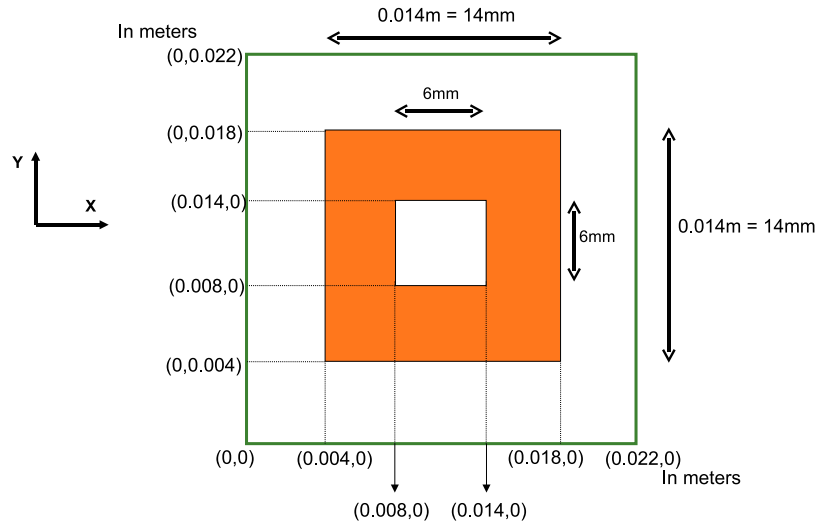
Figure 27: The top-view of the power-plane structure with aperture.

3.3.0.2 Power Plane

To verify the accuracy of the equivalent-circuit based full-wave simulation approach, a power-ground plane, as shown in Fig. 31, is simulated. A 13 $mm \times$ 13 mm thin metal plane is considered, placed at the center of a dielectric box of dimensions 21 $mm \times$ 21 $mm \times$ 60 μm. A unit cell of 0.5 $mm \times$ 0.5 $mm \times$ 10 μm was used to discretize the structure shown in Fig. 31. The dielectric constant of the homogeneous medium enclosed in the PEC box is 3.8. The impedance response of the structure obtained from the SEEC model is compared to that obtained from the simulation using Laguerre equivalent circuit (SLeEC) approach, also called the Laguerre-FDTD [63]. Since, Laguerre-FDTD and SEEC model use similar finite difference discretization
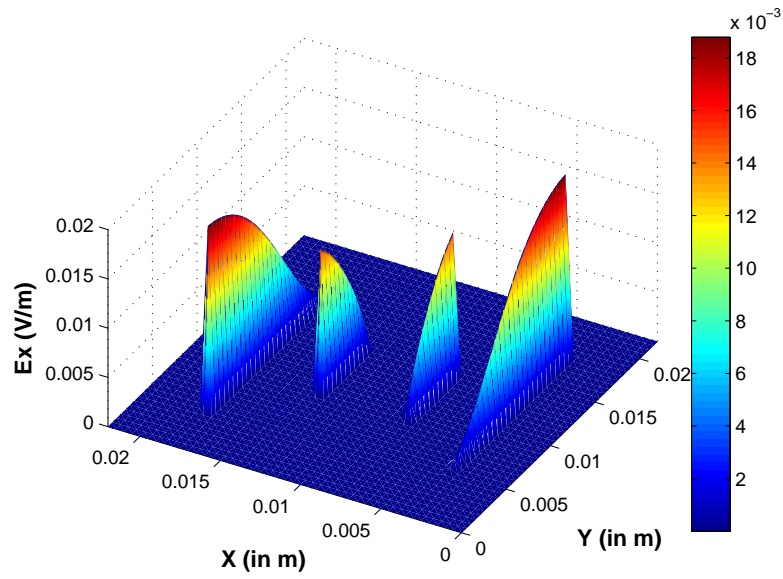
Figure 28: Electric field distribution along the x- direction of the power-ground structure with aperture.
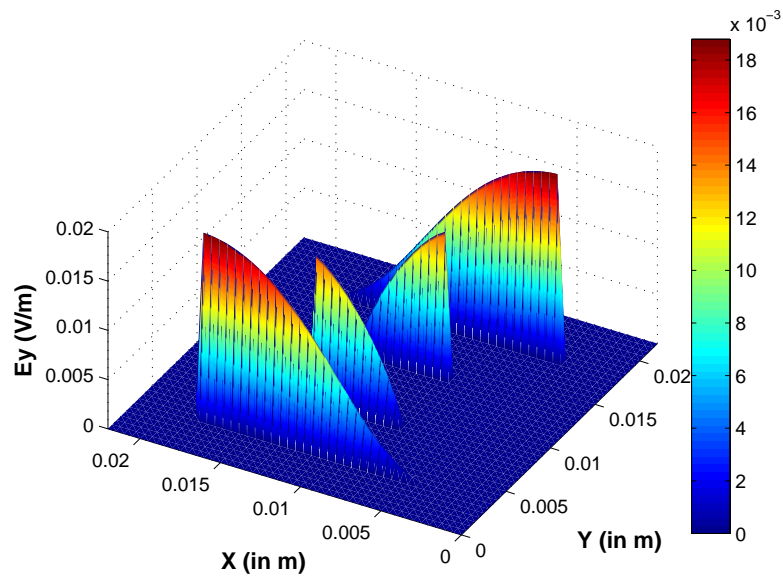
Figure 29: Electric field distribution along the y- direction of the power-ground structure with aperture.

and have similar port definitions, the response from these models can be expected to match very well. This is shown in Fig. 32.
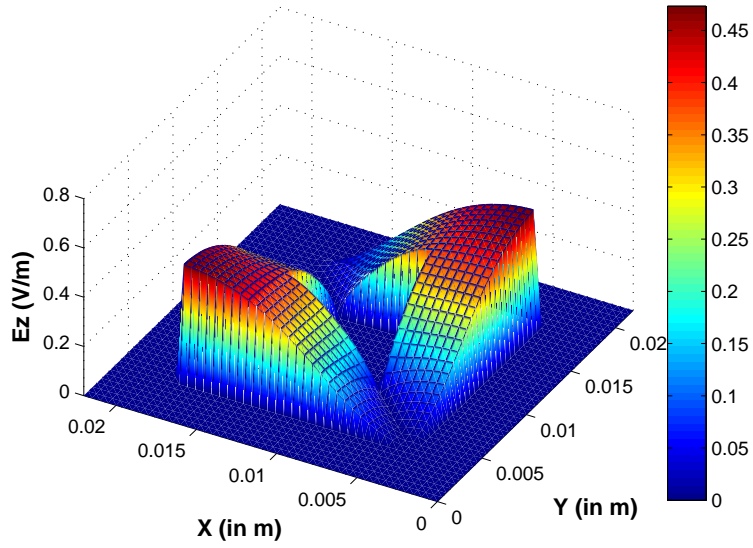
Figure 30: Electric field distribution along the z- direction of the power-ground structure with aperture.
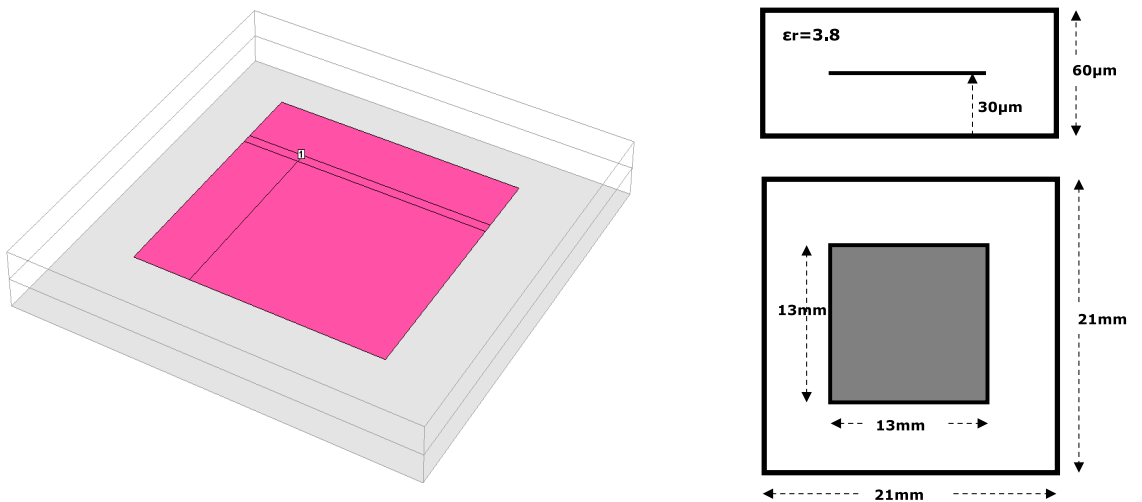
Figure 31: The layout, cross-section and the top-view of the 13mm power plane structure.

3.3.0.3   Three Plane Power Ground with Aperture

To further verify the accuracy of the SEEC model, a three-metal plane structure with aperture on the center plane is considered. The structure, with PEC boundaries and port placement is shown in Fig. 33. The discretization of the $22\ mm \times 22\ mm \times 80\ \mu m$

32
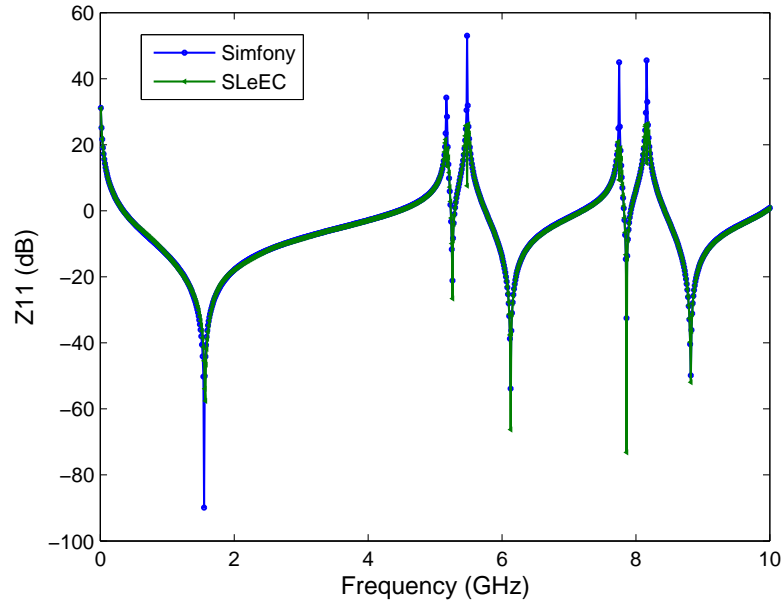
Figure 32: The impedance response of the 13mm plane structure obtained from the SEEC model compared to the Laguerre-FDTD method.

volume is done using a unit cell of 0.5 $mm \times 0.5$ $mm \times 10$ μm resulting in approximately 50, 000 unknowns. The dielectric constant of the homogeneous medium enclosed in the PEC box is 4.4. A comparison of the scattering parameters of the structure obtained from SEEC model with a commercial method of moments solver results in a good match, as shown in Fig. 34.

3.3.0.4   Lossy Power-Ground Structure

To validate the SEEC model inclusive of the dielectric losses, the same structure as shown in Fig. 33 was simulated assuming the loss tangent between the metal planes to be 0.025. A comparison of the results is shown in Fig. 35

3.4   Co-simulation of SEEC with Lumped-circuit Elements

The combined simulation of lumped circuit elements along with full-wave EM simulation is essential in solving many practical problems. For example, decoupling
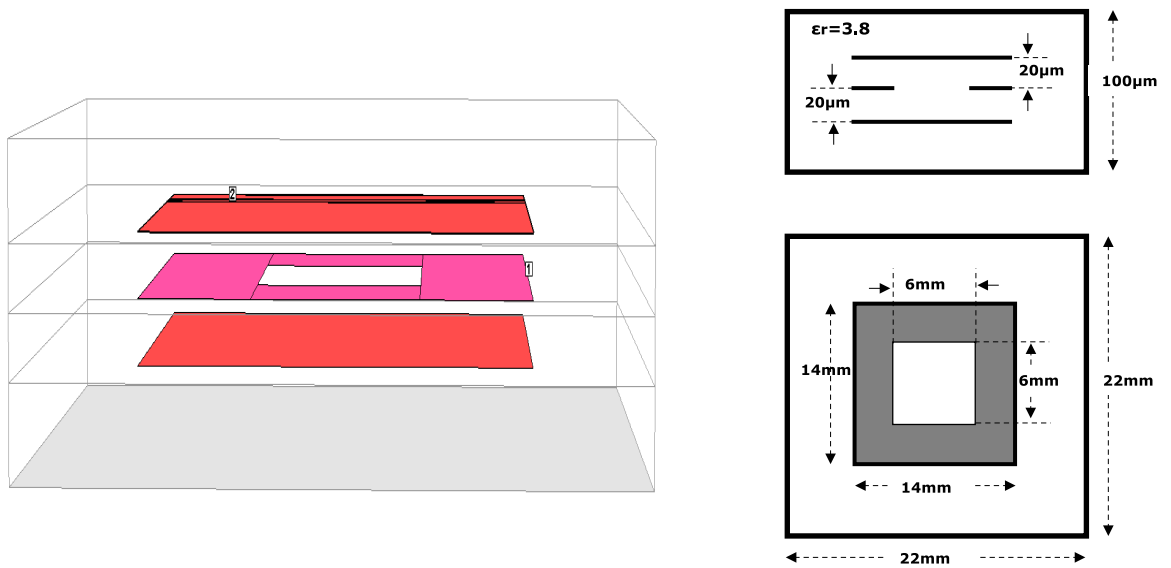
Figure 33: The layout, cross-section and top-view of the three plane power ground structure with aperture.
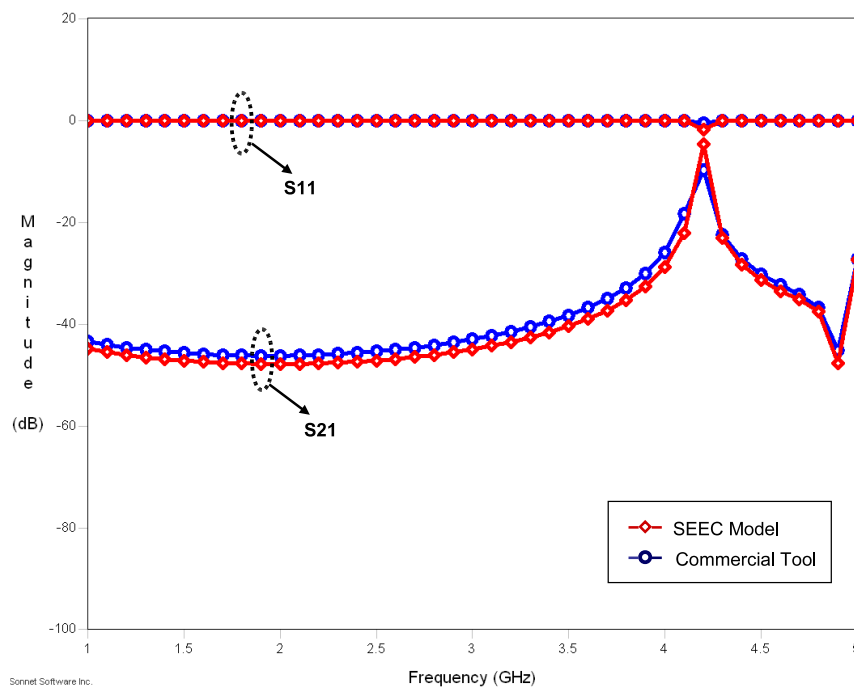
Figure 34: The scattering parameters of the three plane power-ground structure with aperture obtained from the SEEC model compared to a commercial method of moments solver.

capacitors (decaps) are commonly used to reduce the impedance profile of power distribution networks. An equivalent circuit representation of the decoupling capacitor,

34
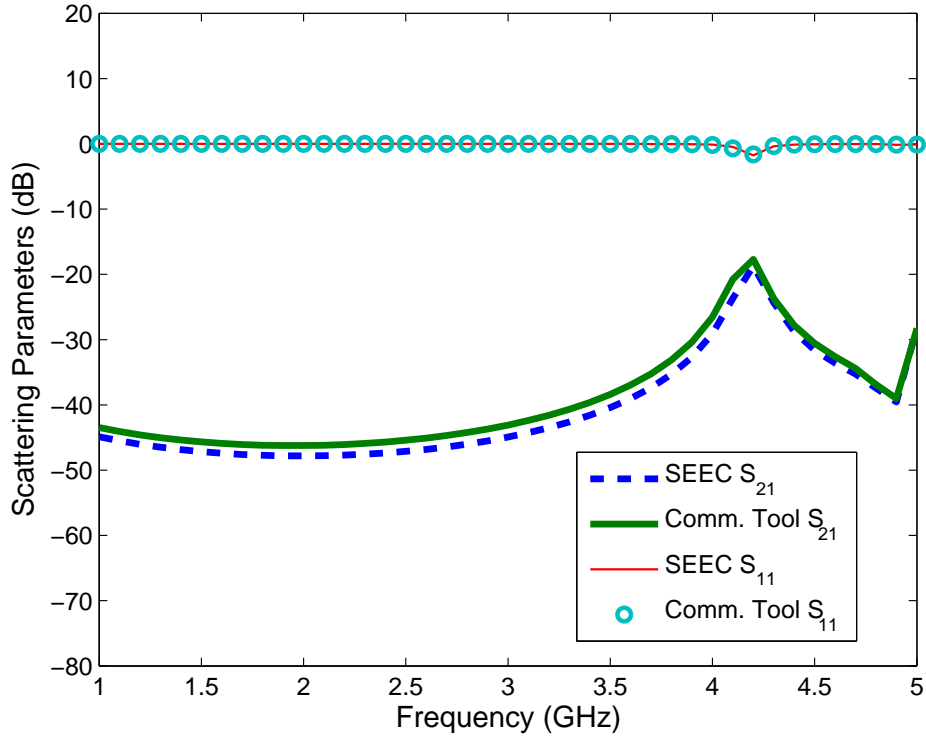
Figure 35: The scattering parameters of the three plane power-ground structure with aperture obtained from the SEEC model compared to a commercial method of moments solver, inclusive of dielectric losses.

inclusive of the parasitic equivalent series resistance (ESR) and equivalent series inductance (ESL) is shown in. Fig. 36. The inclusion of lumped elements in the SEEC model can be done in terms of an equivalent current density. For any lumped element with impedance, Z_{lumped}, placed in the Yee cell (with dimensions Δx, Δy, and Δz) along the z- direction, the current density is given as:

$$J_{lumped} = \frac{I_{lumped}}{Area_{cell}} = \frac{V_{lumped}}{Z_{lumped} \times Area_{cell}} \tag{23}$$

where, I_{lumped} and V_{lumped} are the current and voltage associated with the lumped circuit element, and $Area_{cell}$ is the cross-sectional area of the Yee cell. V_{lumped} in turn can be written in terms of the z- component of electric field, E_z, in the Yee cell as:

$$V_{lumped} = \sum_{z=ref}^{l} E_z \Delta z \tag{24}$$

35

Figure 36: The lumped element equivalent circuit for a decoupling capacitor.
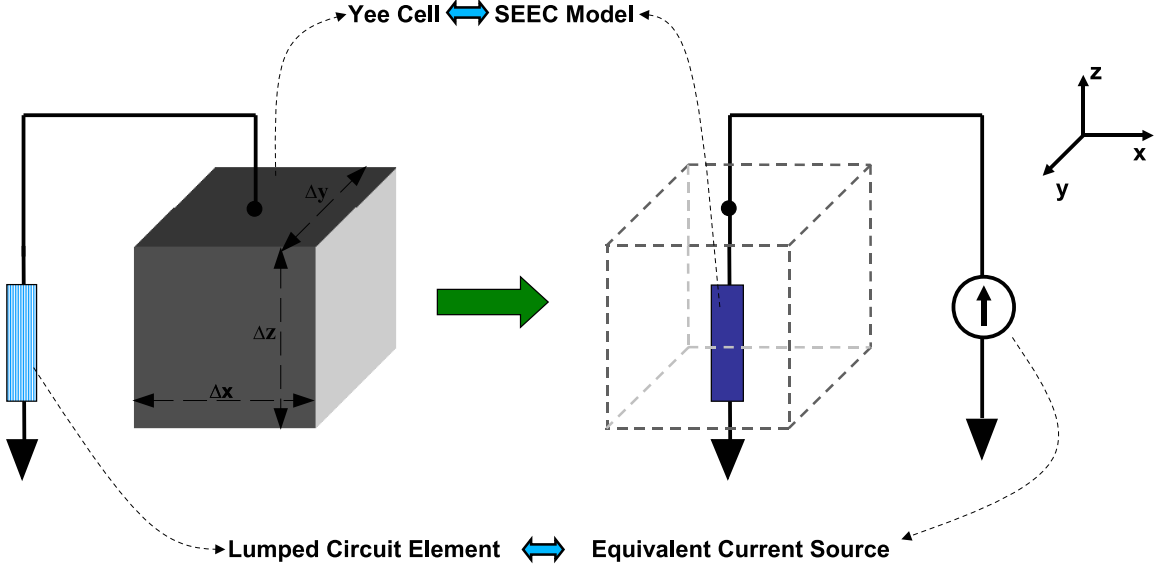
Figure 37: The model for co-simulation of the SEEC model with a lumped circuit element.

where, the lumped element is connected between the nodes ref and l. Thus the equivalent current source for the lumped circuit element to be included in the Yee cell is given as:

$$J_{lumped} = \frac{V_{lumped}}{Z_{lumped} \times Area_{cell}} = \sum_{z=ref}^{l} \frac{\Delta z}{\Delta x \Delta y} \frac{E_z}{Z_{lumped}} \tag{25}$$

The equivalent model inclusive of the lumped element is shown in Fig. 37.

3.4.1 Numerical Test Cases

3.4.1.1 Decoupling Capacitors Resonances

The final example to be considered is that of placing a single decoupling capacitor between the plane pair as shown in Fig. 38. The dimension of the plane is 250 mm × 250 mm. The entire structure is discretized using a unit cell of size 10 mm × 10 mm × 0.2 mm with a dielectric constant of 4.4 between the planes. A decoupling capacitor with parameters $ESL = 2.53 \ nH$ and $C = 100 \ nF$ is placed at the port,
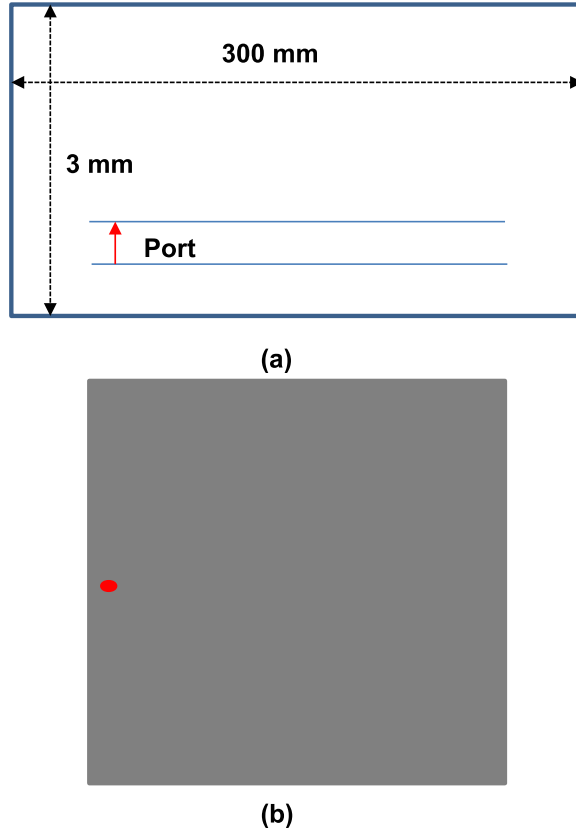
Figure 38: The layout of the plane pair showing (a) the cross-section and (b) the top-view.

causing a resonance and an anti-resonance, captured in the frequency response. The response of the structure, with and without decoupling capacitors, is shown in Fig. 39.

3.4.1.2   Power Plane with Decoupling Capacitor

Next we consider an example of full-wave SEEC/ lumped circuit element co-simulation. A two-metal plane power-ground structure is considered. The structure, with PEC boundaries and port placement is shown in Fig. 40. The discretization of the $21\ mm \times 21\ mm \times 90\ \mu m$ volume is done using a unit cell of $1\ mm \times 1\ mm \times 10\ \mu m$ resulting in approximately $15,000$ unknowns. The dielectric constant of the homogeneous medium enclosed in the PEC box is 3.8. A comparison of the self impedance of the structure obtained from SEEC model of the power-ground structure, with and
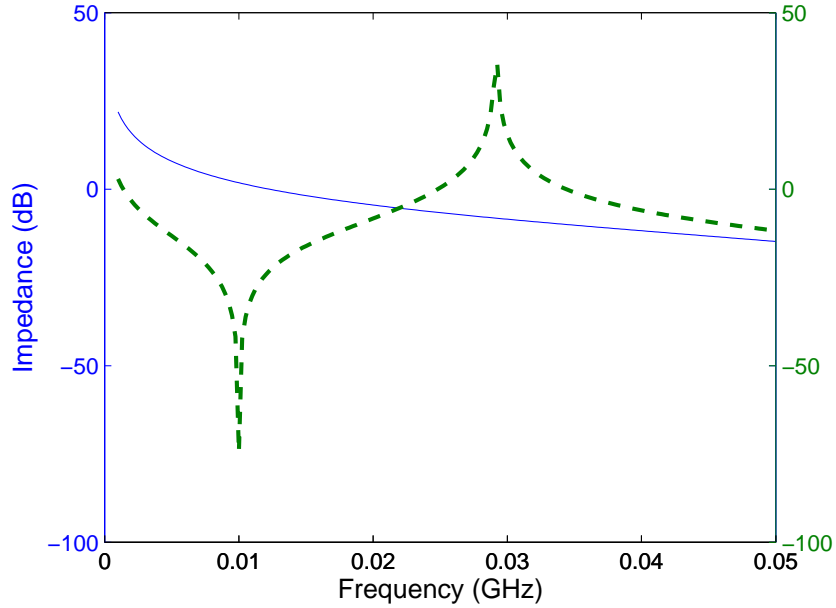
Figure 39: The response of the structure without decoupling capacitors (solid) and with decoupling capacitors (dashed).

without decaps, is shown in Fig. 41. The relevant values of the decoupling capacitor are: $ESR = 15.9\Omega$, $ESL = 0.54nH$ and $C = 179.9nF$. A total of 25 decoupling capacitor spread throughout the plane structure are used, resulting in a significant decrease in the self impedance.

3.5 Complexity Scaling

Complexity analysis for the quasi-minimal residual method has been well-studied. The memory complexity of the process is $O(Nlog(N))$, thus affording the solution of large test cases. The computational complexity of the process is $O(rlog(Nz(\mathbf{A})))$, where r is the number of iterations of the solver, and $Nz(\mathbf{A})$ is the number of non-zeros in the system matrix $\mathbf{A}$. Results of the complexity analysis done on a 32-bit machine with 2 GB RAM with an Intel Core 2 Duo E4500 processor are shown in Fig. 42.

The code was also ported to a 64-bit quad-core personal computer with 48GB RAM. Preliminary investigation showed good scaling of the memory and time per
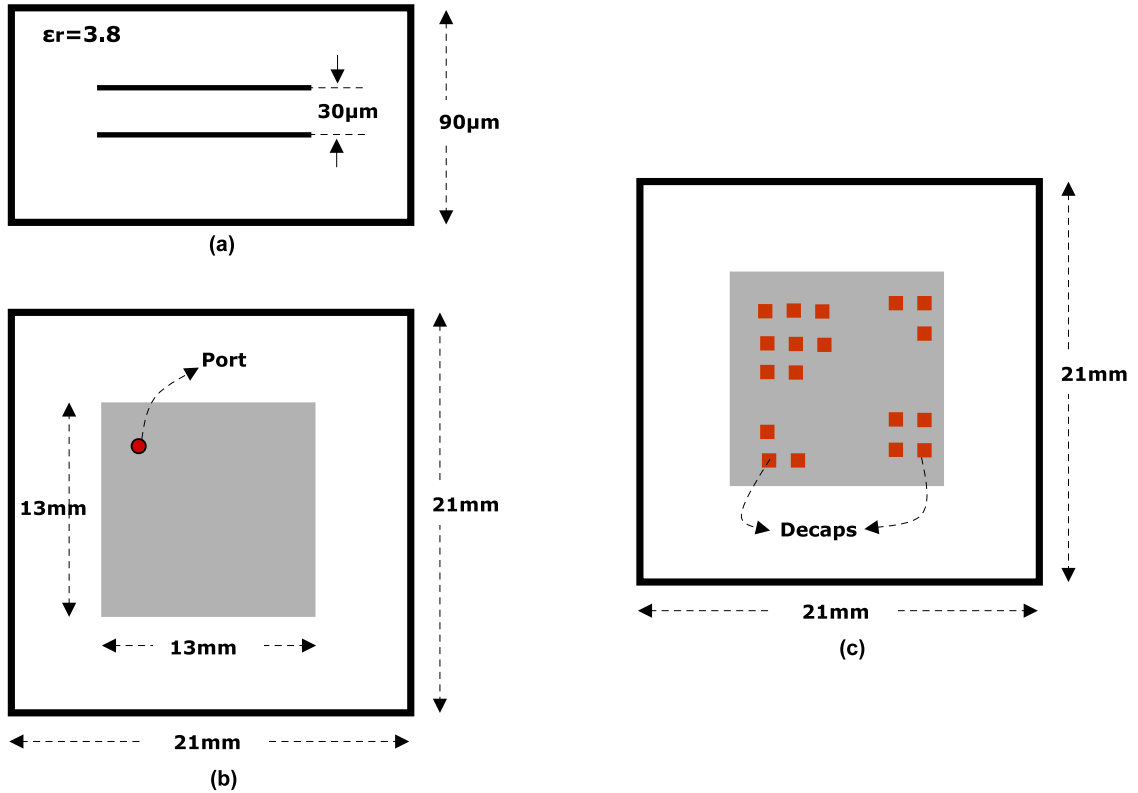
Figure 40: The (a)cross section and (b) top-view of the power plane pair structure. (c) shows a top-view illustration of decoupling capacitor distribution between the plane pair.

iteration of the simulation, as shown in Fig. 43.

3.6 Summary

A second order equivalent circuit framework for electromagnetic simulation has been shown. The corresponding circuit equivalent form, SEEC model, was shown for one-, two- and three- dimensional cases. Since the equivalent circuit form is a direct representation of the Maxwell's equation, all electromagnetic effects can be captured accurately. Lumped components can be included by means of a voltage dependent current density term. The second order nature of the model translates into half the number of unknowns as the first order form, but more importantly, presents important properties for model order reduction.
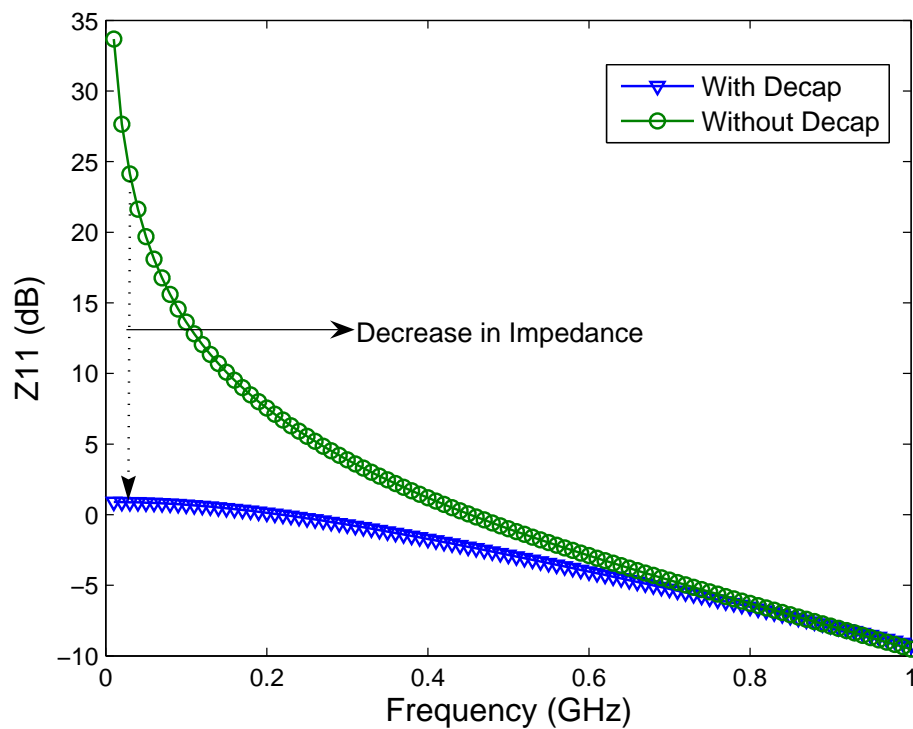
Figure 41: The impedance response of the power plane pair, with and without decoupling capacitors.
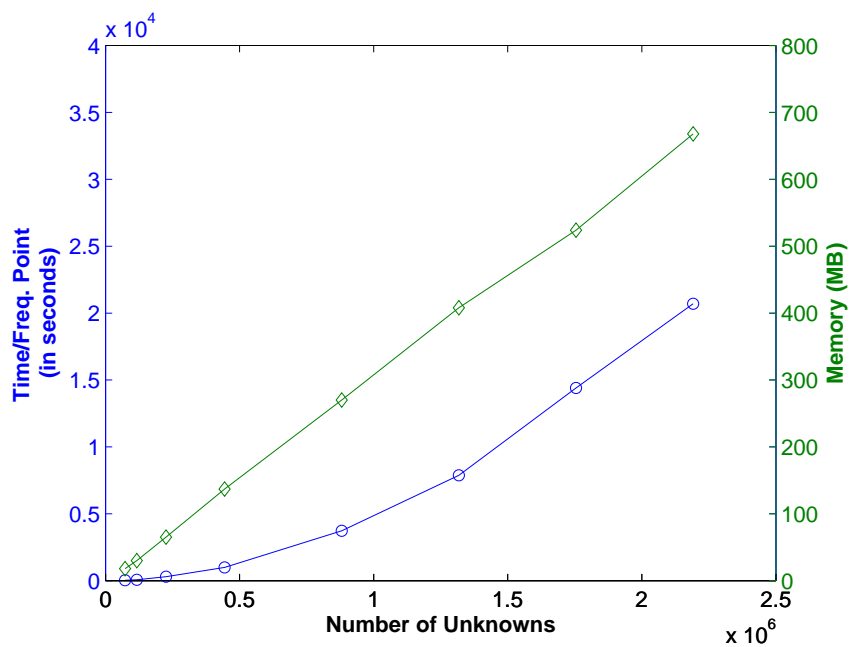
Figure 42: The scaling of computational complexity (circles) and memory complexity (diamonds).
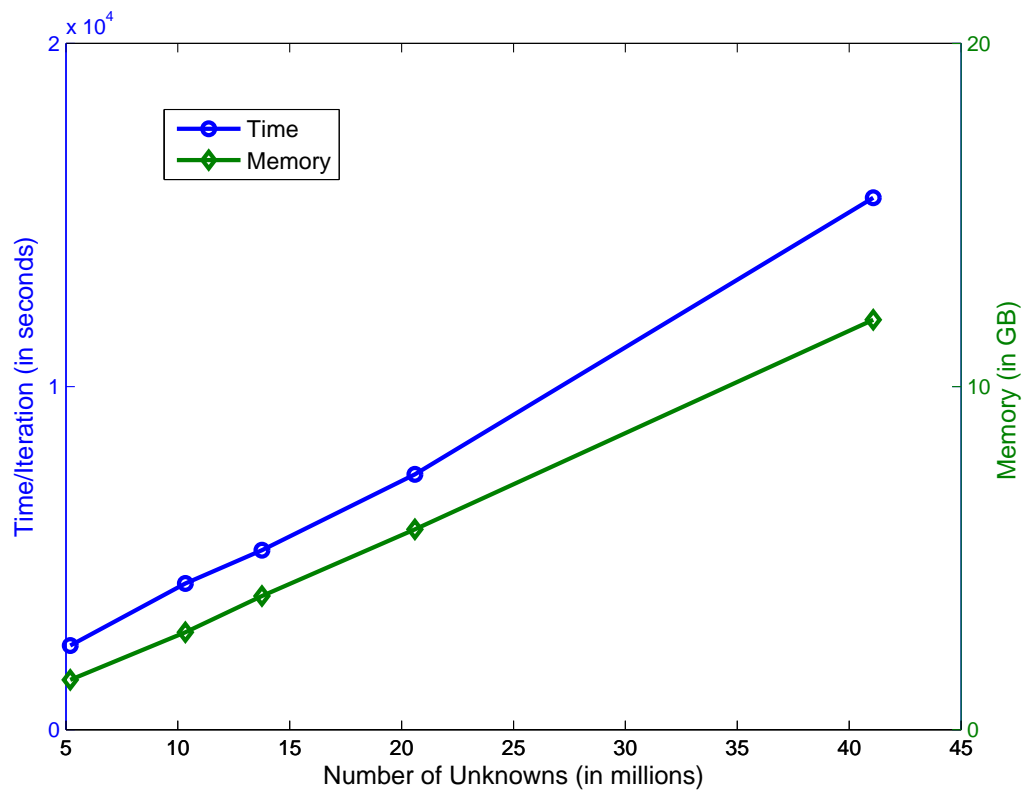
Figure 43: Results for complexity scaling on the 64 bit machine.

CHAPTER IV

EFFICIENT MODEL ORDER REDUCTION OF SEEC MODEL

4.1   Introduction

As has been discussed in the previous chapter, the focus of model order reduction (MOR) methods have been primarily towards the first order methods. To work with the SEEC model, an investigation into suitable second order methods of MOR needs to be done. The focus of this chapter is to intoduce an existing method of MOR, which can work on SEEC model, and then to demonstrate its application through numerical examples.

4.2   Preliminaries

In this section a few definitions and theorems are necessary, which are described below. Consider a linear system in Laplace domain, given by a system of equations known as the descriptor form:

$$s\mathbf{E}\mathbf{x}(s) = \mathbf{A}\mathbf{x}(s) + \mathbf{b}\mathbf{u}(s) \tag{26a}$$

$$\mathbf{y}(s) = \mathbf{l}^T\mathbf{x}(s) \tag{26b}$$

where, $\mathbf{x}$ is the vector of descriptors, $\mathbf{u}$ and $\mathbf{y}$ are the input and output variables, respectively, $\mathbf{A}, \mathbf{E} \in \mathbb{R}^{N \times N}$, $\mathbf{b}, \mathbf{l} \in \mathbb{R}^N$. The transfer function for the above system is then given as:

$$\mathbf{H}(s) = \mathbf{l}^T(s\mathbf{E} - \mathbf{A})^{-1}\mathbf{b}. \tag{27}$$

Definition 1: Let $\mathbf{A} \in \mathbb{C}^{N \times N}$ be a given matrix and $\mathbf{b} \in \mathbb{C}^N$ be a known vector,

then the qth order Krylov subspace generated by these quantities is defined as:

$$\mathcal{K}_q(A, b) = span\left\{\mathbf{b}, \mathbf{Ab}, \mathbf{A}^2\mathbf{b}, \ldots, \mathbf{A}^q\mathbf{b}\right\}, \quad q \in \mathbb{Z}^+. \tag{28}$$

The one-sided projection Krylov subspace reduction is defined to be the operation of pre- and post- multiplication by a suitable matrix, $\mathbf{Q} \in \mathbb{C}^{N \times q}$ such that the original system is transformed into a reduced system given by

$$s\mathbf{Q}^T\mathbf{EQz}(s) = \mathbf{Q}^T\mathbf{AQz}(s) + \mathbf{Q}^T\mathbf{bu}(s) \tag{29a}$$

$$\mathbf{y}(s) = \mathbf{l}^T\mathbf{Qz}(s) \tag{29b}$$

Theorem 1: If we choose a projection matrix $\mathbf{Q}$ for one-sided projection on (26) such that,

$$colsp\left\{\mathbf{Q}\right\} = \mathcal{K}_q(\mathbf{A}^{-1}\mathbf{E}, \mathbf{A}^{-1}\mathbf{b}), \tag{30}$$

then, the reduced system matches up to q moments of the original system's transfer function.

4.3   Inherently Passive MOR

A passive reduction of MOR for susceptance based elements was recently proposed in [60]. We first start with (22). We choose the point of expansion to be s_o and scale the frequencies by using the following coordinate transformation:

$$z = -\frac{1}{s_o}(s - s_o). \tag{31}$$

An auxiliary quantity is then introduced,

$$Y(z) = \frac{1}{1 - z}X(z). \tag{32}$$

Using the method of moments technique, and expanding $X(z)$, $Y(z)$ and $I(z)$ in powers of z,

$$\left\{\mathbf{C}s_o(1 - z) + \mathbf{G}\right\}\left\{\mathbf{X}_0 + \mathbf{X}_1z + ...\right\} + \frac{\Gamma}{s_o}\left\{\mathbf{Y}_0 + \mathbf{Y}_1z + ...\right\}$$

$$= \mathbf{B}\left\{\mathbf{I}_0 + \mathbf{I}_1z + ...\right\}. \tag{33}$$

43

Equating like powers of z,

$$\Upsilon_o X_k = \mathbf{C} s_o \mathbf{X}_{k-1} - \frac{\Gamma}{s_o} \mathbf{Y}_{k-1} + \mathbf{B} \mathbf{I}_k \qquad (34)$$

where the following equations complete the recursive formulation for matching the electric field moment vectors:

$$\Upsilon_o = \left(\mathbf{G} + \mathbf{C} s_o + \frac{\Gamma}{s_o} \right) \qquad (35)$$

$$\mathbf{Y}_k = \mathbf{X}_k + \mathbf{Y}_{k-1} \qquad (36)$$

$$\mathbf{Y}_{-1} = \mathbf{X}_{-1} = 0. \qquad (37)$$

The orthogonalization process used in [60] presented stability concerns due to the auxiliary variable $Y(z)$, which was eliminated in [80] by making use of the following summation:

$$\mathbf{Y}_k = \sum_{l=0}^{k} \mathbf{X}_l. \qquad (38)$$

Substituting (38) in (35), we get the following set of equations:

$$\mathbf{X}_k = \mathbf{P} \mathbf{X}_{k-1} + \mathbf{R} \sum_{l=0}^{k-1} \mathbf{X}_l \qquad (39)$$

$$\mathbf{X}_{-1} = 0 \qquad (40)$$

$$\mathbf{X}_0 = \Upsilon_o^{-1} B \qquad (41)$$

where, $\mathbf{P}$ and $\mathbf{R}$ amplification matrices are given by:

$$\mathbf{P} = \Upsilon_o^{-1} \mathbf{C} s_o \qquad (42)$$

$$\mathbf{R} = \Upsilon_o^{-1} \frac{\Gamma}{s_o} \qquad (43)$$

Further details on the procedure for generation of the subspace can be found in [80]. By limiting the number of terms in the summation in (39) to two, the process limits the effect of roundoff errors. It is to be noted that the column space of the projection matrix forms the Krylov subspace of order q, $\mathcal{K}_q$. There still remains

the issue of terminating the recursive calculation at an appropriate level. As has been the case with other approaches, the iterative process is terminated when a particular level of convergence has been reached. This can be determined by checking for the difference between successive iterations and after a predetermined tolerance is achieved, the final projection matrix is formed. Also, on-the-fly deflation is done during the orthogonalization process to keep it stable. Once the projection matrix has been formed, the original system matrix is reduced resulting in the following governing equation for the reduced system:

$$\left(\tilde{\mathbf{G}} + \tilde{\mathbf{C}}s + \frac{\tilde{\Gamma}}{s}\right)\tilde{\mathbf{V}} = \tilde{\mathbf{B}}\tilde{\mathbf{I}} \tag{44}$$

where,

$$\tilde{\mathbf{G}} = \mathbf{Q}^T\mathbf{G}\mathbf{Q}, \ \tilde{\mathbf{C}} = \mathbf{Q}^T\mathbf{G}\mathbf{Q}, \ \tilde{\Gamma} = \mathbf{Q}^T\Gamma\mathbf{Q} \tag{45}$$

$$\tilde{\mathbf{B}} = \mathbf{Q}^T\mathbf{B}, \ \tilde{\mathbf{I}} = \mathbf{I}\mathbf{Q}, \tag{46}$$

This reduced system, obtained as a result of the one-sided projection, matches up to q moments of the original system's transfer function.

4.3.1 Passivity and Reciprocity

The issue of passivity presents a significant problem in model order reduction methods and therefore its definition is now presented.

Definition 2: For the impedance matrix, $Z(s)$ to be passive, it has to satisfy the following conditions [56, 69]:

1. $Z(s)$ is a rational function of s.

2. $Z(s^*) = Z^T(s)^*$.

3. $z^*(Z(s) + Z^*(s))z \geq 0$, $\forall z \in \mathbb{C}$, and $\forall s \in \mathbb{C}$ with $\Re(s) > 0$.

In the case of the susceptance element equivalent circuit model governed by (22), the impedance response is given as

$$\mathbf{Z}(s) = \mathbf{B}^T \left(\mathbf{G} + \mathbf{C}s + \frac{\Gamma}{s} \right)^{-1} \mathbf{B}. \tag{47}$$

Condition 1 is easily satisfied since the inverse of a rational function, (47), is also rational. With $\mathbf{G}$, $\mathbf{B}$ and Γ being real-valued, condition 2 is also readily satisfied, since it involves only the conjugates of s. As stated in [60], proof for Condition 3 can be obtained by rewriting it as

$$z^* \mathbf{B}^T \left\{ \Upsilon^{-1} + (\Upsilon^{-1})^* \right\} \mathbf{B}z \geq 0, \tag{48}$$

where, $\Upsilon = \mathbf{G} + \mathbf{C}s + \Gamma/s$. This can be rewritten as

$$z^* \mathbf{B}^T (\Upsilon^{-1})^* \left\{ \Upsilon^* + \Upsilon \right\} \Upsilon^{-1} \mathbf{B}z \geq 0. \tag{49}$$

Substituting for Υ with its constituent terms, taking $s = \alpha + j\omega$ and $\eta = \Upsilon^{-1}\mathbf{B}z$,

$$\eta^* \left\{ (\mathbf{G} + \mathbf{G}^T) + \alpha(\mathbf{C} + \mathbf{C}^T) + \frac{\alpha}{s^2}(\Gamma + \Gamma^T) \right\} \mathbf{B}\eta \geq 0. \tag{50}$$

If the matrices $\mathbf{G}, \mathbf{C}$, and Γ are positive semidefinite, the above condition holds true. A similar proof for first order reduction can be found in [48], along with proof that one-sided projection of matrices will not change this requirement. However, this reduced system may not be passive due to discretization and/or roundoff errors. To provide an additional check, as in [9], the scattering parameters obtained from the reduced model are noted and checked for the unitary boundedness condition

$$\mathbf{S}^T\mathbf{S} - \mathbf{I} \leq 0, \tag{51}$$

where, $\mathbf{S} \in \mathbb{C}^{p \times p}$ is the scattering parameter matrix and $\mathbf{I}$ is the $p \times p$ identity matrix.

Theorem 2: The application of the improved efficient nodal order reduction algorithm also preserves reciprocity, an important property of the transfer functions of passive networks.

This is true, since in the impedance response given by (47), $\mathbf{G}$, $\mathbf{C}$, and Γ are symmetric, making $\mathbf{Z}(s)$ reciprocal among its ports.

4.3.2 Projection Matrix Calculation

The calculation of electric field moments presents a computational challenge. Conventional means employed for model order reduction employ direct methods such as LU decomposition or QR factorization, which for sparse matrices work very well. However, the required memory scales very quickly as the problem size increases. Keeping in mind the need for fast frequency sweep and the fact that many electromagnetic problems would be typically large, it is best to opt for an iterative solution. Here the biconjugate gradient process, QMR [20], is used. Due to its conjugate gradient-like memory requirements of $O(Nlog(N))$, where N is the number of unknowns, it is possible to address larger problems. As compared to the generalized minimal residual (GMRES) method [58], QMR offers advantages of 1) storing only three vectors in memory for the recursive calculation of the basis, as against all basis vectors and 2) use of look-ahead strategies to avoid cases of near-breakdown. Near breakdown is said to occur when, though the vector calculated in current iteration might be nearly zero, the vectors in successive iterations are well-behaved. More details can be found in [20]. The iterative process can be accelerated through the use of suitable preconditioners. Consider a linear equation of the form

$$\mathbf{Ax} = \mathbf{b}. \tag{52}$$

Then the introduction of a preconditioner, $\mathbf{M}$, modifies this equation to be of the form

$$\mathbf{M}^{-1}\mathbf{Ax} = \mathbf{M}^{-1}\mathbf{b}, \tag{53}$$

which converges to a solution faster, since the condition number of the coefficient matrix $\mathbf{M}^{-1}\mathbf{A}$ is much smaller than that if $\mathbf{A}$. The main properties of an effective preconditioner are that it should be as close to the original system matrix as possible, and it should be computationally inexpensive. It is observed that the system matrix used for the calculation of the moment vectors is essentially similar to the Helmholtz
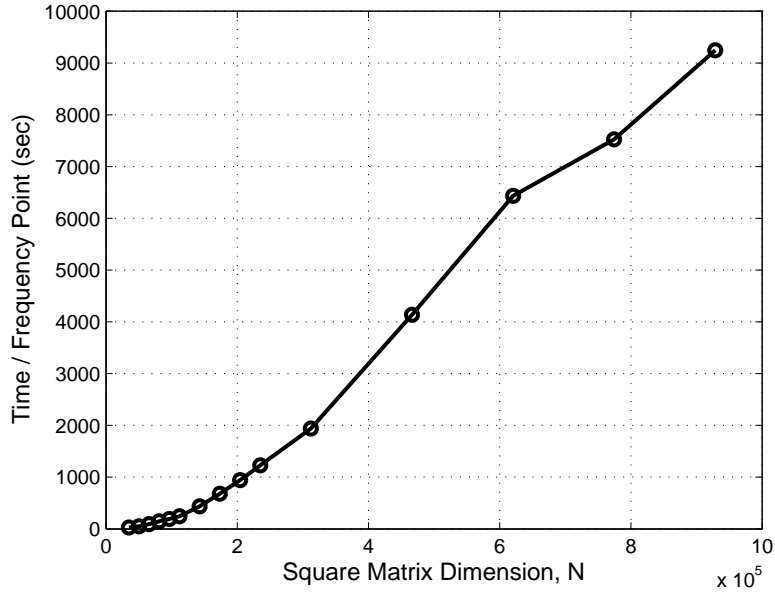
Figure 44: The time taken per iteration by the solver as the matrix dimension increases.

operator. Preconditioner for the Helmholtz operator is a well studied field [36, 42]. The complex space shifted diagonal preconditioner is used, which is a simple, yet stable and effective preconditioner for the Helmholtz operator. The advantage of using the shifted diagonal preconditioner is primarily two-fold: 1) The cost of calculating the preconditioner is trivial, and 2) the introduction of the imaginary shift prevents any clustering or crossing of the eigenvalues of the preconditioned matrix around zero. Detailed discussions about the use of the complex shifted preconditioner and its effects on the eigenvalues of the preconditioned matrix, and therefore the stability and convergence properties of the iterative solution can be found in [42]. An imaginary shift of 0.5 is chosen for the test cases presented in this thesis. The scalability of the solver on a 32-bit platform in a MATLAB environment is shown in Fig. 44. The computational complexity of conjugate gradient type processes is $O(rNz(\mathbf{A}))$, where r is the number of iterations of the solver, $Nz(\mathbf{A})$ is the number of non-zeros in the system matrix $\mathbf{A}$.
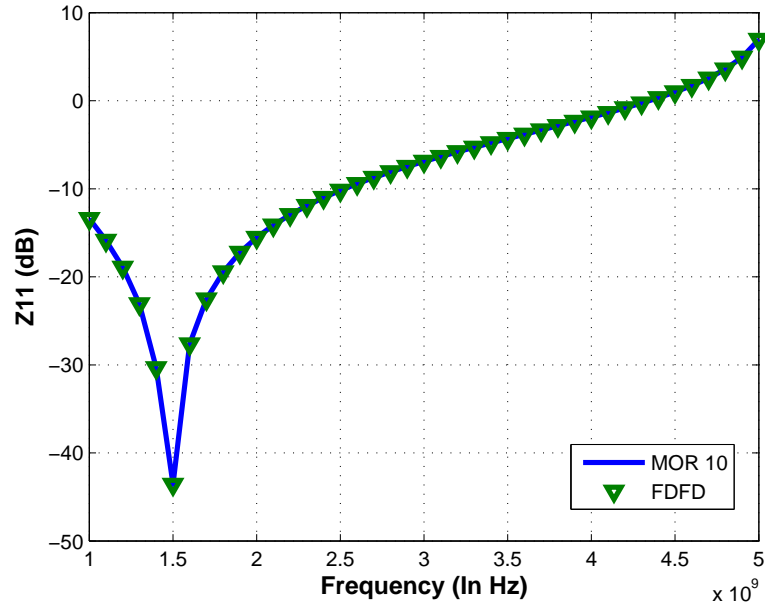
Figure 45: The impedance response of the 13mm plane structure obtained from the reduced model compared to the full-wave SEEC model.

4.4   Numerical Test Cases

In this section the efficiency and scalability of the imp-ENOR algorithm for SEEC models is demonstrated with test cases.

4.4.0.1   Power Plane

The first test case considered is the 13 *mm* power plane structure shown in Fig. 31. The improved-ENOR algorithm is applied and the model-order is reduced to a system of order 10. Fig. 45 shows a favorable comparison of the reduced model and the full-wave 3D SEEC model. The average time per frequency point for the full 3D simulation was of the order of 20 s, whereas that for the reduced-order system was on the order of tenths of milliseconds.

4.4.0.2   Power Ground Structure with Via

To verify the accuracy of the equivalent-circuit based full-wave simulation followed by the improved ENOR approach, a power-ground structure, as shown in Fig. 46, is
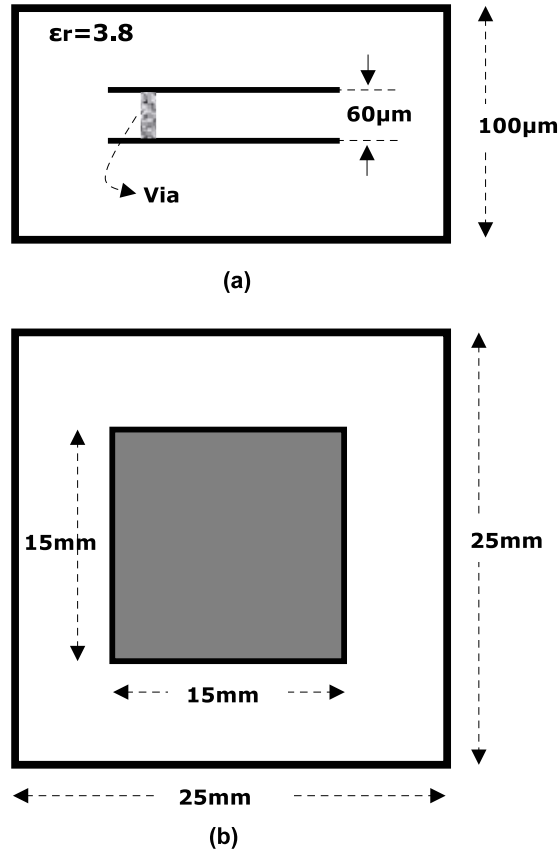
Figure 46: The (a) cross-section and (b) top-view of the power-ground structure connected by a via.

simulated. Two 15 mm × 15 mm thin metal planes connected by a via are considered, placed in a homogeneous medium of dielectric constant 4.5, enclosed in a PEC box of dimensions 25 mm × 25 mm × 80 μm. A unit cell of 0.5 mm × 0.5 mm × 10 μm was used to discretize the structure shown in Fig. 46. The imp-ENOR algorithm is applied and the model-order is reduced to 15. Fig. 47 shows a favorable comparison of the reduced model and the full-wave 3D SEEC model simulation. The average time per frequency point for the full 3D simulation was of the order of 120 s, whereas the reduced-order system response took on the order of tenths of milliseconds per frequency point.
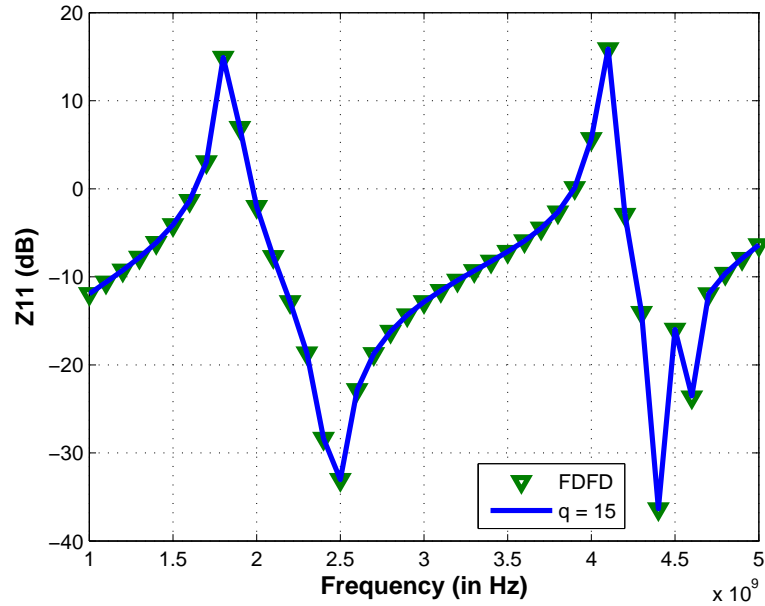
Figure 47: The impedance response of the power-ground structure shorted by a via, obtained from the reduced model and the full-wave SEEC model.

4.4.0.3 Test Structure - Power Ground Structure with Aperture

To demonstrate the convergence of the solution as the order of the reduced system is increased, a three-metal plane structure with aperture on the top plane, as shown in Fig. 33 is considered. The improved-ENOR algorithm is then applied, with the number of poles varying as 2, 5 and 10 poles. Fig. 48 and 49 shows the self and transfer impedance response of the two-port system for this set-up. As can be seen, as the number of poles is increased the system response converges to the full-wave simulation. Whereas the 2-pole system is inadequate, the 5-pole system starts to diverge at frequencies above 4.5GHz. The 10-pole reduced order system shows a good match with the full-wave simulation results. The average time per frequency point for the full 3D simulation was of the order of 180 s, whereas for the reduced-order system response took on the order of tenths of milliseconds.

51
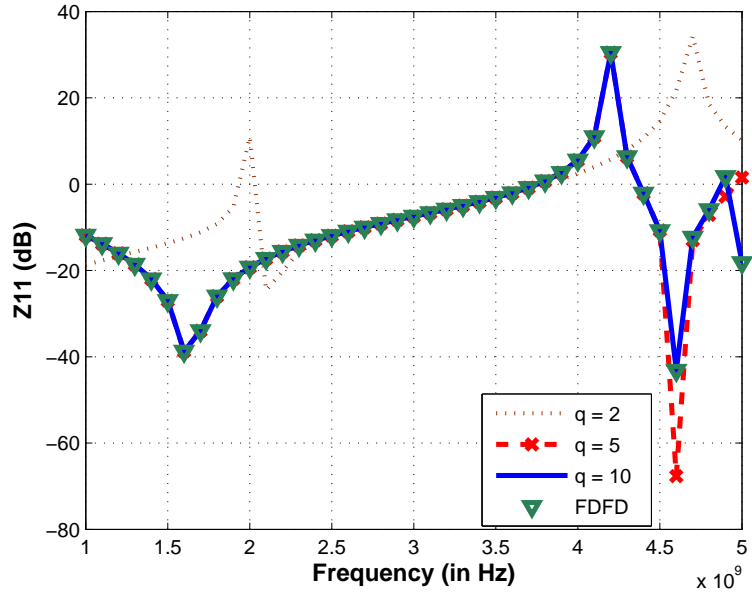
Figure 48: The self impedance of the three plane power ground structure with aperture, obtained from the reduced model compared to the full-wave SEEC model.
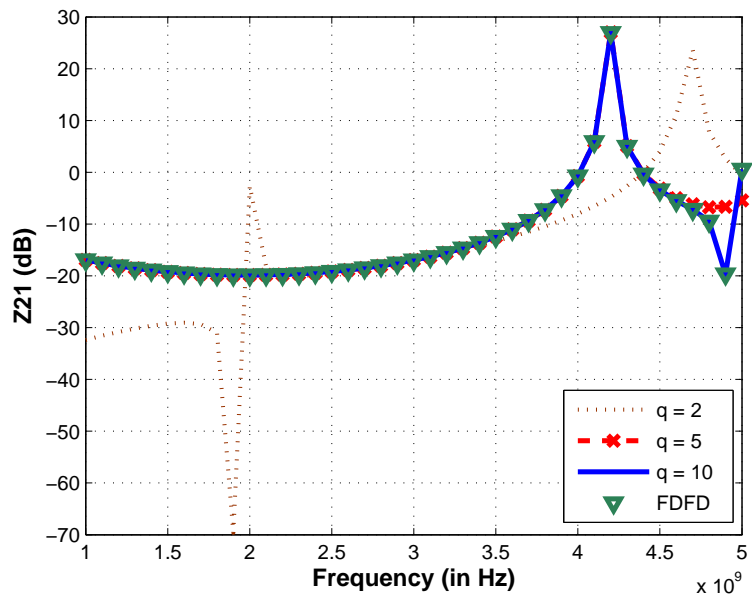
Figure 49: The transfer impedance of the three plane power ground structure with aperture, obtained from the reduced model compared to the full-wave SEEC model.

4.4.0.4   Test Structure - 2.4GHz Band-pass Filter

The test structure now considered is that of a 2.4 GHz band-pass filter structure shown in Fig. 50. It is a multilayer structure in a homogeneous medium of dielectric

constant, $\epsilon_r = 3.51$. The structure on metal layer M0 is repeated on metal layer M1. The linewidth of the larger inductor is 150 μm and the spacing is 100 μm and its dimensions are 1200 μm × 950 μm. The smaller inductor has a linewidth of 200 μm and a spacing of 100 μm and its dimensions are 900 μm×700 μm. The larger capacitor has dimensions of 1050 μm × 300 μm and the smaller capacitor has dimensions of 1200 μm × 100 μm. The square vias are 100 μm × 100 μm. The entire structure enclosed in a PEC box is discretized using a unit cell of 50 μm × 50 μm × 20 μm resulting in a total of 220, 000 unknowns. The SEEC model is then extracted from this discretization as described in Section II. Then the passive reduction process using a single point of expansion is applied to this model. A comparison of the insertion loss of the reduced model as compared to the original full-wave model is shown in Fig. 54. The corresponding comparison for the return loss is shown in Fig. 55. The frequency at which the expansion is done is 2.5 GHz. The electric field distribution of the structure along the x-, y- and z- directions is shown in Fig. 51, Fig. 52, and Fig. 53, respectively. A very close representation of the full-wave model is obtained and therefore the accuracy of the reduction process is validated. The computational cost of reduction is primarily comprised of the solutions to the twenty linear equations during the recursive calculation of the projection matrix. This is however, a considerably lower cost as compared to running a fine frequency sweep of the original full-wave model.

4.4.0.5 Test Structure - 5GHz Band-pass Filter

Consider a multilayer 5 GHz bandpass filter enclosed in a PEC box of dimensions 4 mm × 4 mm × 280 μm shown in Fig. 56. The box is filled with a homogeneous medium with dielectric constant 3.8. Discretizing the structure using a unit cell of dimensions 0.05 mm × 0.05 mm × 20 μm results in approximately 300, 000 unknowns. It is a multilayer structure in a homogeneous medium of dielectric constant, $\epsilon_r = 3.51$.
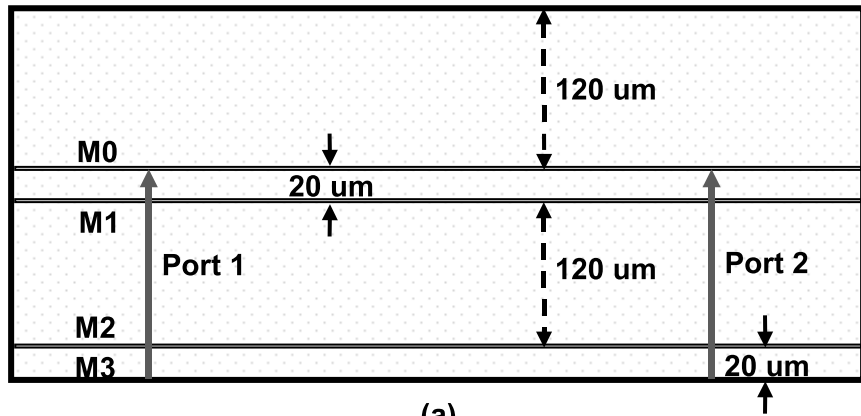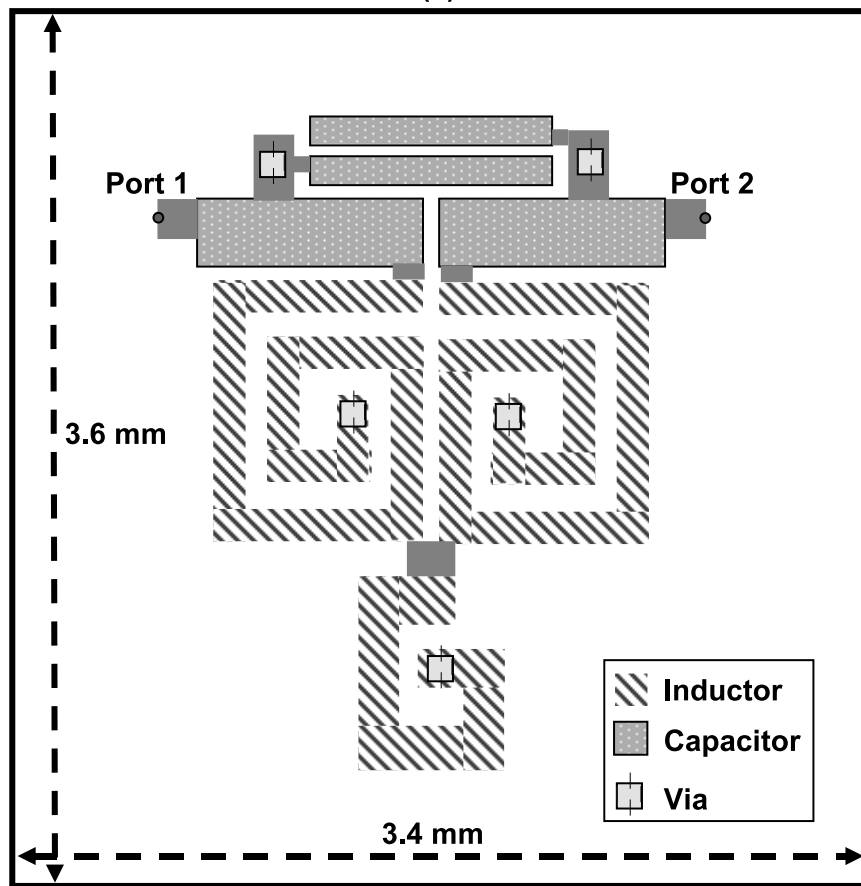
Figure 50: The (a) cross-section and (b) the top-view of the layout of the M0 layer of 2.4 GHz band-pass filter structure.

The structure on metal layer M0 is repeated on metal layer M1. The inductors, capacitors, and vias have the same feature dimensions as in the previous test case. The insertion loss response of the structure for the original and the reduced system is
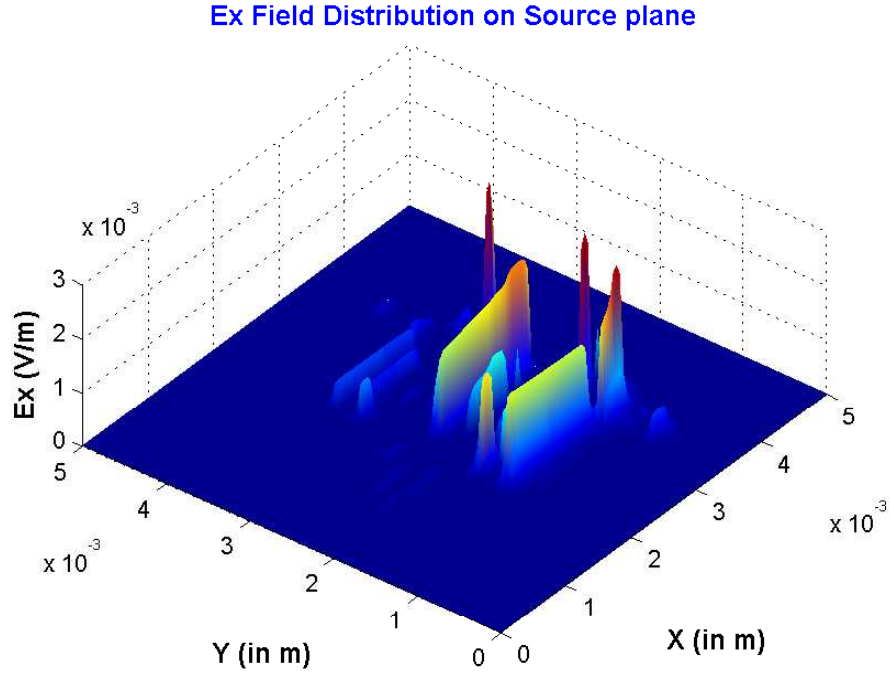
Figure 51: Electric field distribution along the x- direction of the band-pass filter structure at 2 GHz.

shown in Fig. 57. The corresponding comparison for the return loss of the structure for the original and reduced system is shown in Fig. 58. A high level of accuracy is obtained with the passive reduced order model over a frequency range from 1 GHz to 8 GHz.

For all the test cases described above, it is to be noted that if a factorization for the Υ matrix is available, the total time and memory overhead is corresponds to just one solution of the linear system. However, when such a factorization cannot be calculated, the time and memory overhead is equal to that associated with q solutions of the system equations.

4.5   *Summary*

A model order reduction scheme, the imp-ENOR method, has been successfully applied to the SEEC model, resulting in a smaller reduced system. By virtue of its
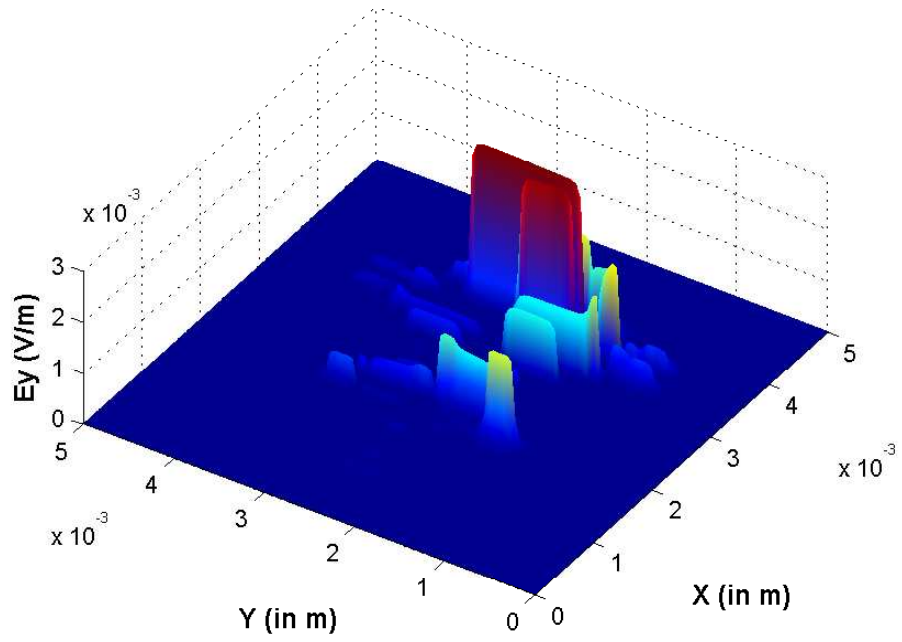
Figure 52: Electric field distribution along the y- direction of the band-pass filter structure at 2 GHz.

application to the second order form of SEEC model, properties of passivity and reciprocity are well preserved. To check for passivity violations due to round-off error, the scattering parameters are checked for the unity boundedness. Application of the algorithm to power ground and a band-pass filter structure were shown, where the reduction in size translated to a much smaller frequency sweep time (of the order of milliseconds).
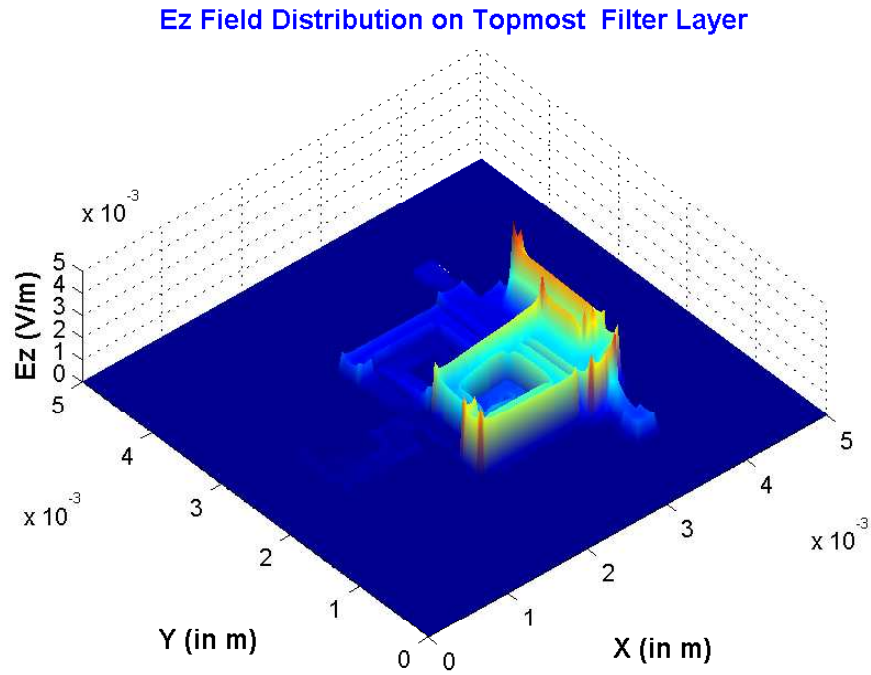
Figure 53: Electric field distribution along the z- direction of the band-pass filter structure at 2 GHz.
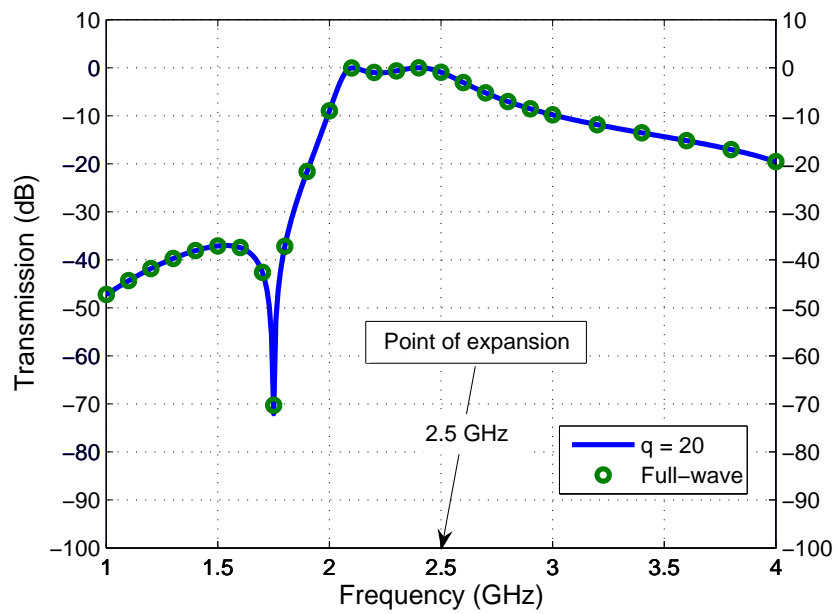
Figure 54: The insertion loss of the reduced model of order 20 compared to the original full-wave simulation of the band-pass filter structure layout
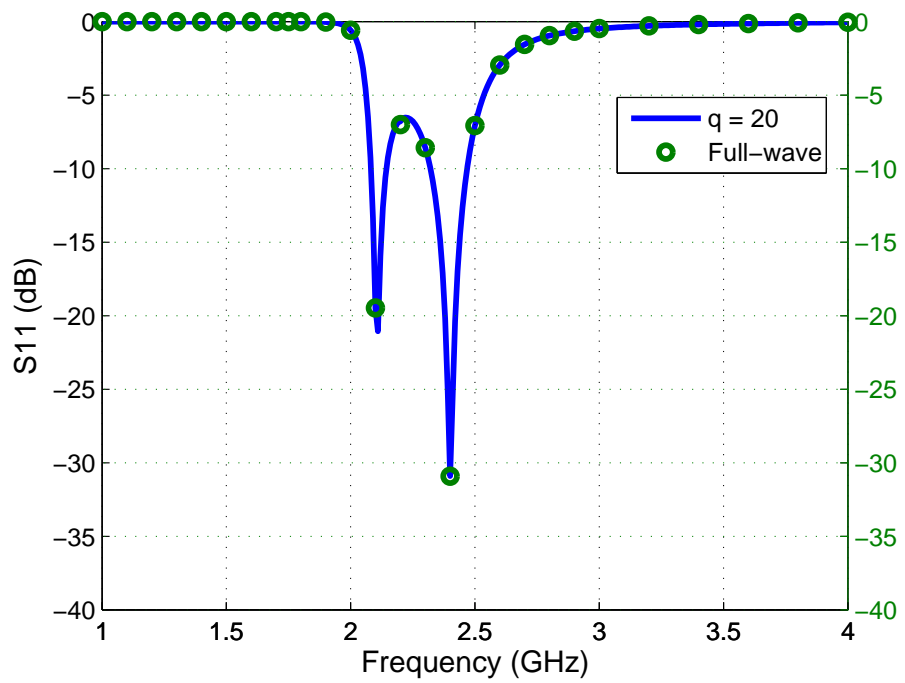
Figure 55: The return loss of the reduced model of order 20 compared to the original full-wave simulation of the band-pass filter structure layout

(a)

Inductor
Capacitor
Via

4 mm

4 mm

(b)
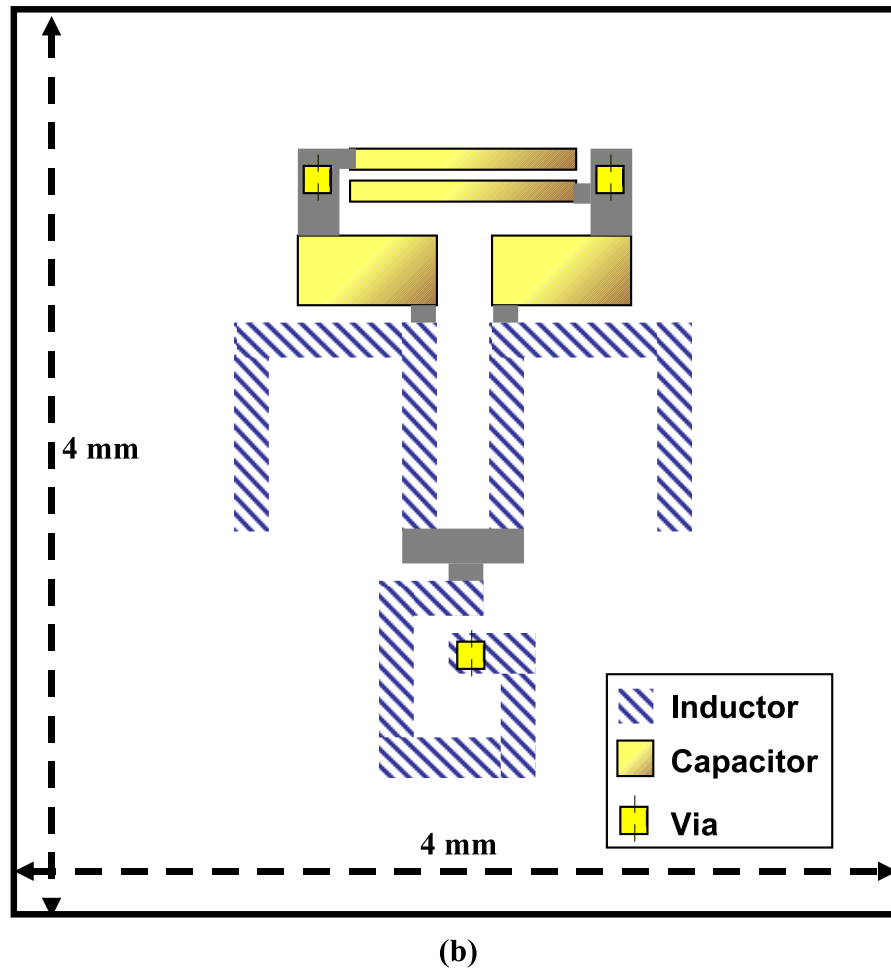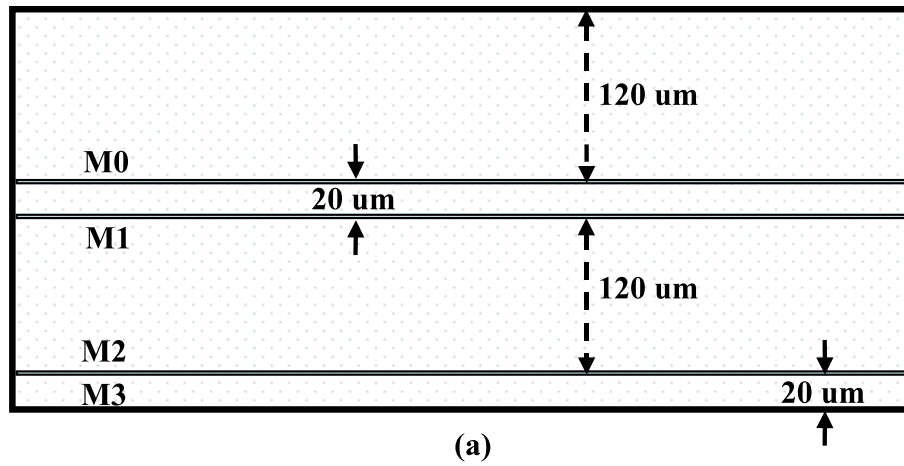
Figure 56: The (a) cross-section and (b) the top-view of the layout of the M0 layer of 5 GHz band-pass filter structure.
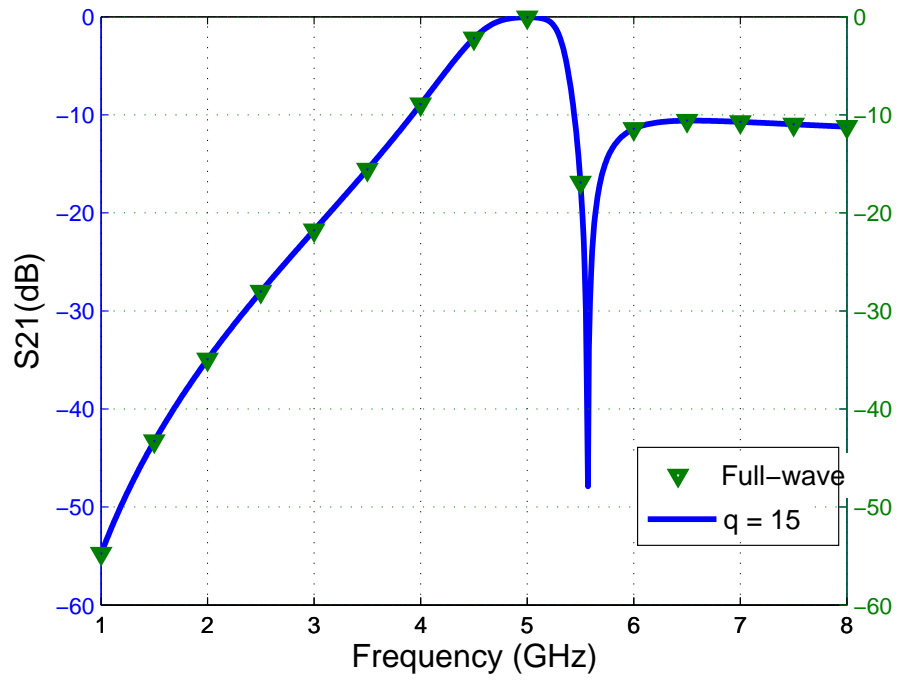
Figure 57: The insertion loss of the reduced model of order 20 compared to the original full-wave simulation of the 5 GHz band-pass filter structure layout.
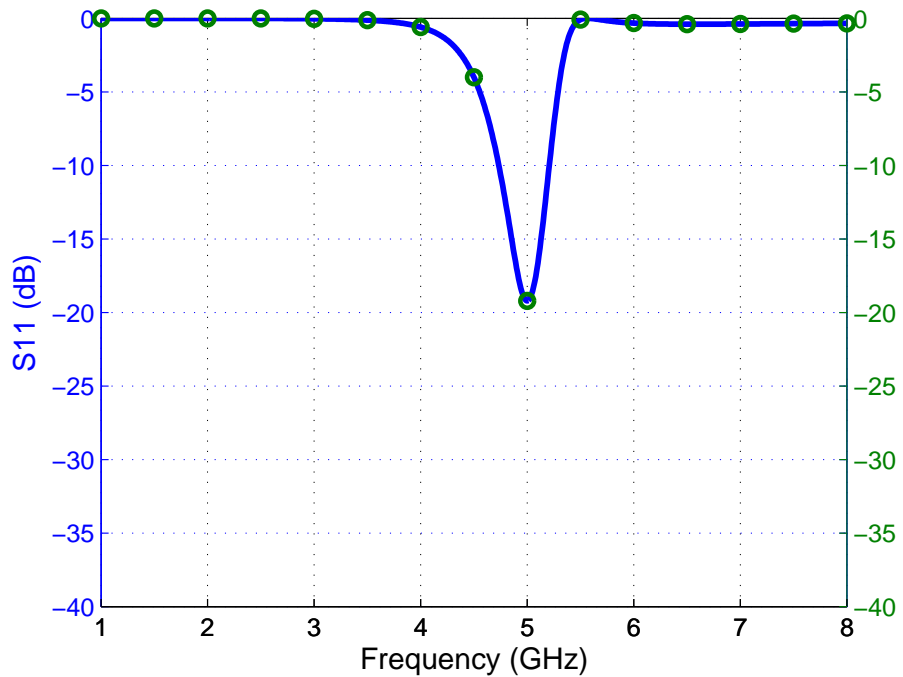
Figure 58: The return loss of the reduced model of order 20 compared to the original full-wave simulation of the 5 GHz band-pass filter structure layout.

MULTI-POINT EFFICIENT NODAL ORDER REDUCTION

5.1 Introduction

In the previous chapter, the focus was to apply an existing MOR method to the SEEC model. In this chapter, the focus is to improve on the MOR approach itself. To motivate this discussion, consider the concept of approximation achieved by expanding around a single frequency point, as shown in Fig. 59.

Increasing order of reduced model
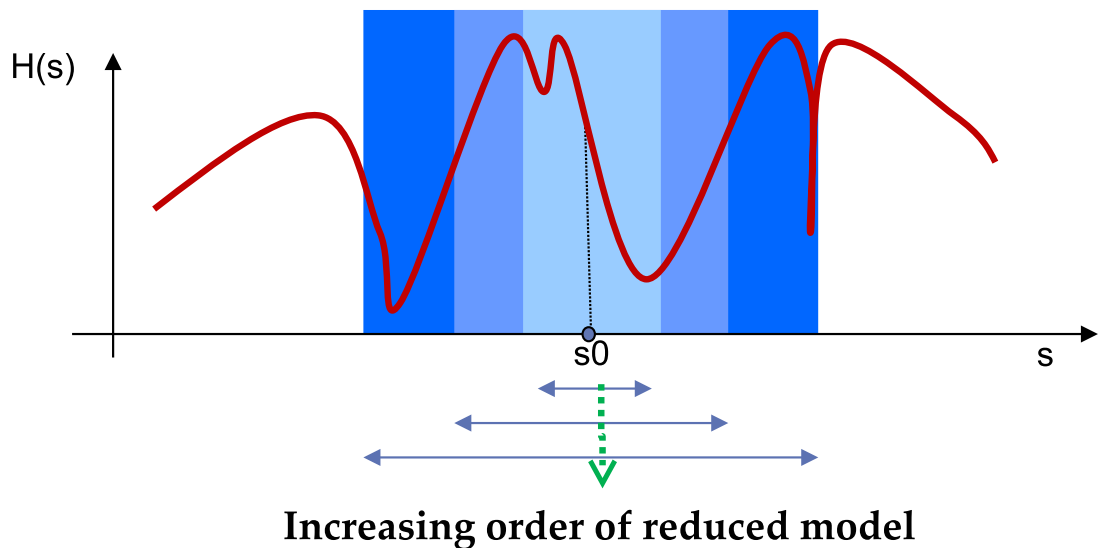
Figure 59: The single point expansion based model order reduction.

It works by increasing the accuracy of approximation as the order of the reduced model is increased. However, to achieve satisfactory levels of accuracy at points further away from the point of expansion, a much larger increase is needed in the order of the reduced model. Instead, if multiple points of expansion are used, as shown in Fig. 60, the same level of accuracy can be achieved over the entire bandwidth with
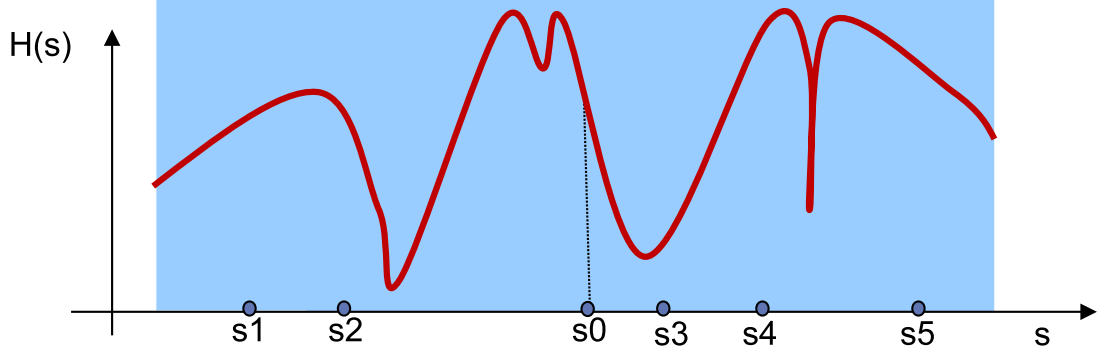
Figure 60: The multiple point expansion based model order reduction.

a much smaller reduced model. In the following sections, the multi-point expansion scheme will be developed further, demonstrating its superiority over the algorithm presented in the previous chapter.

5.2 Multi-point Efficient Nodal Order Reduction (MPENOR) Scheme

In this section, the multi-point extension scheme to a second order model order reduction method is presented. We start with the set of expansion points ϕ_0, ϕ_1, ..., ϕ_q. This set, in turn, can contain repeated instances of a given set of expansion points s_0, s_1, ..., s_r. The objective then is to find the reduced-state such that the impedance matrices of the original and reduced state satisfy the relation [30]

$$\frac{\partial^{k-1}}{\partial s^{k-1}}\mathbf{Z}(s_l) = \frac{\partial^{k-1}}{\partial s^{k-1}}\tilde{\mathbf{Z}}(s_l),\qquad(54)$$

$$1 \leq k \leq \nu_l, \quad 1 \leq l \leq r,$$

where ν_l corresponds to the reduced order at a given local subspace $\mathcal{K}_{s_l}$. This ensures that through multiple local expansions, a more global approximation for the original system is obtained. The main algorithm for this is described in Fig. 61. It works by generating the union of the Krylov subspaces $\mathcal{K}_{s_0}$, $\mathcal{K}_{s_1}$, ..., $\mathcal{K}_{s_r}$ corresponding to the points of expansion. The recurrence relation given by (39) is maintained here, with the summation limited to two terms. The inner iteration loop ensures the

proper generation of orthogonal basis vectors. The check for equality of successive ϕ_i values establishes the transition from one expansion point s_l, to the next. This directly corresponds to the transition from generating the Krylov subspace $\mathcal{K}_{s_l}$, to the subspace $\mathcal{K}_{s_{lmax}}$. Also, as previously with the single point algorithm, convergence is determined through a predefined tolerance level and on-the-fly deflation is done during the orthogonalization process. When a single point of expansion is chosen, the algorithm becomes the same as in the improved efficient nodal order reduction approach. In addition to a predetermined tolerance at a given point, in the case of multi-point reduction, a maximum order of expansion, ν_l, may be set for each local Krylov subspace. The choice of subsequent expansion points can be done by looking at two factors: 1) determining the values of frequencies where the minimum deviation is observed in successive iterations and 2) the frequencies at which the maximum relative error is observed. This process can be repeated if necessary. Thus an accurate control over the relative error is achieved in the entire frequency bandwidth of interest. The relative error is given as

$$\epsilon_{rel}(s) = \frac{|S_{Full-wave}(s) - S_{Model}(s)|}{|S_{Full-wave}(s)|}. \tag{55}$$

The tolerance, δ_{tol}, is measured in terms of the relative change in the frequency response between two successive iterations, similar to (67). A representative algorithm to check for a transition from one Krylov subspace to the next, and to check for the global convergence of the solution is shown in Fig. 62. For each of the distinct expansion point s_l, one can choose a minimum number of expansion order after which a check for transition to another subspace is performed. This is shown in the algorithm with the set of values ζ_0, ζ_1, ..., ζ_r. The set of points over which the tolerance is checked is φ_0, φ_1, ..., φ_n, with n usually being much greater than r. In addition, acceptable values for the relative error and tolerance are defined as $defErr$ and $defTol$, respectively.

The reduced state equation obtained through the multi-point efficient nodal order

Input: G, C, Γ, B, I, s_0, s_1, …, s_r
Output: $\tilde{\mathbf{G}}_{MP}$, $\tilde{\mathbf{C}}_{MP}$, $\tilde{\Gamma}_{MP}$, $\tilde{\mathbf{B}}_{MP}$, $\tilde{\mathbf{I}}_{MP}$

Require: $q > 0$
Ensure: $size(\mathbf{C}) = size(\Gamma)$, $rows(\mathbf{C}) = rows(\mathbf{B})$,
  $cols(\mathbf{B}) = rows(\mathbf{I})$
  if G $\neq 0$ **then**
    Ensure: $size(\mathbf{G}) = size(\mathbf{C})$
  end if
  $convFlag = 0$
  $l = 0$
  $iterCount = 0$
  $\phi_0 = s_0$
  Solve: $(\mathbf{G} + \phi_0 \mathbf{C} + \Gamma/\phi_0)\, \mathbf{U}_0 = \mathbf{BI}$
  $\mathbf{W}_0 = orth(\mathbf{U}_0)$
  $\mathbf{U}_{-1} = 0$
  $k = 1$
  $\phi_k = s_0$
  while $k \leq q$ **do**
    if $\phi_k \neq \phi_{k-1}$ **then**
      Solve: $(\mathbf{G} + \phi_k \mathbf{C} + \Gamma/\phi_k)\, \mathbf{U}_k = \mathbf{BI}$
      $\mathbf{W} = [\mathbf{W}\ \mathbf{U}_k]$
      $\mathbf{W} = orth(\mathbf{W})$
      $\mathbf{U}_{k-1} = 0$
      $\phi_{k+1} = s_l$
      $k = k + 1$
    end if
    $iterCount = iterCount + 1$
    $\mathbf{T} = \mathbf{C}\phi_k\mathbf{U}_{k-1} - (\Gamma/\phi_k)(\mathbf{U}_{k-1} + \mathbf{U}_{k-2})$
    Solve: $(\mathbf{G} + \phi_k \mathbf{C} + \Gamma/\phi_k)\, \mathbf{U}_k = \mathbf{T}$
    $\mathbf{W} = [\mathbf{W}\ \mathbf{U}_k]$
    $\mathbf{W} = orth(\mathbf{W})$
    $\tilde{\mathbf{G}}_{MP} = \mathbf{W}^T\mathbf{G}\mathbf{W}$, $\tilde{\mathbf{C}}_{MP} = \mathbf{W}^T\mathbf{C}\mathbf{W}$,
    $\tilde{\Gamma}_{MP} = \mathbf{W}^T\Gamma\mathbf{W}$, $\tilde{\mathbf{B}}_{MP} = \mathbf{W}^T\mathbf{B}$, $\tilde{\mathbf{I}}_{MP} = \mathbf{IW}$
    checkConvergence (See Fig. 4)
    if $convFlag = 1$ **then**
      Break
    end if
    $k = k + 1$
  end while

Figure 61: Pseudocode for the multi-point efficient nodal order reduction algorithm.

```
Input:  φ₀, φ₁, …, φₙ, ζ₀, ζ₁, …, ζᵣ, defTol,
defErr

    errMax = max [ε_rel(s₀), ε_rel(s₁), …, ε_rel(sᵣ)]
    Find lmax such that ε_rel(s_lmax) = errMax
    tolMax = max [δ_tol(φ₀), δ_tol(φ₁), …, δ_tol(φₙ)]
    if errMax < defErr and tolMax < defTol then
        convFlag = 1
    else
        if iterCount ≥ ζₗ and ε_rel(φₖ) < defErr then
            if ε_rel(s_lmax) > defErr and δ_tol(φ_lmax) >
            defTol then
                φₖ₊₁ = s_lmax
                iterCount = 0
                l = lmax
            end if
        else
            φₖ₊₁ = sₗ
        end if
    end if
```

Figure 62: Pseudocode for the "checkConvergence" algorithm used in Fig. 61.

reduction scheme is then given as

$$\left(\tilde{\mathbf{G}}_{MP} + s\tilde{\mathbf{C}}_{MP} + \frac{\tilde{\Gamma}_{MP}}{s} \right) \tilde{\mathbf{V}} = \tilde{\mathbf{B}}_{MP}\tilde{\mathbf{I}}_{MP}, \tag{56}$$

$$\tilde{\mathbf{G}}_{MP} = \mathbf{W}^T\mathbf{G}\mathbf{W}, \ \tilde{\mathbf{C}}_{MP} = \mathbf{W}^T\mathbf{C}\mathbf{W}, \ \tilde{\Gamma}_{MP} = \mathbf{W}^T\Gamma\mathbf{W}, \tag{57}$$

$$\tilde{\mathbf{B}}_{MP} = \mathbf{W}^T\mathbf{B}, \ \tilde{\mathbf{I}}_{MP} = \mathbf{I}\mathbf{W}. \tag{58}$$

5.2.1   Passivity and Reciprocity

The proof for passivity follows the pattern described in the previous chapter.

5.2.2   Moment Matching Property

The transfer function of the second order system in (22) can be written as

$$\mathbf{H}(s) = \mathbf{B}^T \left(\mathbf{G} + \mathbf{C}s + \frac{\Gamma}{s} \right)^{-1} \mathbf{B}, \tag{59}$$

65

which in turn can be rewritten in first order form as

$$\mathbf{H}(s) = \mathbf{B}_a^T \left(\boldsymbol{\mathcal{G}} + s\boldsymbol{\mathcal{C}}\right)^{-1} \mathbf{B}_a, \tag{60}$$

where,

$$\boldsymbol{\mathcal{G}} = \begin{bmatrix} \mathbf{G}_\sigma & \mathbf{D}_h \\ \mathbf{D}_e & \mathbf{0} \end{bmatrix}, \tag{61}$$

,

$$\boldsymbol{\mathcal{C}} = \begin{bmatrix} \mathbf{C}_\epsilon & \mathbf{0} \\ \mathbf{0} & \mathbf{L}_\mu \end{bmatrix}, \tag{62}$$

and,

$$\mathbf{B}_a = \begin{bmatrix} \mathbf{B} \\ \mathbf{0} \end{bmatrix}. \tag{63}$$

The matrices in right hand side of (61) and (62) take the same meaning as in (9). Similarly, for the reduced system in (56), The transfer function is of the form

$$\mathbf{H}_q(s) = \tilde{\mathbf{B}}_a^T \left(\tilde{\boldsymbol{\mathcal{G}}} + s\tilde{\boldsymbol{\mathcal{C}}}\right)^{-1} \tilde{\mathbf{B}}_a, \tag{64}$$

where, the matrices $\tilde{\boldsymbol{\mathcal{G}}}$, $\tilde{\boldsymbol{\mathcal{C}}}$, and $\tilde{\mathbf{B}}_a$ take the reduced order definitions corresponding to the matrices defined in (61), (62) and (63), respectively. In the form given by (60) and (64), [48] already presents us with proof that moment matching property is maintained with any one-sided projection transformation. The interested reader is referred to [3], where a mathematically rigorous treatment for moment matching by second order reductions is presented by using the same logic as above - converting the second order transfer function to a first order form and then proceeding to show the moment matching property. In the case of multipoint reduction, the projection matrix can be written in terms of individual Krylov subspaces at given expansion points $s_0, s_1, ..., s_r$ as

$$\mathbf{W} = [\mathbf{Q}_0 \ \mathbf{Q}_1 \ \ldots \ \mathbf{Q}_r]. \tag{65}$$

This is equivalent to matching moments at each of the expansion points as stated in (54) as long as it is ensured that [24] [30]:

1. The projection matrix $\mathbf{W}$ is full rank, due to its orthonormal generation, and

2. The union of Krylov subspaces generated through the multi-point expansion scheme satisfies the relation

$$\bigcup_{l=0}^{m} \mathcal{K}_{s_l} \; \subseteq \; span\left\{\mathbf{W}\right\}. \tag{66}$$

5.3 Numerical Test Case

In this section the limitation of model order reduction by expanding at only one frequency point is shown by means of a numerical example, thus motivating the need for multi-point efficient nodal order reduction algorithm, and show its application.

5.3.0.1 Test Structure - Electromagnetic Band-gap Structure

The example considered is that of an electromagnetic bandgap (EBG) structure, which have been used to provide electrical isolation in RF/microwave structures, reducing the adverse effect of noise. The structure under consideration is shown in Fig. 63. Each metal patch has a dimension of $14 \; mm \times 14 \; mm$ and the metal branch size is $1 \; mm \times 1 \; mm$. The structure is enclosed in a PEC box and is discretized using a unit cell of dimensions $0.5 \; mm \times 0.5 \; mm \times 10 \; \mu m$, resulting in approximately $42\,000$ unknowns. The perfect electric conductor box is filled with a homogeneous medium with dielectric constant $\epsilon_r = 4.5$. The SEEC model is extracted from this layout and model reduction with single point expansion is applied to it. The response of the reduced order model with a single point of expansion is shown in Fig. 64. It is seen that though at lower frequencies the response matches well with that of the full-wave solution at the test-points, at higher frequency there is a considerable deviation. To quantify this deviation the relative error of the model, defined as

$$Relative \; Error = \frac{\left|S_{Full-wave} - S_{Model}\right|}{\left|S_{Full-wave}\right|}, \tag{67}$$

is considered.
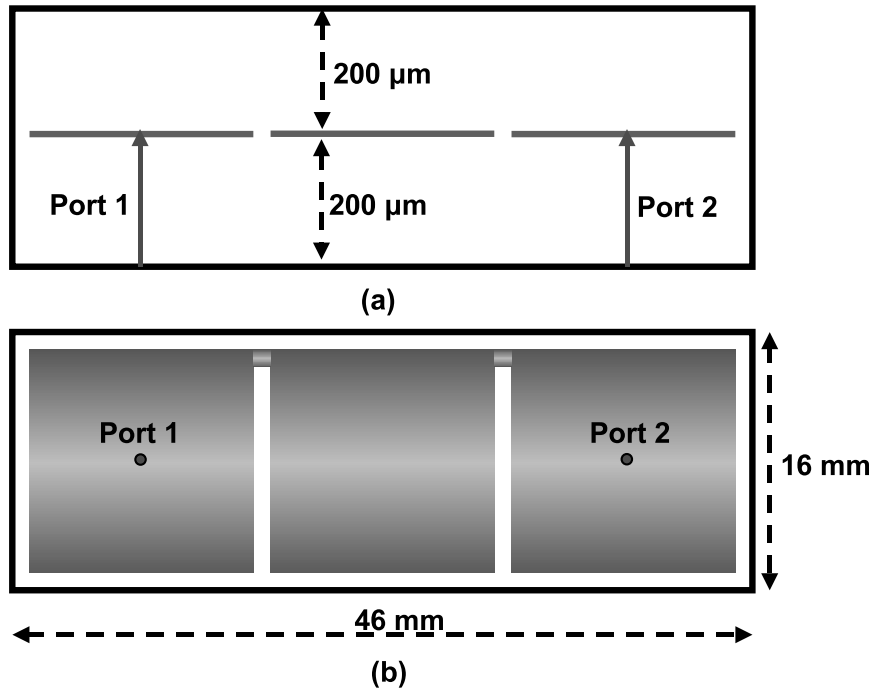
**Figure 63:** The (a) cross-section and (b) top-view of the layout of the EBG structure
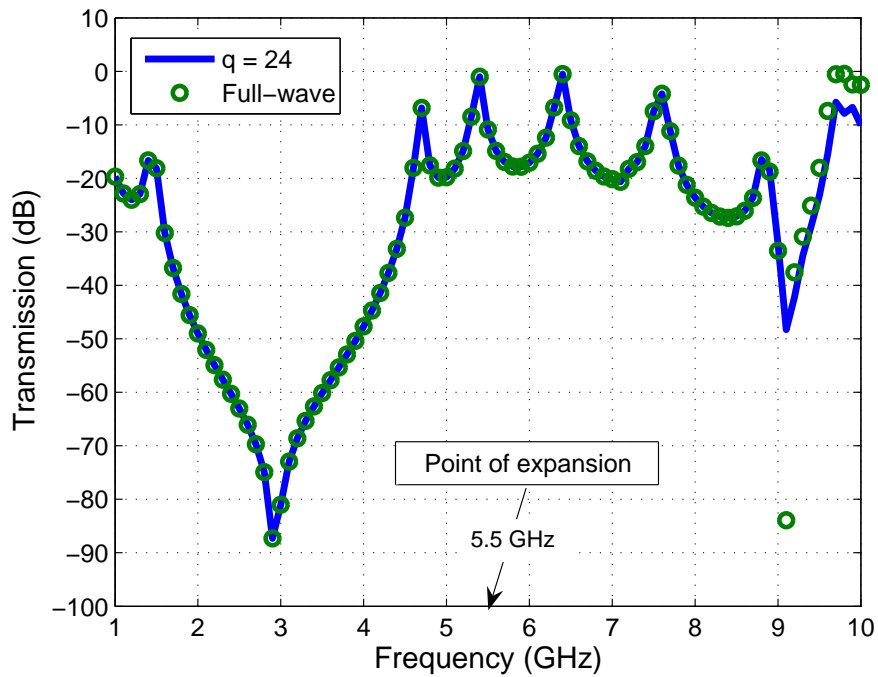
Figure 64: The response of the reduced model of order 24 compared to the original full-wave simulation of the EBG structure layout

68

The semilogarithmic plot of relative error in the magnitude of insertion loss as a function of frequency is shown in Fig. 65. Here we can clearly see the local nature of the Krylov subspace reduction process, wherein the relative error is least in the vicinity of the point of expansion. As we increase the model order from $q = 8$ to $q = 16$, the reduction in relative error is again localized near the point of expansion. Increasing the reduced order to 24 results in a much better representation at the beginning of the frequency range. However, near the upper limits of the bandwidth, we see that a considerable amount of error remains. Specifically, above 8.5 GHz, the relative error is more than 10^{-1} even for the case of $q = 24$, which is clearly seen in the deviation from the full-wave simulation in Fig. 64. This is further corroborated by the stem plot of the convergence behavior as the order of the reduced model is increased as shown in Fig. 66. The tolerance is measured in terms of the relative change in the frequency response between two successive iterations, similar to (67). At 10 GHz the tolerance value is still large for q = 24, whereas at 7 GHz, acceptable convergence has been obtained much earlier.

Keeping the large deviation at the lower and upper limits of the frequency bandwidth, the MPENOR algorithm with the imaginary points of expansion s_0, s_1 and s_2 corresponding to the frequencies 2.5 GHz, 5.5 GHz and 9 GHz and $\nu = \{6, 8, 14\}$ is applied, resulting in a three-point MPENOR algorithm of reduced order, $q = 28$. First we look at the convergence behavior in terms of the stem plot shown in Fig. 67. By the time the expansion order at 9 GHz reaches 13, we observe acceptable tolerance at 10 GHz. Fig. 68 shows the actual insertion loss response of the three-point MPENOR reduced model as compared to the full-wave solution of the EBG structure at test points. Fig. 69 shows the comparison of the return loss for the original and the three-point reduced model obtained through multi-point efficient nodal order reduction. The application of the MPENOR algorithm results in an accurate match at reduced computational cost.
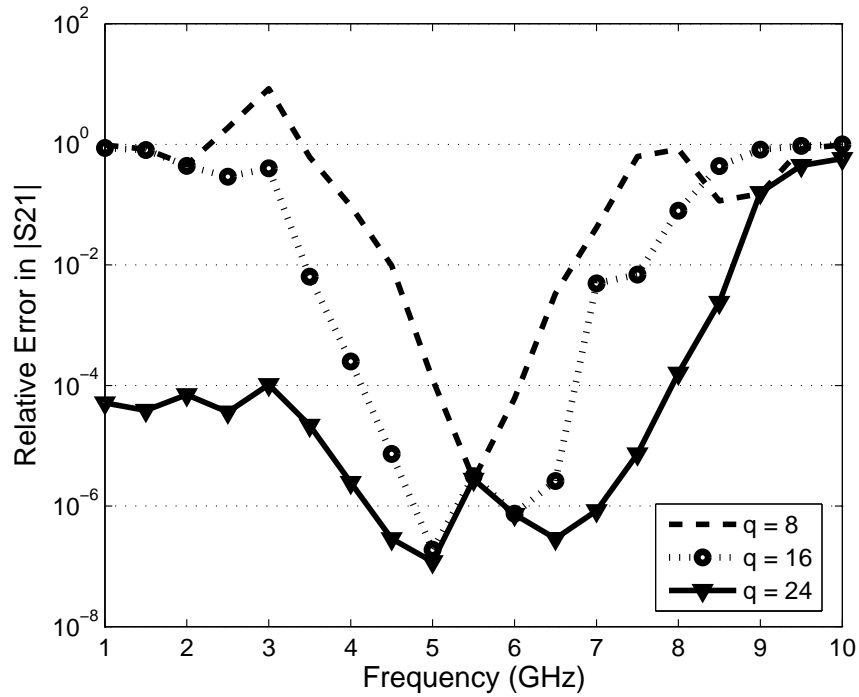
Figure 65: The semilogarithmic plot of relative error with respect to frequency for orders of reduction 8, 16 and 24.
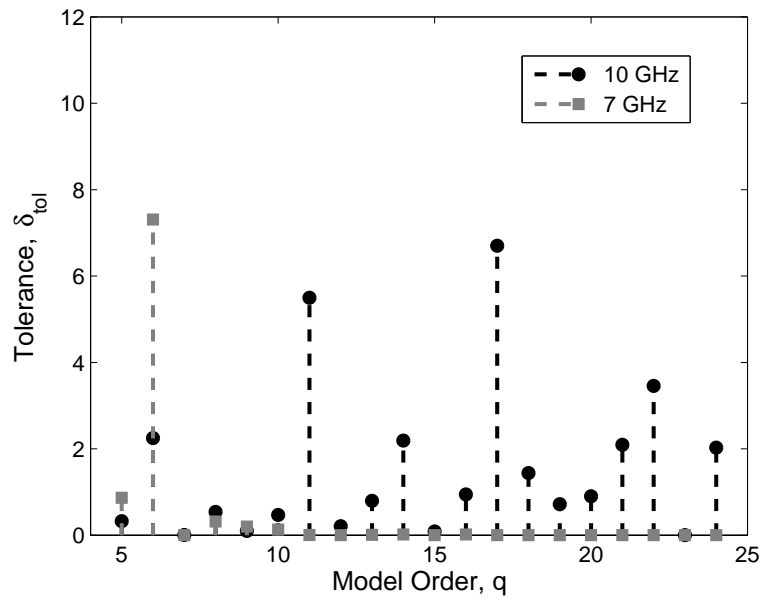
Figure 66: The tolerance values as the model order is increased for single point expansion at 5.5 GHz.

The relative error values of this model are compared to that of the reduced model with single point of expansion, with varying orders. This is shown in Fig. 70. Clearly
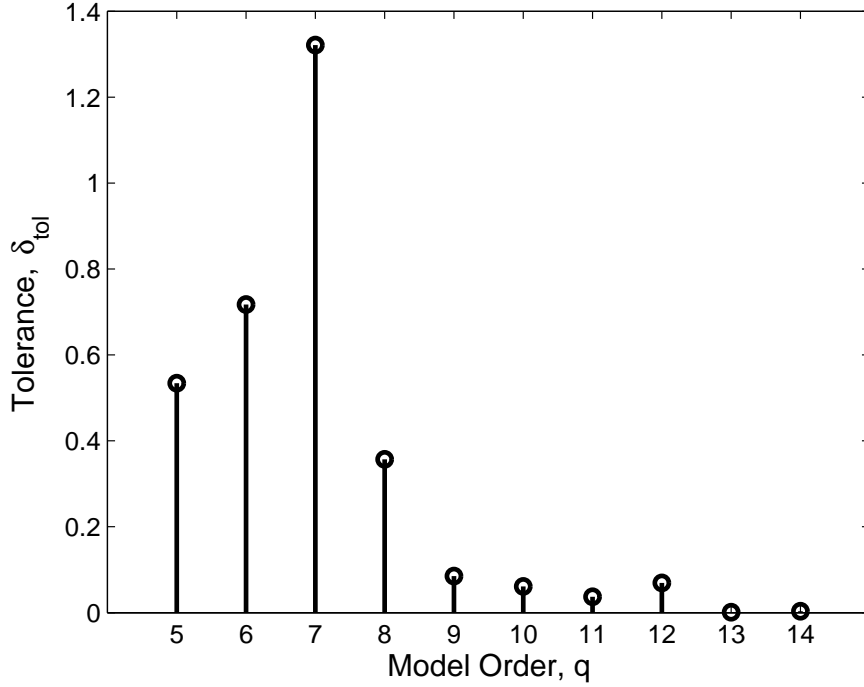
Figure 67: The tolerance values as the model order at 9 GHz is increased for the 3 point multi-point efficient nodal order reduction algorithm.

see that the multi-point scheme results in a more accurate representation over the entire bandwidth. In contrast, even with the reduced order increasing to $q = 32$, the relative error is still greater than 10^{-1} at 10 GHz. To achieve nearly the same level of accuracy as the three-point MPENOR algorithm at the upper bounds of frequency bandwidth, the reduced order for the single point expansion scheme has to be increased to $q = 40$. The computational saving of the MPENOR algorithm is thus clearly in terms of reducing the number of linear equations to be solved during the recursive calculation of the projection matrix. In quantitative terms, the time taken for model generation and the full frequency sweep from 1 GHz to 10 GHz with a step of 0.01 GHz is shown in Table 3. All simulations were carried out on a personal computer with a Intel Core 2 Duo E4500 processor and 2 gigabytes of memory.
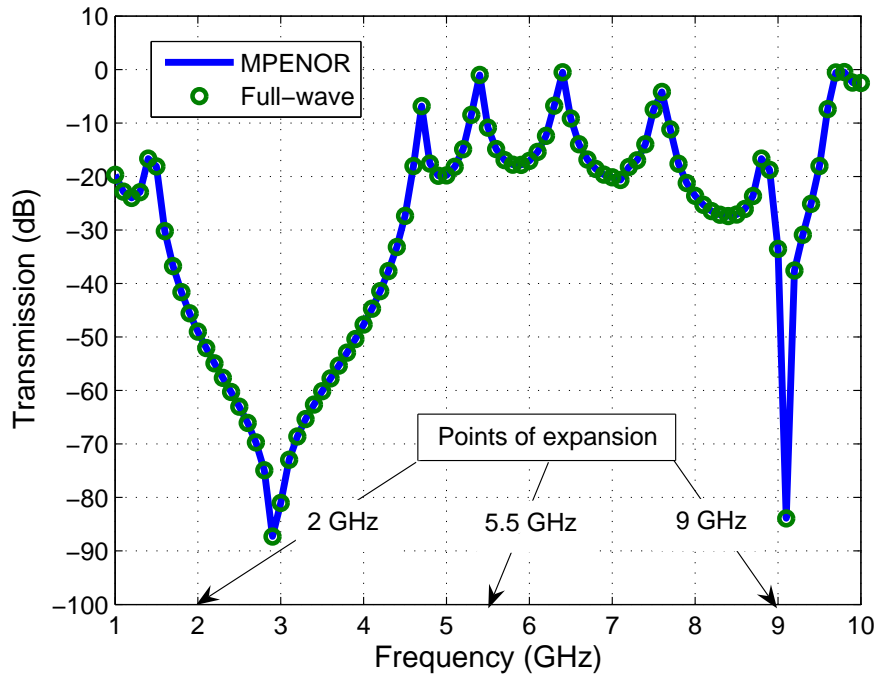
Figure 68: The comparison of the insertion loss response of the 3-point reduced model of order 28 compared to the original full-wave simulation of the electromagnetic bandgap structure layout

Table 3: The performance of algorithms in terms of time.

Algorithm	Model Generation	Frequency Sweep
Full-wave	5 sec.	22.5 hrs.
q=40	1 hr. 49 min.	2 sec.
MPENOR(q=28)	1 hr. 14 min.	2 sec.

5.4   Summary

The 3D full-wave analysis is a computationally intensive process, and in this work an attempt has been made to solve the problem in a fast, memory efficient manner. The MOR of SEEC model extracted from discretized form of Maxwell's equation has been shown to be a computationally efficient process enabling fast frequency sweep of complex RF/microwave structures. In addition to the savings in computational time and memory by operating on a second order system instead of a linear system,
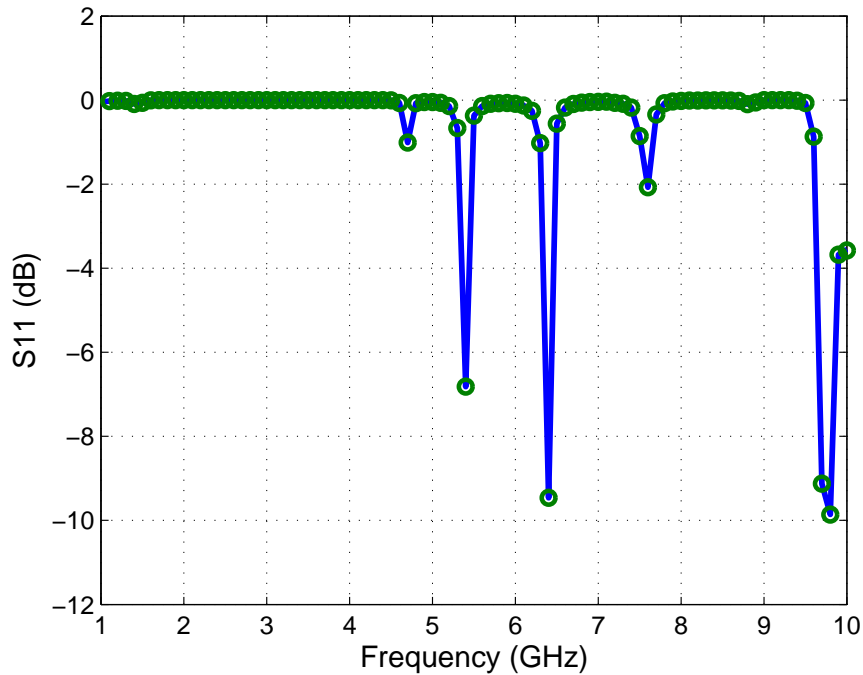
Figure 69: The comparison of the return loss response of the 3-point reduced model of order 28 compared to the original full-wave simulation of the electromagnetic bandgap structure layout

it is noted that the MPENOR algorithm gives rise to a passive and reciprocal system without the need for additional passivity enforcement algorithms. Further, the calculation of the projection matrix stabilized by the use of a complex-space shifted diagonal preconditioner enables the solution of problems without the need for additional storage of the factorized matrix. It is to be noted, however, that in case of smaller problems, such a factorization may be computationally advantageous.

The advantage of the MPENOR algorithm over the single point expansion scheme has been clearly demonstrated in terms of reduced computational cost. This becomes particularly useful when the system response is fairly complex. Though the single point scheme can also reach the same levels of accuracy, the reduced order may be significantly more. This ties in to the localized nature of Krylov subspace projection process. Increasing the order of the reduced model in turn means that more moments of the transfer function of the reduced system are matched to the moments of transfer

73
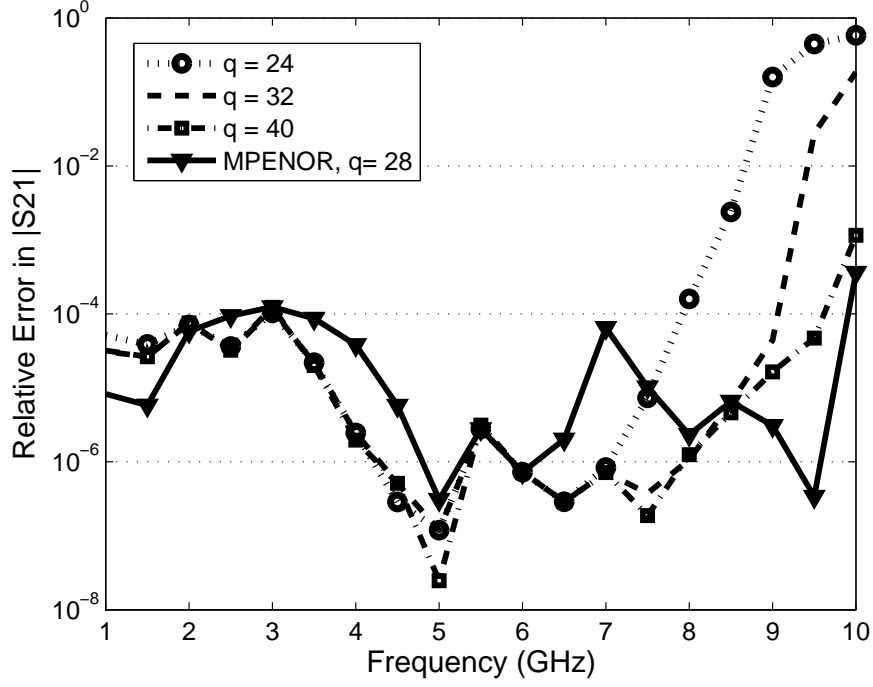
Figure 70: The semilogarithmic plot of relative error with respect to frequency for imp-ENOR algorithm with orders of reduction 24, 32 and 40 compared to that of MPENOR algorithm of order 28.

function of the original system. With increasingly more moments matched, the contribution of states not necessarily dominant at the given expansion point can be taken into account, thus providing better accuracy over a wider frequency bandwidth. In contrast, by creating a union of Krylov subspaces at multiple points in the MPENOR algorithm, the projection matrix thus formed is more globally representative and can swiftly account for various dominant states in the response of the SEEC model. However, for extremely large systems, the generation of a large projection matrix with linearly independent vectors may become the limiting factor. In such cases, one may be left with options of (a) multiple multi-point expansions, (b) multiple single-point expansions, or (c) iterative solution at each discrete frequency point. Among the limitations of the process are the fact that at extremely low frequencies the reduced model is no longer accurate. This happens due to the fact that

$$\lim_{s \to 0} \left(\frac{\Gamma}{s} \right) = undefined. \tag{68}$$

But keeping in mind that quasi-static lumped element models can be easily obtained at considerably less computational cost due to various approximations that can be made to the Maxwell's equation, the proposed MPENOR algorithm remains an extremely efficient option for fast frequency sweep at higher frequencies where these approximations may no longer be valid. An added advantage of the multi-point approach is that it enables the use of parallel processing, resulting in reduced computational time.

CHAPTER VI

BILINEAR CONFORMAL TRANSFORMATION BASED REDUCED ORDER MODELING

6.1 Introduction

The MOR methods explored so far rely primarily on approximating the transfer function of the linear system in the frequency domain, without any error bounds. An *error bound second order model reduction* scheme is formulated in this section through bilinear conformal transformation (BCT).

6.2 Bilinear Conformal Mapping and Error Bound

The bilinear transformation is defined to be a conformal mapping such that the Laplace domain variable,

$$s = c\frac{1 - z^{-1}}{1 + z^{-1}}, \tag{69}$$

c being the constant of transformation. The bilinear transform maps the imaginary axes in the Laplace domain to the unit circle in z-domain. The left half of the Laplace domain is mapped to the interior of the unit circle, and the exterior of the unit circle corresponds to the right half of the Laplace domain. This is shown in Fig. 71.

The BCT was first demonstrated for the first order MOR of a linear system in [10]. If $X(s)$ is a given transfer function reduced to $\tilde{X}(s)$, the error bound is given as [10]:

$$|\epsilon(t)|^2 \leq \frac{2^{(}2N - 3)\pi^2\Gamma(N - \frac{3}{2})}{3\Gamma(N - 1)} \int_{-\pi}^{\pi} \left| X(e^{j\theta}) - \tilde{X}(e^{j\theta}) \right|^2 d\theta, \tag{70}$$

where, $\epsilon(t)$ is the time domain error between the original and the reduced system transfer functions, N is the number of zeros of $X'(z)$ when $z = -1$.
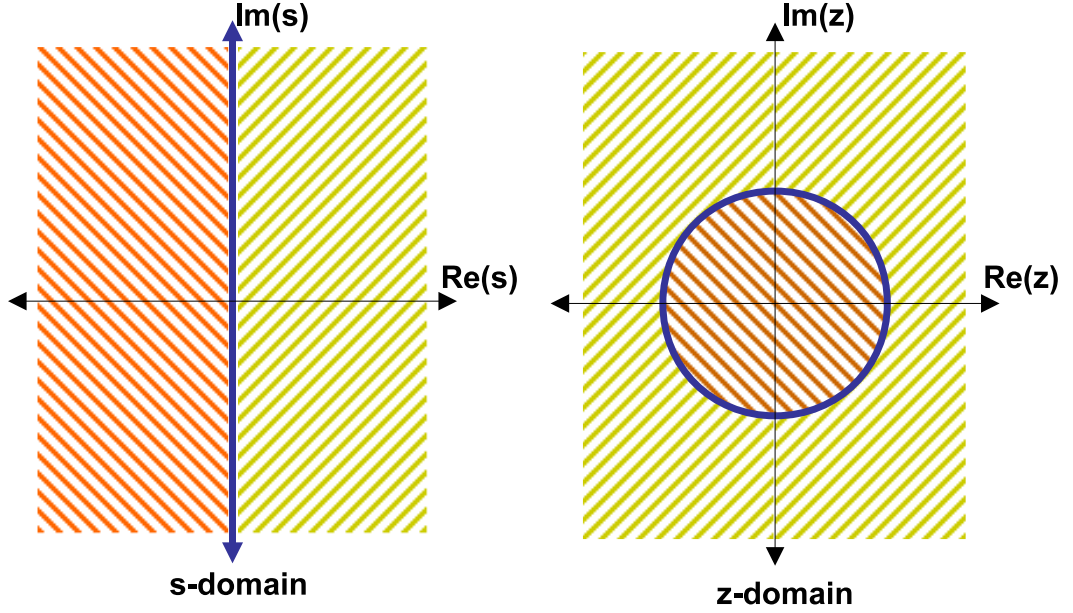
Figure 71: The mapping obtained from bilinear conformal transformation

6.3 Nodal Order Reduction via Bilinear Conformal Transformation (NORBCT) Algorithm

In this section the model order reduction scheme for second order systems through bilinear transformation is introduced. By using the bilinear transformation (82) in the SEEC nodal equations (22), we get the nodal equations in the z-domain as

$$\left(\mathbf{G} + c\frac{1 - z^{-1}}{1 + z^{-1}}\mathbf{C} + \frac{(1 + z^{-1})\Gamma}{c(1 - z^{-1})}\right)\mathbf{V}(z) = \mathbf{B}\mathbf{U}(z) \qquad (71)$$

Following a few steps of mathematical manipulation and expanding $\mathbf{V}(z)$ and $\mathbf{U}(z)$ in powers of z, it is possible to show that a recursive relation can be obtained for the various $\mathbf{V}_k(z)$. These vectors correspond to the voltage moments of the transfer function of the second order system in the z-domain. The vectors thus calculated can be used to form a projection matrix, $\mathbf{Q} \in \mathbb{C}^{N \times q}$, which in turn can be used to reduce (22) through congruent transformation resulting in:

$$\left(\tilde{\mathbf{G}} + \tilde{\mathbf{C}}s + \frac{\tilde{\Gamma}}{s}\right)\tilde{\mathbf{V}} = \tilde{\mathbf{B}}\tilde{\mathbf{U}} \qquad (72)$$

77

$$\begin{array}{l}
\textbf{Solve: } (\mathbf{G} + c\mathbf{C} + \Gamma/c)\,\mathbf{V}_0 = \mathbf{BU} \\
\mathbf{V}_0 = orth(\mathbf{V}_0) \\
\textbf{Solve: } (\mathbf{G} + c\mathbf{C} + \Gamma/c)\,\mathbf{V}_1 = 2\,(c\mathbf{C} - \Gamma/c)\,\mathbf{V}_0 \\
\text{Orthonormalize } \mathbf{V}_1 \text{ against } \mathbf{V}_0, \mathbf{V}_1 \\
T = 2\,(c\mathbf{C} - \Gamma/c)\,\mathbf{V}_1 + (\mathbf{G} - c\mathbf{C} - \Gamma/c)\,\mathbf{V}_0 - \mathbf{BU} \\
\textbf{Solve: } (\mathbf{G} + c\mathbf{C} + \Gamma/c)\,\mathbf{V}_2 = T \\
\text{Orthonormalize } \mathbf{V}_2 \text{ against } \mathbf{V}_0, \mathbf{V}_1, \mathbf{V}_2 \\
k = 3 \\
\textbf{while } k \leq q \textbf{ do} \\
\quad T = 2\,(c\mathbf{C} - \Gamma/c)\,\mathbf{V}_{k-1} + (\mathbf{G} - c\mathbf{C} - \Gamma/c)\,\mathbf{V}_{k-2} \\
\quad \textbf{Solve: } (\mathbf{G} + c\mathbf{C} + \Gamma/c)\,\mathbf{V}_k = T \\
\quad \text{Orthonormalize } \mathbf{V}_k \text{ against } \mathbf{V}_0, \mathbf{V}_1, \ldots, \mathbf{V}_k \\
\quad k = k + 1 \\
\textbf{end while} \\
\mathbf{Q} = [\mathbf{V}_0, \mathbf{V}_1, \ldots, \mathbf{V}_q] \\
\tilde{\mathbf{G}} = \mathbf{Q}^T \mathbf{G} \mathbf{Q}, \ \tilde{\mathbf{C}} = \mathbf{Q}^T \mathbf{C} \mathbf{Q}, \\
\tilde{\Gamma} = \mathbf{Q}^T \Gamma \mathbf{Q}, \ \tilde{\mathbf{B}} = \mathbf{Q}^T \mathbf{B}, \ \tilde{\mathbf{U}} = \mathbf{U} \mathbf{Q}
\end{array}$$

Figure 72: The nodal order reduction via bilinear conformal transformation (NOR-BCT) algorithm

where,

$$\tilde{\mathbf{G}} = \mathbf{Q}^T \mathbf{G} \mathbf{Q}, \ \tilde{\mathbf{C}} = \mathbf{Q}^T \mathbf{G} \mathbf{Q}, \ \tilde{\Gamma} = \mathbf{Q}^T \Gamma \mathbf{Q}$$

$$\tilde{\mathbf{B}} = \mathbf{Q}^T \mathbf{B}, \ \tilde{\mathbf{U}} = \mathbf{U} \mathbf{Q}.$$

The process of obtaining the projection matrix is shown in Fig. 72. During the recursive calculation of the vectors, orthogonalization with on-the-fly deflation is done to ensure the generation of a full-rank projection matrix. The process can be suitably stopped once a predefined tolerance level is achieved.

6.3.1 Passivity and Reciprocity

Passivity is an important consideration for such systems and is defined to be a state where no net energy is generated by the system [56]. More rigorously it can be stated that for a system to be passive, its transfer function, H(s), must obey the following

rules:

1. $H(s)$ is analytic in s.

2. $H(s^*) = H^T(s)^*$

3. $z^*(H(s) + H^*(s))z \geq 0$, $\forall z \in \mathbb{C}$, and $\forall s \in \mathbb{C}$ with $\Re(s) > 0$

The use of congruence transformation preserves the passivity of the system [48][60]. Also, by working with the second order system, i.e. the nodal analysis framework, the reciprocity of the reduced system is preserved [60].

6.3.2 Relation to Generalized Laguerre Functions

The relationship between the bilinear conformal transformation and the generalized Laguerre functions was shown in [37]. We first start with the Laguerre polynomials defined as:

$$l_n(t) = \frac{e^t}{n!} \frac{d^n}{dt^n} (e^{-t} t^n).$$ (73)

The scaled time-domain Laguerre functions are then given as:

$$\Phi_n^\alpha(t) = \sqrt{(2\alpha)} e^{-\alpha t} l_n(2\alpha t), \quad n = 0, 1, 2 \dots$$ (74)

where, α is a positive scaling factor. The frequency domain Laguerre functions can be found by taking the Laplace transform of (74), and are given as:

$$\Phi_n^\alpha(s) = \frac{\sqrt{(2\alpha)}}{s + \alpha} \left(\frac{s - \alpha}{s + \alpha} \right)^n, \quad n = 0, 1, 2 \dots$$ (75)

The scaled Laguerre functions form an orthonormal basis, and any transfer function $H(s)$ can be expanded as:

$$H(s) = \sum_0^\infty F_n \Phi_n^\alpha(s)$$ (76)

which can be rewritten as:

$$H(s) = \sum_0^\infty F_n \left(\frac{s - \alpha}{s + \alpha} \right)^n$$ (77)

79

We also know that the passive Pade' approximant found through NORBCT inherently approximates the original transfer function given in the form :

$$H(z) = \sum \mathbf{B}_n z^n \tag{78}$$

where,

$$z = \frac{s - c}{s + c} \tag{79}$$

From (77), (80), and (79) we can determine that the NORBCT algorithm in the z-domain directly corresponds to finding a passive Laguerre approximant of the the original second order system in the Laplace domain.

6.3.3 Numerical Test Cases

We now look at results to demonstrate the use of the NORBCT projection approach to actual test cases.

6.3.3.1 Power ground structure with apertures

The first test case we consider is a four metal layer power ground plane structure. The dimensions of the structure are as shown in the Fig. 73. The metal plate size is 14 mm and the size of the aperture is 6 mm. The vertical distance between the metal plates is 20 μm. Discretizing the structure using a unit cell of 0.5 $mm \times$ 0.5 $mm \times$ 10 μm results in approximately 72, 000 unknowns. The PEC box is filled with a homogeneous material with dielectric constant 4.5. Fast frequency sweep of the power-ground structure is done from 1 GHz to 10 GHz using the NORBCT algorithm. In Fig. 74, we see response of the original system compared to reduced system obtained after applying the NORBCT algorithm. The full-wave simulation of the original system is done at discrete points for comparison.

6.3.3.2 Split power plane structure

The next example we consider is the split power plane structure shown in Fig. 75. Discretizing the structure using a unit cell of 0.5 $mm \times$ 0.5 $mm \times$ 30 μm results
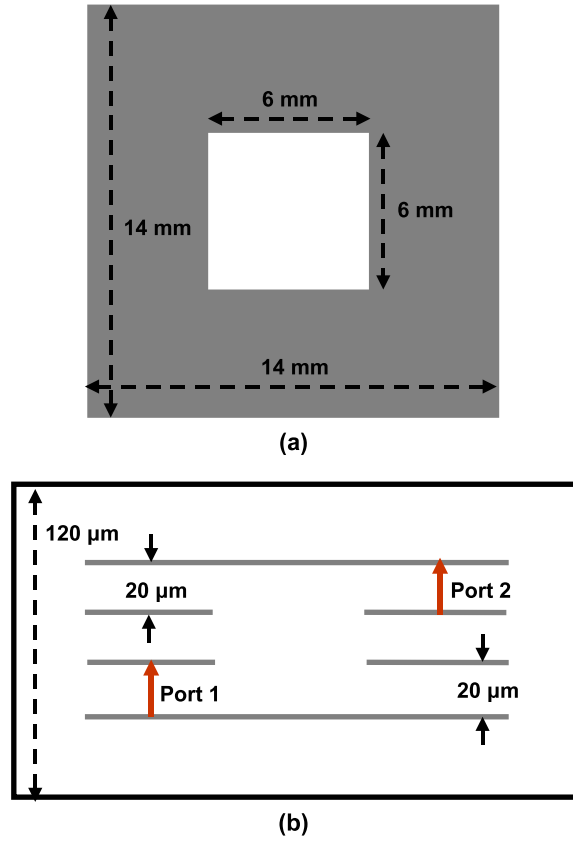
Figure 73: The (a) cross-section and (b) top-view of the layout of the power-ground structure with apertures

in approximately 100, 000 unknowns. The PEC box is filled with a homogeneous material with dielectric constant 4.4. The NORBCT algorithm is applied to obtain the fast frequency sweep of the power-ground structure. The frequency range of interest is from 1 GHz to 5 GHz. In Fig. 76, we see insertion loss of the original system compared to reduced system of order 15 obtained after applying the NORBCT algorithm. Fig. 77 shows the corresponding comparison of the return loss for the original and the reduced models. The full-wave simulation of the original system is done at discrete points for comparison.

6.3.3.3   Split Power Island

A power ground structure with a split on the top plane, as shown in Fig. 78, is considered. The structure is enclosed in a PEC box of dimensions $22mm \times 22mm \times$
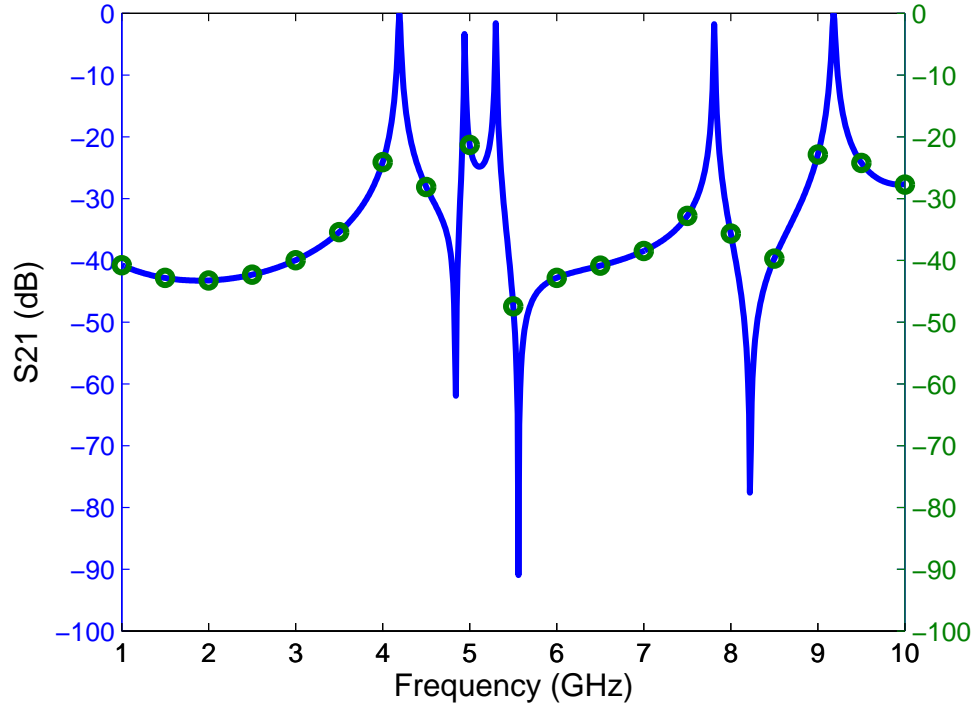
Figure 74: The response of the reduced model of order 20 (solid line) compared to the original full-wave simulation (circles) of the power-ground structure with apertures structure layout.

$80\mu m$. Discretizing the whole structure using a unit cell of dimensions $0.5mm \times 0.5mm \times 10\mu m$ results in approximately $51,000$ unknowns. The medium in the box has a dielectric constant of 3.8. The NORBCT algorithm is applied to obtain a reduced model of order 10. Fig. 79 shows a comparison between the reduced order model and the full-wave simulation. As can be seen from the plot, an accurate match is obtained over the entire frequency range under investigation, thus proving the accuracy of the algorithm to address electromagnetic simulations.

6.4 Choice of Laguerre Parameter

For a given bandwidth, BW, it is stated that the range of values over which α can be chosen is

$$4 \times BW \le \alpha \le \pi^2 \times BW. \tag{80}$$

The above inequality holds true for a system, where the frequency range of interest

82
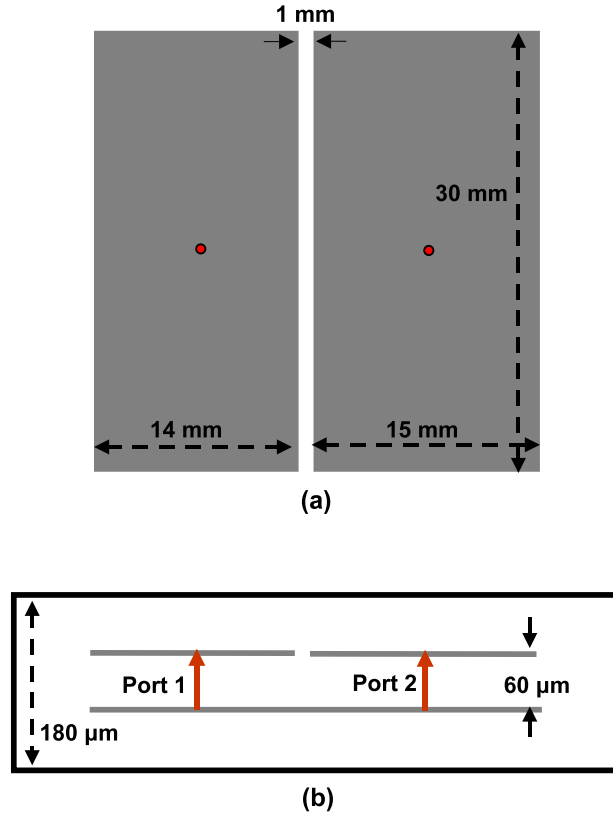
Figure 75: The (a) cross-section and (b) top-view of the layout of the split power plane structure

is $[0, f_{max}]$, and the usual choice for the Laguerre parameter is,$\alpha = BW = 2\pi f_{max}$. For a system with frequency range of interest $[f_{min}, f_{max}]$, the usual choice of the Laguerre parameter is $\pi(f_{max} + f_{min})$, which corresponds to the mid-point of the frequency range. Further, it is stated in [37] that the Laguerre parameter, α, is also related to the reciprocal of the time constant of the system. Since the time constant of a finite difference solution is related to the discretization, one can say that a Laguerre parameter based on the upper frequency bound will be better able to capture the physical dynamics of the system.

6.4.0.4 Power-island Structure

A power-ground structure with a power-island is shown in Fig. 80. The dimension of the island is $6mm \times 6mm$ and with the gap being $1mm$. The structure is enclosed in a
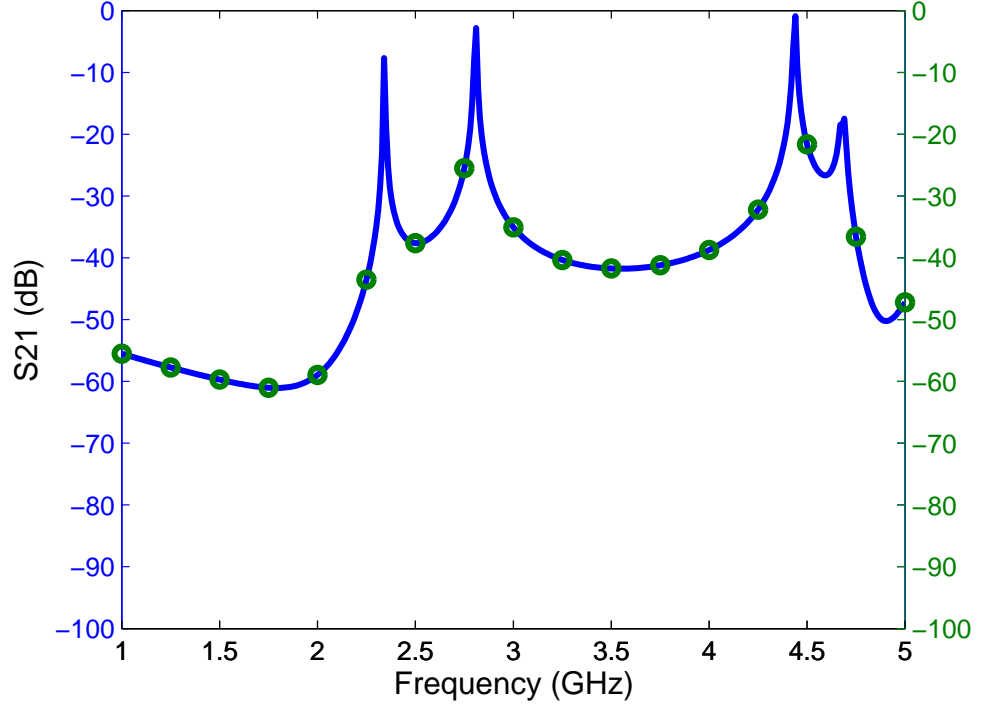
Figure 76: The insertion loss of the reduced model of order 15 (solid line) compared to the original full-wave simulation (circles) of the split power plane structure layout.

perfect electric conductor box of dimensions $26mm \times 26mm \times 400\mu m$ and discretized using a unit cell of $0.5mm \times 0.5mm \times 50\mu m$. To characterize the structure for a range up to 5 GHz, the nodal order reduction via bilinear conformal transformation is used with Laguerre parameters corresponding to - 1) the mid frequency value, $2\pi \times 2.5e9$, 2) a value outside the suggested range, $2\pi \times 1.5e9$, 3) the values $\pi^2 \times 2.5e9$ and 4) $2\pi \times 5e9$. A comparison of these reduced models, each of order 10, with the original full-wave response is shown in Fig. 82 and Fig. 81. We see that for Laguerre parameters,$\alpha = 2\pi \times 1.5e9$, which is outside the range of suggested values, there is a definite convergence issue. For $\alpha = 2\pi \times 2.5e9$, the convergence is better, and for $\alpha = \pi^2 \times 2.5e9$, the convergence is the best. For $\alpha = 2\pi \times 5e9$, there is a lack of convergence towards the beginning of the frequency range.

Further, we see that the choice of the Laguerre parameter has a definite effect on
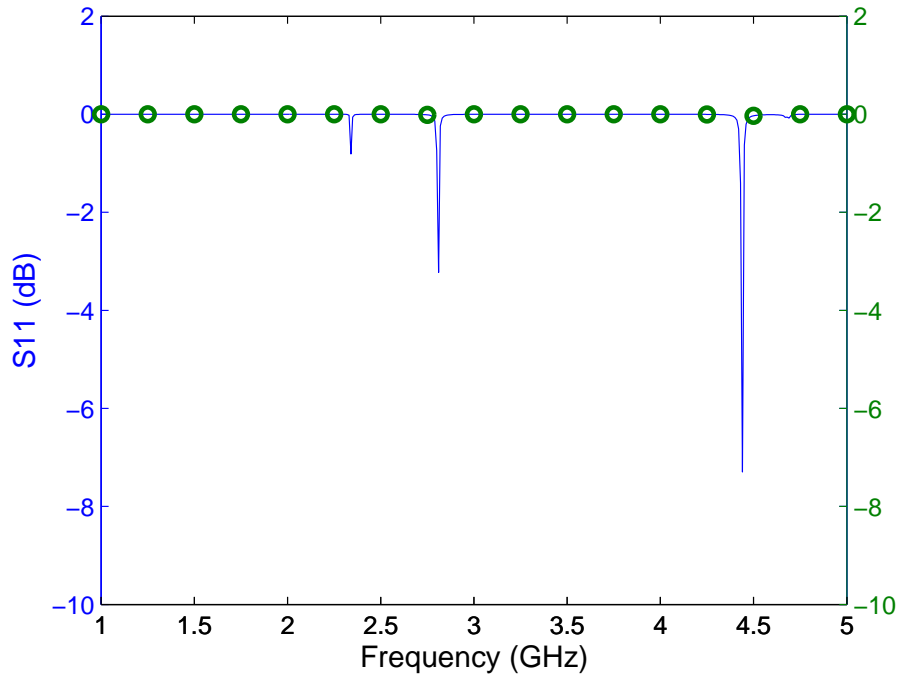
Figure 77: The return loss of the reduced model of order 15 (solid line) compared to the original full-wave simulation (circles) of the split power plane structure layout.

the speed of convergence of the reduced model to the original full-wave response. Another perspective on the choice of Laguerre parameter is in terms of the time constant of the system under consideration [37]. For finite difference based governing equations, this may is related to the upper bound of analysis frequency, which determines the discretization (based on the wavelength). We also know that the overall convergence of the process is dictated by the poles near the end points of the frequency range. Moving the Laguerre parameter very close to either of these points may result in longer time for convergence of results at the other end point. Also, an additional requirement is that the Laguerre parameter should be of the same order as the bandwidth of the system. A balancing act is needed between the radius of convergence, determined by the value of Laguerre parameter, and the order of the solution, which is determined by the proximity of the Laguerre parameter to the end points of the frequency range. Keeping all these factors in mind, for a range of interest $[f_{min}, f_{max}]$,
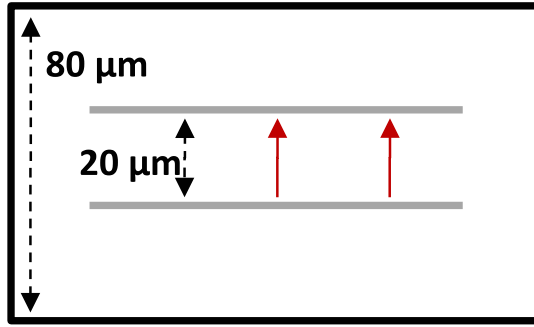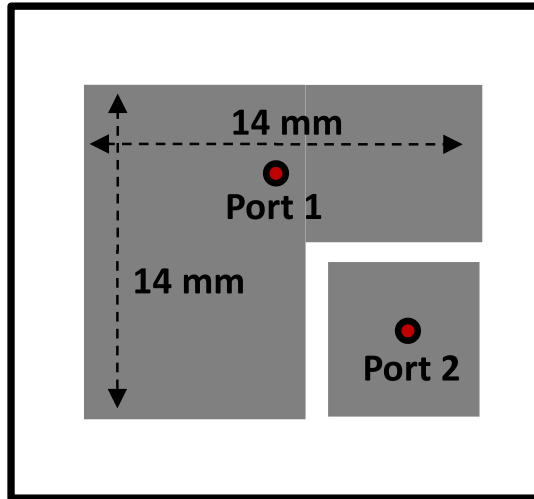
Figure 78: The (a) cross-section and (b) top-view of the layout of the split power island structure

it is best to choose the Laguerre parameter as: $\pi(f_{max} + f_{min}) \leq 2\alpha < 2\pi f_{max}$ This choice of Laguerre parameter between the mid-point and the upper frequency bound, keeps the required reduced order lower, and at the same time provides enough radius of convergence.

6.5 Multi-point Reduction via Bilinear Conformal Transformation

The derivation starts with the second order nodal analysis equations described below

$$\left(\mathbf{G} + s\mathbf{C} + \frac{\Gamma}{s}\right)\mathbf{V}(s) = \mathbf{B}\mathbf{U}(s) \tag{81}$$
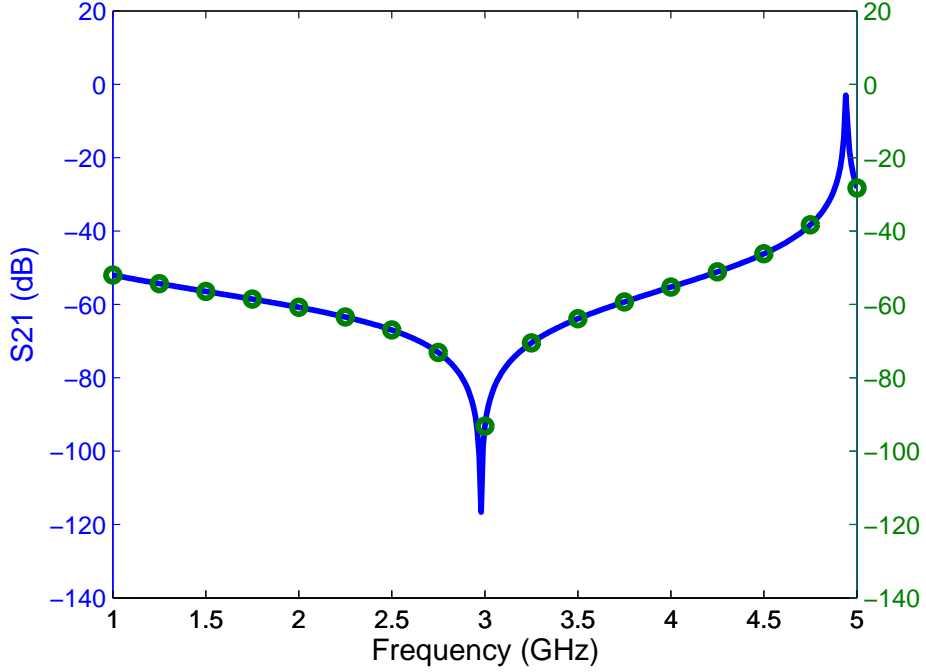
Figure 79: The insertion loss of the reduced model of order 10 (solid line) compared to the original full-wave simulation (circles) of the split power island structure layout.

The advantage of using these equations, apart from solving for only half the number of unknowns, is that they retain passivity and reciprocity when a congruent transformation based reduction is applied on them [60]. We then proceed to define a set of expansion points, $s_i, i = 0, 1, ..., n$, for which the bilinear conformal transformation may be defined as,

$$s = s_i \frac{1 - z^{-1}}{1 + z^{-1}}, \tag{82}$$

By using the above transformation (82) in (22), we get the nodal equations in the z-domain as

$$\left(\mathbf{G} + s_i \frac{1 - z^{-1}}{1 + z^{-1}} \mathbf{C} + \frac{(1 + z^{-1})\Gamma}{s_i(1 - z^{-1})} \right) \mathbf{V}(z) = \mathbf{B}\mathbf{U}(z) \tag{83}$$

After expanding $\mathbf{V}(z)$ and $\mathbf{U}(z)$ in powers of z, and then equating like powers, a recursive relation can be obtained for the column vectors which form the basis for projection matrix.
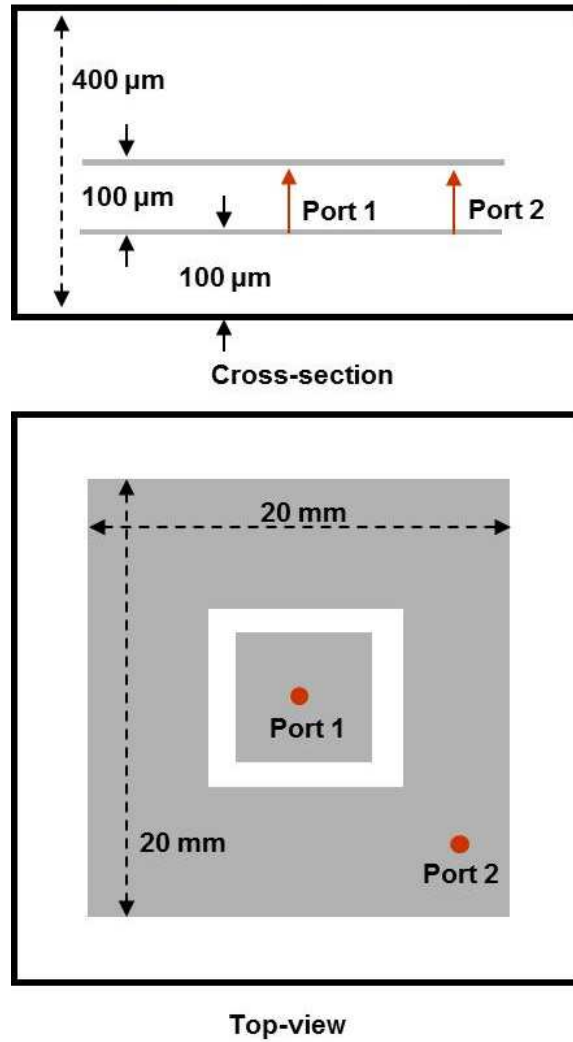
Figure 80: The layout of the power island structure.

The process of obtaining the multi-point second order bilinear conformal transformation based projection matrix is shown in Fig. 83.

At each expansion point s_i, the recursive calculation is carried out for an order, r_i. Orthogonalization, with on-the-fly deflation of the basis vectors is carried out to ensure to ensure the generation of a full-rank projection matrix. In the z-domain, the first $q(= \sum_i r_i)$ moments of the transfer function of the reduced system match the first q moments of the original system's transfer function. To preserve the passivity of the system after reduction, its reduced transfer function, $\tilde{H}(s)$, must obey the following rules:
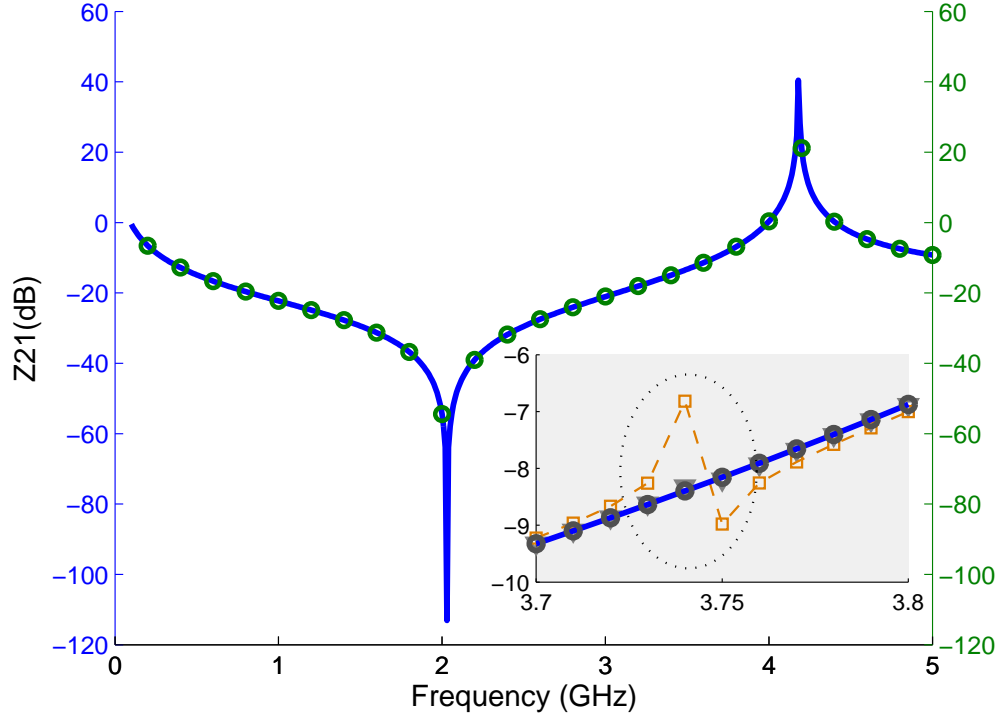
Figure 81: The transfer impedance response for the power island structure obtained using full-wave model (circles), and reduced order models with Laguerre parameters 1) $2\pi \times 2.5e9$ (triangle), 2) $2\pi \times 1.5e9$ (squares), and 3) $\pi^2 \times 2.5e9$ (solid).

1. $\tilde{H}(s)$ is analytic in s.

2. $\tilde{H}(s^*) = \tilde{H}^T(s)^*$

3. $z^*(\tilde{H}(s) + \tilde{H}^*(s))z \geq 0, \forall z \in \mathbb{C}$, and $\forall s \in \mathbb{C}$ with $\Re(s) > 0$

As has been discussed before in [48][60], the use of congruence transformation preserves the passivity of the system. In addition, the reciprocity of the system is also preserved by working on second order systems [60]. This projection matrix can then be used to reduce (81) through congruent transformation, to a reduced system of equations as shown below,

$$\left(\tilde{\mathbf{G}} + \tilde{\mathbf{C}}s + \frac{\tilde{\Gamma}}{s}\right)\tilde{\mathbf{V}} = \tilde{\mathbf{B}}\tilde{\mathbf{U}} \tag{84}$$
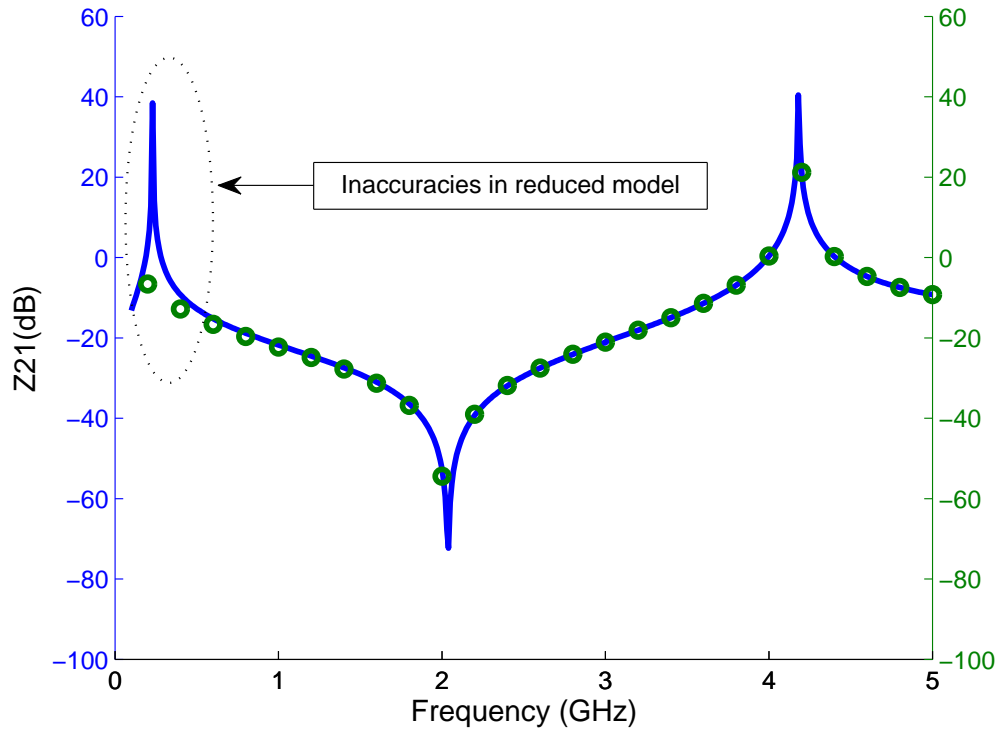
Figure 82: The transfer impedance response for the power island structure obtained using full-wave model (circles), and reduced order model with Laguerre parameters $2\pi \times 5e9$ (solid).

6.5.1 Numerical Test Cases

In this section we will first prove the efficiency of the model order reduction process with single point expansion and then proceed to a second test case showing the limitation of expanding at only one frequency point, thus motivating the application of the multi-point efficient nodal order reduction algorithm.

6.5.1.1 Transmission Line

The first example considered is that of a single transmission line. The transmission line is composed of 40 subsections of conductance (G), inductance (L), and capacitance (C), respectively. The coupling capacitance between the two lines is assumed to be C_c. This is illustrated in Fig. 84. The system of equations to solve for the nodal voltages can be written as in (22). The multi point second order bilinear conformal

90

```
k = 1
i = 0
while k ≤ r_i do
    if k == 1 then
        Solve: (G + s_i C + Γ/s_i) V_0 = BU
        V_0 = orth(V_0)
        Solve:           (G + s_i C + Γ/s_i) V_1       =
        2 (s_i C − Γ/s_i) V_0
        Orthonormalize V_1 against V_0, V_1
        T              =              2 (s_i C − Γ/s_i) V_1       +
        (G − s_i C − Γ/s_i) V_0 − BU
        Solve: (G + s_i C + Γ/s_i) V_2 = T
        Orthonormalize V_2 against V_0, V_1, V_2
    end if
    k = 3
    T              =              2 (s_i C − Γ/s_i) V_{k−1}       +
    (G − s_i C − Γ/s_i) V_{k−2}
    Solve: (G + s_i C + Γ/s_i) V_k = T
    Orthonormalize V_k against V_0, V_1, ..., V_k
    if i ≤ n && k < r_i then
        k = k + 1
    end if
    if i < n && k == r_i then
        k = 1
        i = i + 1
    end if
end while
Q = [V_0, V_1, ..., V_q]
G̃ = Q^T G Q,  C̃ = Q^T C Q,
Γ̃ = Q^T Γ Q,  B̃ = Q^T B,  Ũ = UQ
```

Figure 83: The second order multi-point reduced order modeling algorithm using bilinear conformal transformation

transformation based reduction is then applied to suitably reduce the system. The respective values used in the simulation are $G = 4$ S, $L = 0.125$ nH, $C = 0.375$ pF and $C_c = 0.0375$ pF. The ports one and two are defined across the ends of the transmission line. Fig. 85 shows the results, comparing the original simulation, with those obtained from the multi-point expansion scheme described above. Fig. 86 shows an
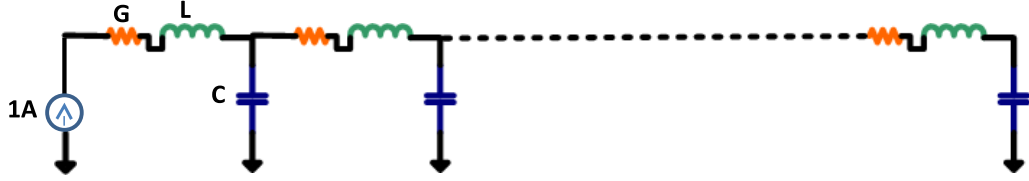
Figure 84: The transmission line represented by a distributed model with 40 sections.
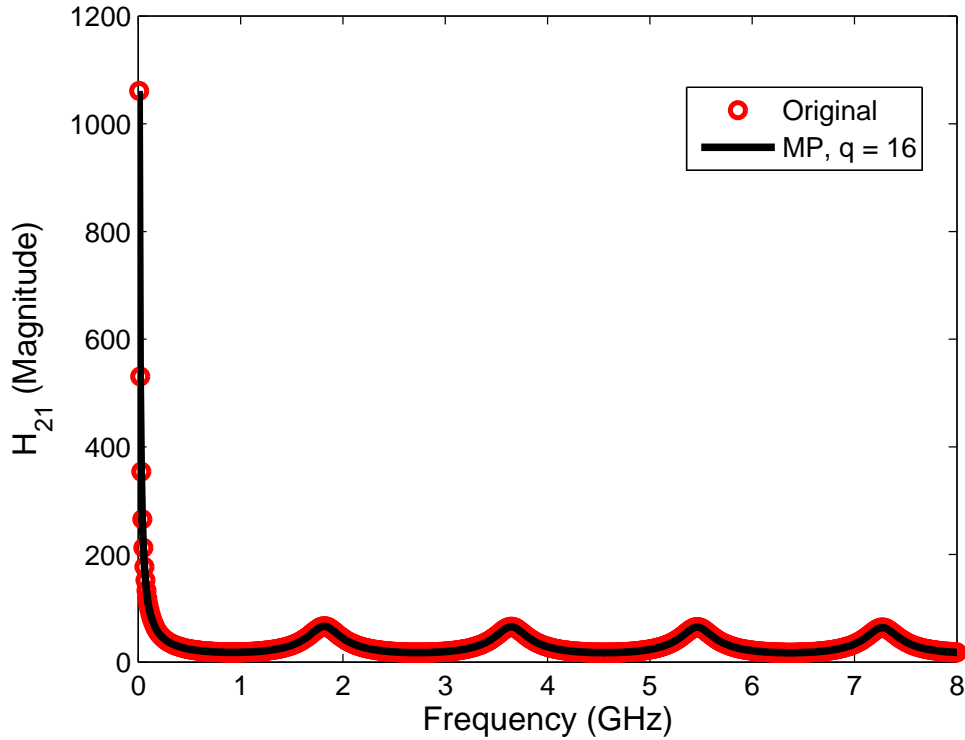
Figure 85: Comparison of the magnitude of the transfer function across ports one and two for the original and reduced models.

accurate match in the phase information obtained from the reduction with the phase of the original transfer function.

6.5.1.2 Test Structure - Electromagnetic Band-gap Structure

An electromagnetic band-gap structure as shown in Fig. 63 is considered. The metal patch has a dimension of 14 mm × 14 mm and the metal branch size has a dimension of 1 mm × 1 mm. Perfect electric conductor boundary conditions are assumed. The structure is discretized using a unit cell of dimensions 0.5 mm × 0.5 mm × 10 μm,
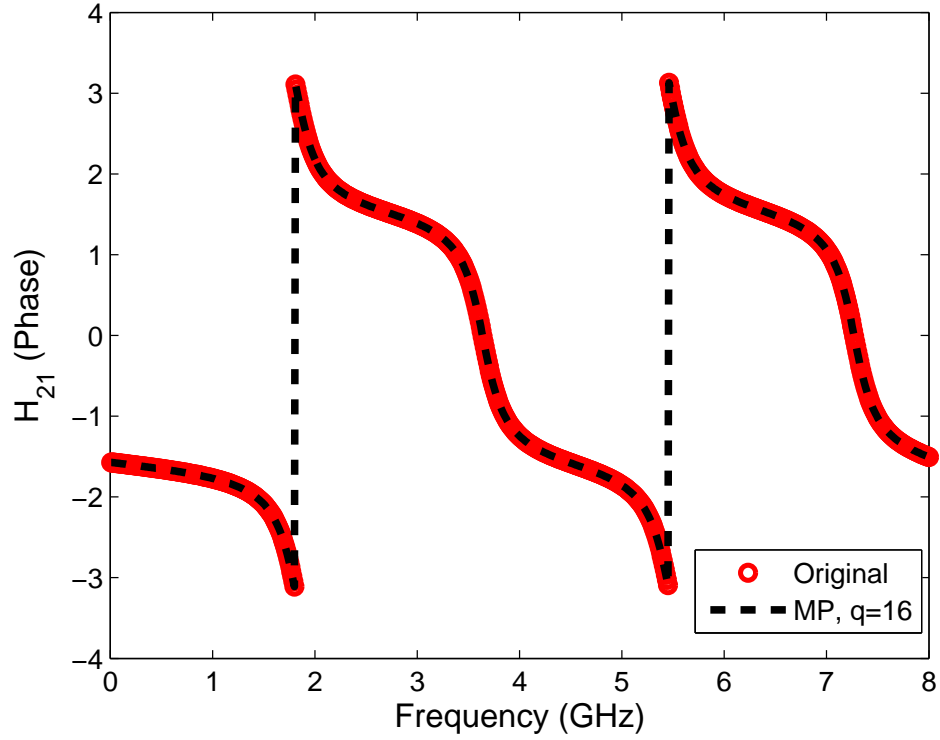
Figure 86: Comparison of the phase of the transfer function across ports one and two for the original and the reduced model obtained through multi-point nodal order reduction via bilinear conformal transformation.

resulting in approximately 42 000 unknowns. A homogeneous medium of dielectric constant, $\epsilon_r = 4.5$ is assumed throughout. Using the the SEEC model, a second order system of equations can be obtained to describe the structure. Fig. 88 shows the transmission coefficient of the structure obtained using full-wave and the reduced models. The inset clearly shows that the bilinear conformal transformation based approach is better at approximating the original system.

The reason for better properties is the fact that, in the improved efficient nodal order reduction method, an approximation is made while obtaining the recurrence relation for the basis vectors. The summation equation (corresponding to (13) in [80]) is shown below

$$V_k = PV_{k-1} + Q \sum_{k-1}^{i=0} V_i, k > 0, \tag{85}$$

93
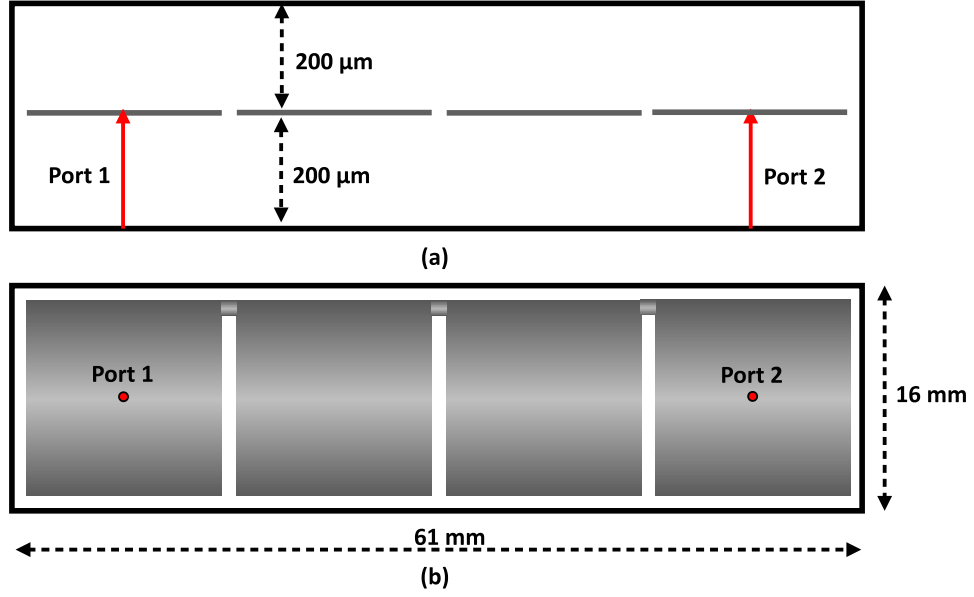
Figure 87: The (a) cross-section and (b) top-view of the layout of the electromagnetic band-gap structure

wherein, P and V are coefficient matrices determined by the admittance matrices of the system. This summation is terminated at the second term resulting in an altered recurrence relation as shown below,

$$V'_k = PV'_{k-1} + QV'_{k-1} + QV'_{k-2}, for k > 0. \tag{86}$$

However, for the bilinear conformal transformation based second order reduction method, no such summation arises. The calculation of the basis vectors in an iteration is thus free of any numerical noise due to termination of a series.

6.5.1.3 Coupled Transmission Line

The next example considered is that of a capacitively coupled transmission line pair. Each of the transmission lines is through 40 subsections of conductance (G), inductance (L), and capacitance (C) respectively. The coupling capacitance between the two lines is assumed to be C_c. This is illustrated in Fig. 89. The system of equations to solve for the nodal voltages can be written as in (22). The multi point second order bilinear conformal transformation based reduction is then applied to suitably reduce
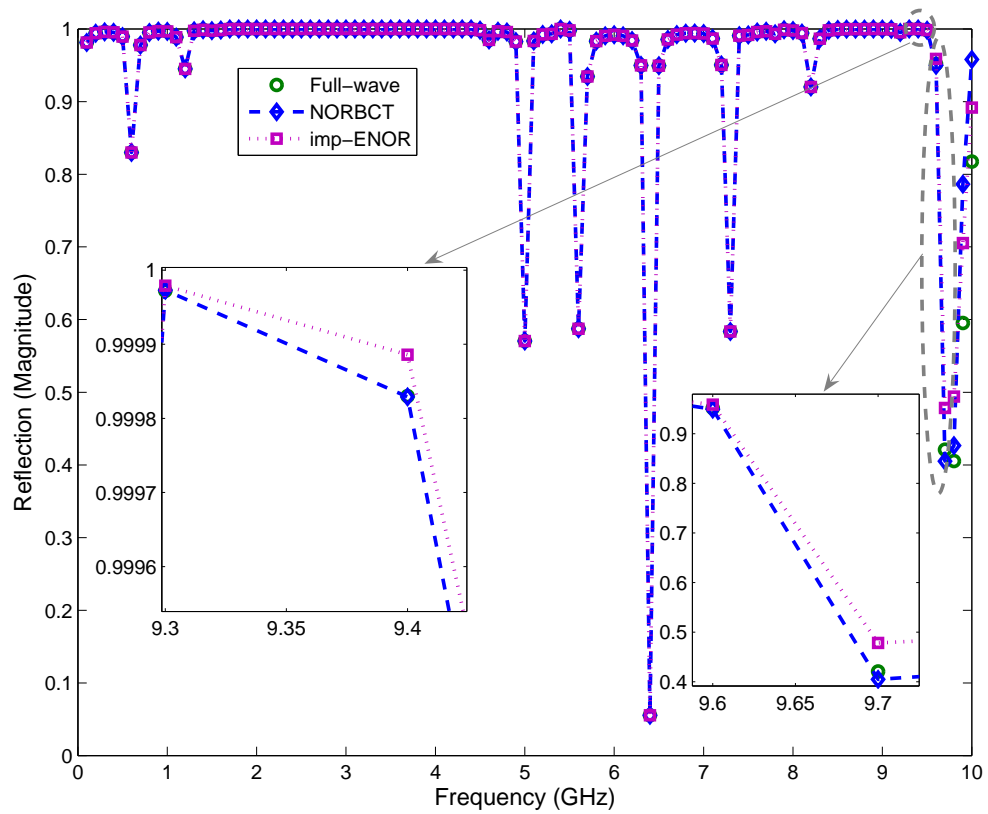
Figure 88: The comparison of the insertion loss response for the original and reduced models.

the system. The respective values used in the simulation are $G = 4$ S, $L = 0.125$ nH, $C = 0.375$ pF and $C_c = 0.0375$ pF. The ports one and two are defined across the first transmission line, and ports three and four are defined across the other line. Fig. 90 shows the results, comparing the original simulation, with those obtained from the multi-point expansion scheme to the single point reduction scheme [46], with the order of expansion, q, varying as 10, 15, and 20. As shown in the zoomed-in portions of the simulation (insets of Fig. 90), the reduced system of order 16 obtained by the multipoint expansion approach is able to better approximate the original simulation, than the reduced system of order 20 obtained from the method in [46]. Fig. 91 shows an accurate match in the phase information obtained from the reduction with the phase of the original transfer function.

95
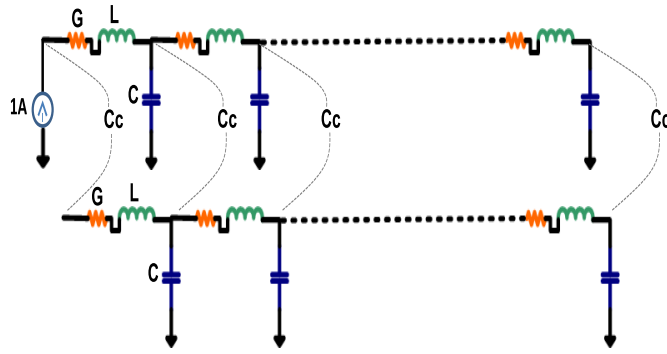
Figure 89: The coupled transmission line pair with 40 sections.
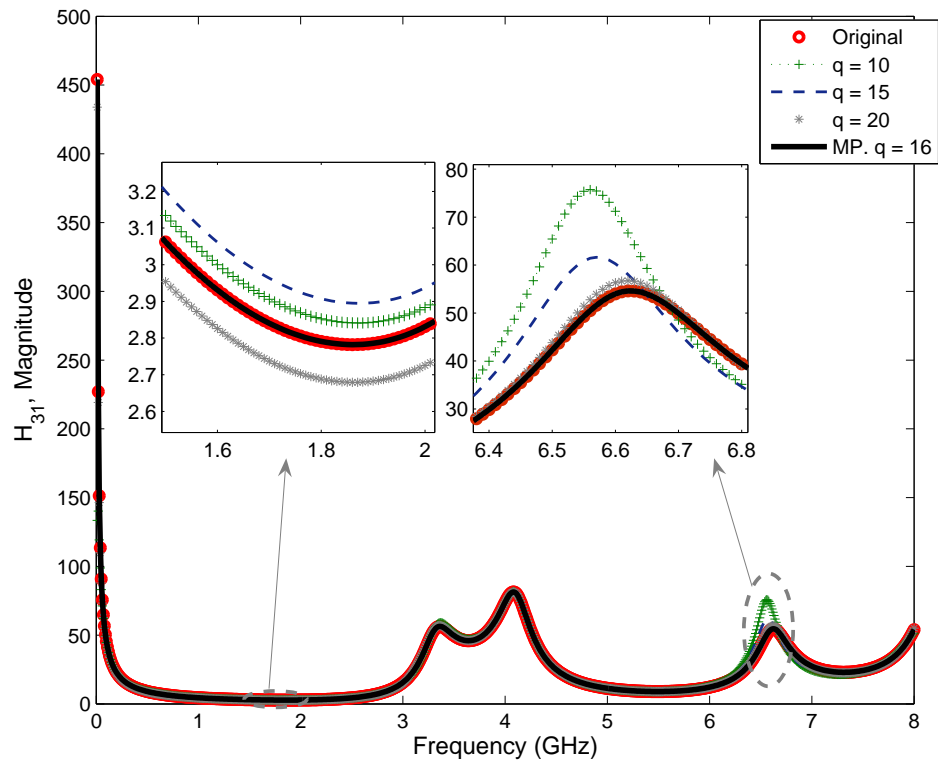
Figure 90: Comparison of the magnitude of the transfer function across ports one and three for the original and reduced models..

In conclusion, the multi-point second order reduced order modeling via bilinear conformal transformation has been shown to be an effective tool in approximating transfer functions of electromagnetic systems, with improved properties over the corresponding single point approximation as well as the improved efficient nodal order
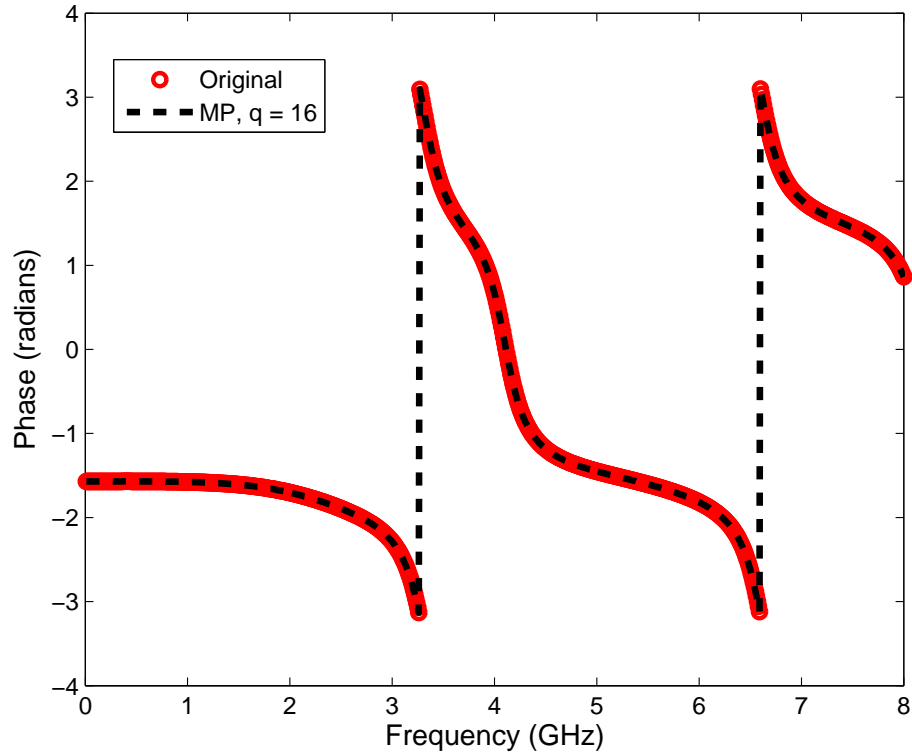
Figure 91: Comparison of the phase of the transfer function across ports one and three for the original and the multi-point nodal order reduction via bilinear conformal transformation.

reduction algorithm.

6.5.1.4 Stripline Via Transition

A stripline via transition structure as shown in Fig. 92 and Fig. 93. The symmetric stripline structure has a width of 400 μm with a dielectric thickness of 500 μm and dielectric constant of 4.4. The dimension of the via is 200 μm × 400 μm with a via hole of size 400 μm × 800 μm. The structure is simulated using the SEEC model with a unit cell of size 100 μm × 200 μm × 500μm, as well as the multi-point nodal order reduction via bilinear conformal transformation algorithm. Results of the simulation are shown in Fig. 94 and Fig. 95, illustrating an accurate match between the reduced (q = 10) and the original simulation.
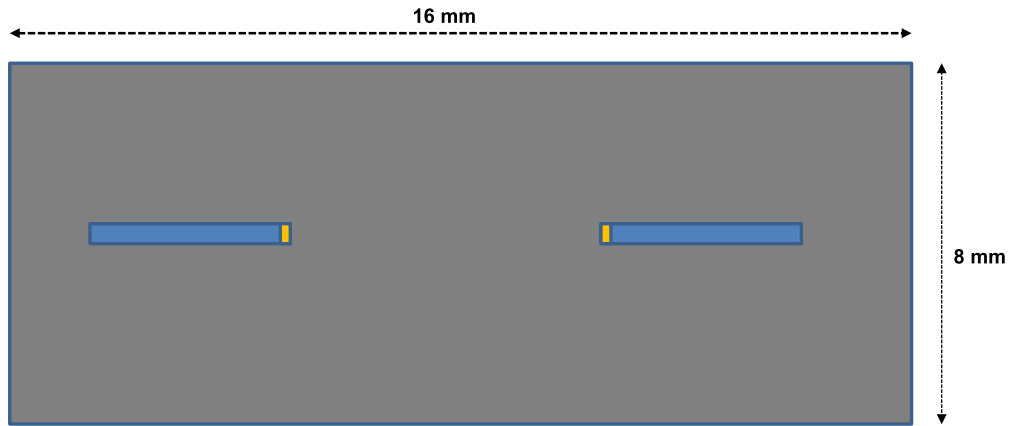
Figure 92: Top-view of the stripline via transition structure.
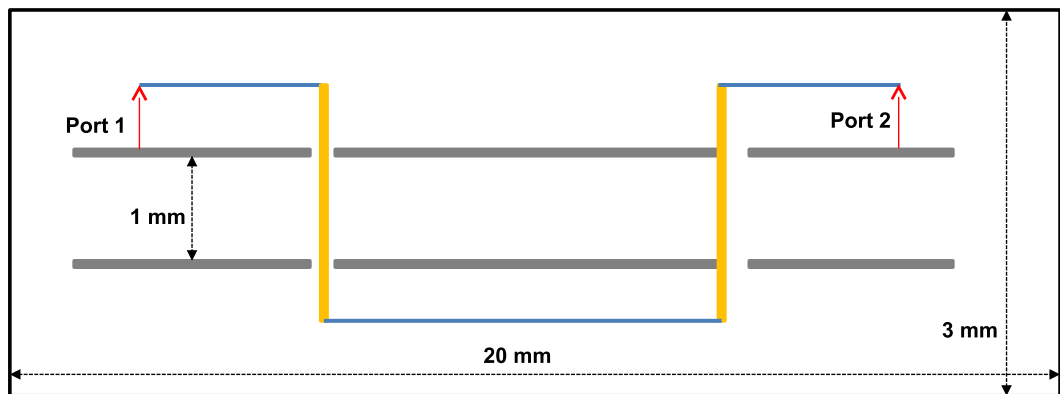
Figure 93: Cross-sectional view of the via transition structure.

6.5.1.5   Five Layer Structure with Apertures

Further, the model order reduction for a large size example was carried out. A five layer stack-up of metal planes as shown in Fig. 96 was considered. The number of unknowns resulting from the discretization was approximately 4.6 millions. The multipoint nodal order reduction via bilinear conformal transformation algorithm was applied to the layout and a reduction to order 12 was obtained. The Laguerre shifts were chosen to be 2 GHz and 4 GHz. Fig. 97 shows an accurate comparison between the original SEEC model and the reduced order model.
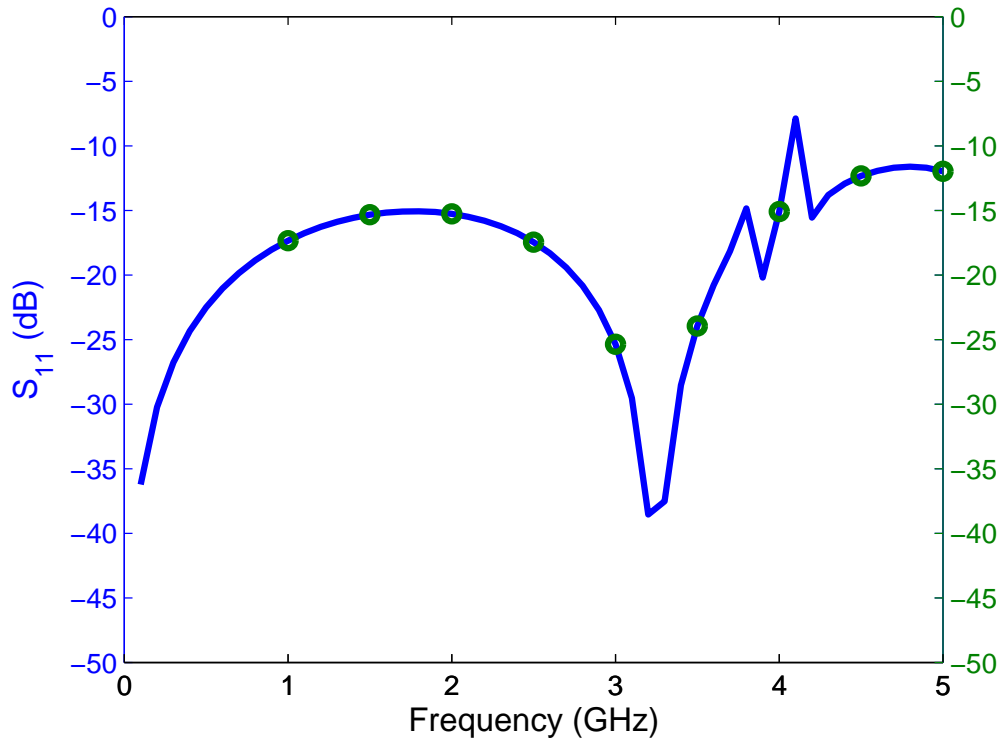
Figure 94: The return loss of the stripline via transition structure for the original (circles) and the reduced (solid) model.

6.6 Electromagnetic/Lumped-element Model Order Reduction

The model order reduction of lumped elements in combination with the electromagnetic Yee field cells is not straightforward. If we were to add these elements in terms of an equivalent admittance, the resulting equations have order greater than two rendering it impossible to use the afore-mentioned second-order reduction methods. A way to overcome this was described in [11], wherein for lumped elements, the corresponding equations for electromagnetic field values are calculated for the nodes in direct relation to the additional lumped elements. Consider the addition of the decoupling capacitor shown in Fig. 36 to the SEEC model of the power plane. The easiest way to do this is to write out the equivalent admittance of the decoupling capacitor as

$$Y_{decap} = \frac{j\omega C}{1 - \omega^2 LC + j\omega RC}. \tag{87}$$
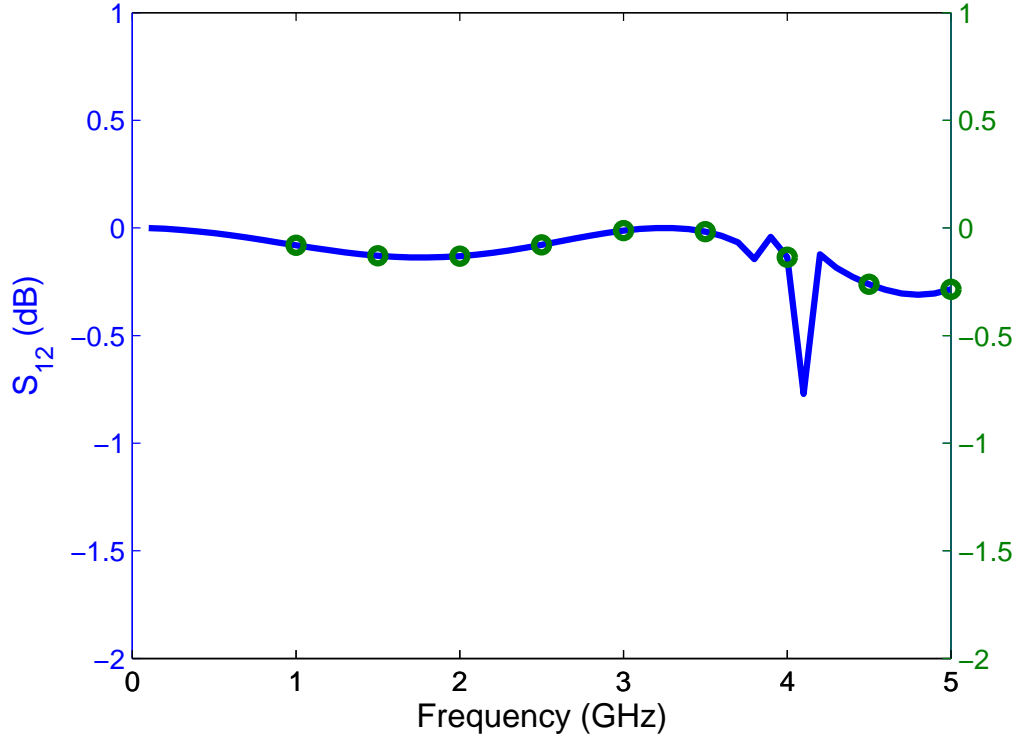
Figure 95: The insertion loss of the stripline via transition structure for the original (circles) and the reduced (solid) model.

and then substitute this in the SEEC model equation (given by (22) for the power plane pair, resulting in

$$\left(\mathbf{G} + s\mathbf{C} + \frac{\Gamma}{s}\right)\mathbf{V} + \mathbf{YV} = \mathbf{BI} \tag{88}$$

where $\mathbf{Y}$ contains entries at nodes corresponding to where the decoupling capacitor has been added. However, as can be seen the SEEC structure of the original equation (22) is broken in (88). A way around this is to treat each node of the decoupling capacitor equivalent circuit separately, and map the current voltage relationship at each of those nodes to the electric field equations of the SEEC model, as shown in Fig. 98

This combined framework is then used for model order reduction allowing the use of second order reduction methods.

Plane Size: 14 mm x 14mm
Large Aperture: 6mm x 6mm
Small aperture: 1mm x 1mm
Vertical spacing: 20 microns
Dielectric permittivity 3.8
Discretization unit cell (125x125x5) microns
# of unknowns = 4.6 millions
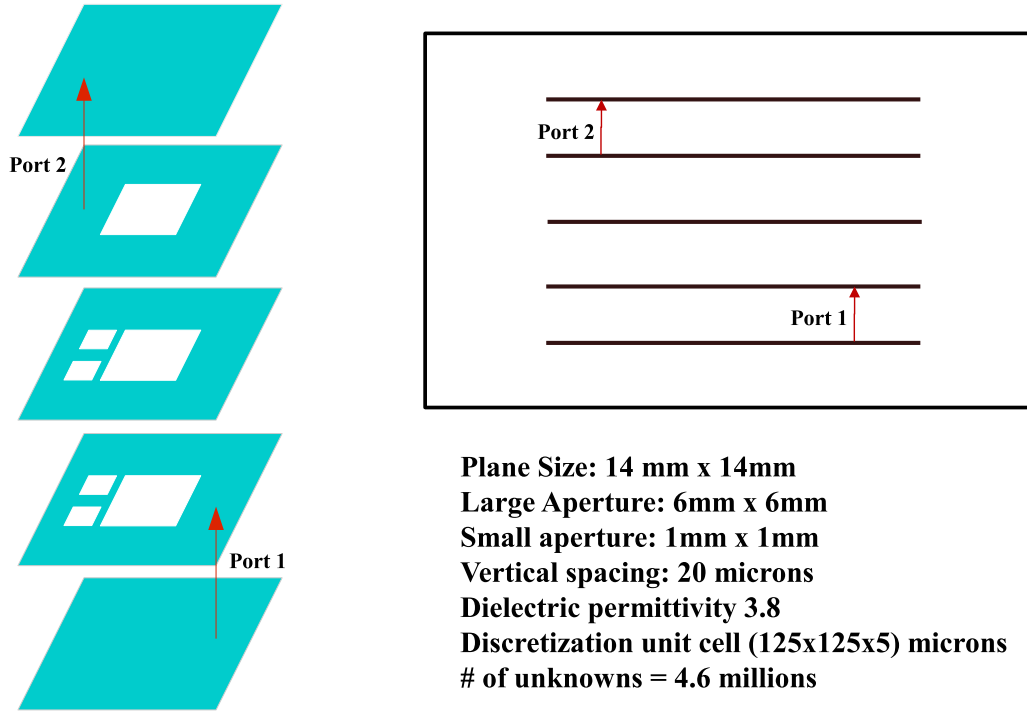
Figure 96: The layout of the five layer structure showing port placement.

6.6.1 Numerical Test Case

6.6.1.1 Power Plane with Decoupling Capacitors

Finally, we consider an example of full-wave SEEC/ lumped circuit element co-simulation with reduction. The example shown in Fig. 40 is considered. Additional nodal equations are written for the lumped circuit elements, and then the NORBCT algorithm is applied. A comparison of the impedance response for the original and reduced systems, for cases with and without decoupling capacitors is shown in Fig. 99. The original system with 15, 000 unknowns is reduced to order, q = 10. The computational time per iteration is reduced from 26 second to 0.2 milliseconds.

6.7 Summary

A second order reduced order modeling scheme based on bilinear conformal transformation has been developed, resulting in improved performance over the reduction method based on linear transformation. The corresponding multi-point version of the
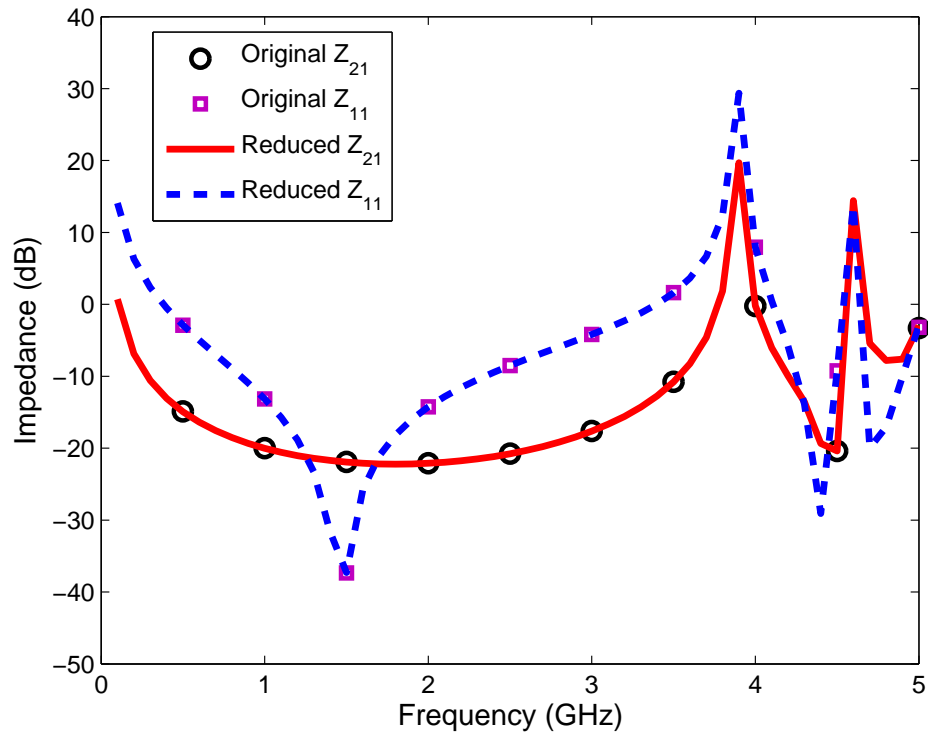
Figure 97: Results of the impedance response showing accurate match between the reduced and original model.
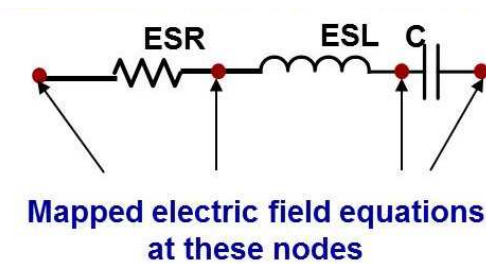
Figure 98: The mapping of electric field equation at additional nodes of the decoupling capacitor.

algorithm showed, as expected, greater efficiency in capturing the network response accurately, as compared to the single point version. The algorithm was successfully applied to lumped elements, as well as to the SEEC model. Further, electromagnetic/lumped circuit element co-simulation through the application of the NORBCT algorithm has also been shown. The difficulty in applying the model order reduction technique directly to electromagnetic/lumped circuit element cosimulation has been

102
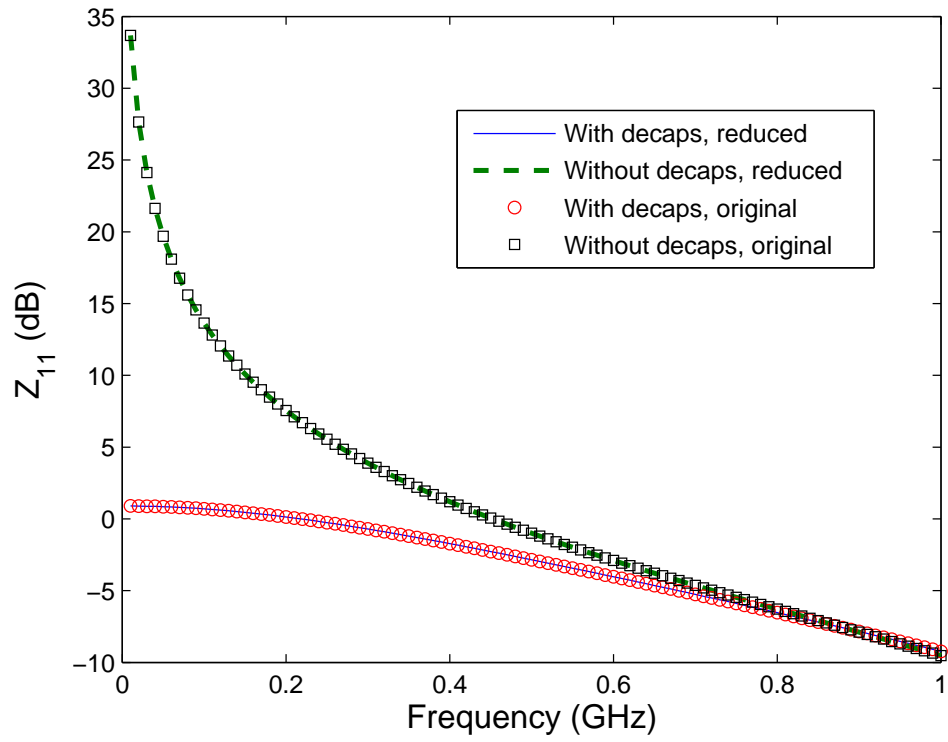
Figure 99: The impedance response of the power plane pair, with and without decoupling capacitors, for the original and the reduced systems.

overcome by applying nodal analysis to write equations for electromagnetic fields corresponding to the added lumped circuit elements.

CHAPTER VII

CONCLUSION

The drive in the integrated circuits industry towards miniaturization and multi-functional platforms is leading to complex multiscale geometries, with mixed signal effects at high operating frequencies. While transistor scaling has kept pace, the package and interconnect design may turn out to be the bottleneck in meeting these requirements. The efficient design of packages for such platforms requires efficient ways of modeling and analyzing the package geometries, to capture the electromagnetic effects accurately, as well as efficiently. Efficiency here being defined in terms of being able to solve very large problems by using less memory and within a reasonable amount of time. Indeed, accurate fast methods for electromagnetic simulation become absolutely critical to reduce the burden on the design cycle time, as well as improving yield of the manufacturing process. Both the afore-mentioned features, design cycle time and yield, ultimately affect the cost of production, and thus the accuracy and speed of simulation become all the more relevant in a commercial sense as well. The contribution of this thesis pertains to this aspect - fast methods for efficient electromagnetic simulation.

7.1 Contribution

7.1.1 Susceptance Element Equivalent Circuit Model

Firstly, the susceptance element based equivalent circuit electromagnetic solver has been developed. In respect of the previous work in this domain, this is significant in two aspects - 1) it is second order in nature, and therefore gives rise to very useful properties, which can be capitalized for model order reduction, and 2) it is differential equation based, and thus solves for all field components, and therefore by virtue of

discretization over the entire volume, is easily able to capture complex geometries of varied shapes, as well as the various electromagnetic phenomena arising therefrom. In terms of designing packages, an equivalent circuit based solver makes it easier for the engineer to relate physical phenomena directly to a passive network element, in terms of inductance, resistance, capacitance or current sources.

7.1.2 Second Order Reduced Order Modeling

Secondly, in terms of fast methods, an already existing second order reduced order modeling method, the improved efficient nodal order reduction algorithm, was successfully applied showing a significant reduction in the simulation time. Subsequently, the multipoint efficient nodal order reduction algorithm was developed, which was shown to have considerable performance improvements over the single point expansion version. Further investigation was done into using bilinear conformal transformation, instead of the linear transformation used in the previous two methods, resulting in the nodal order reduction via bilinear conformal transformation algorithm. Investigation into the choice of the Laguerre parameter was done, and it was also shown that this algorithm intrinsically removed an approximation associated with the improved efficient nodal order reduction method. The corresponding multipoint expansion algorithm based on bilinear conformal transformation was developed as well. All of the above algorithms were successfully applied on the suscpetance element equivalent circuit model resulting in significant reduction in the size of the problem, and therefore the simulation time. By using a second-level preconditioned Krylov subspace process, the memory requirement was also kept low.

7.2   Publications

Journal

- Narayanan T.V. , Madhavan Swaminathan, "Preconditioned Second Order Multipoint Passive Model Order Reduction for Electromagnetic Simulations," *IEEE*

Trans. Microwave Theory Tech., vol. 58, no. 11, 2010, pp. 2856-2866.

- Narayanan T.V. , Madhavan Swaminathan, "Second Order Reduced Order Modeling based on Multi-point Bilinear Conformal Transformation," *IEEE Microwav. Comp. and Lett.* (*submitted*)

Conference

- Narayanan T.V. , Krishna Srinivasan, Madhavan Swaminathan, "Fast Memory-Efficient Full-Wave 3D Simulation of Power Planes," IEEE International Symposium on Electromagnetic Compatibility, 2009.

- Narayanan T.V., Sung-Hwan Min, Madhavan Swaminathan, "Accelerated Frequency Domain Analysis by Susceptance-Element Based Model Order Reduction of 3D Full-wave Equations," 18th conference on Electrical Performance of Electronic Packaging and Systems, 2009.

- Narayanan T.V. , Madhavan Swaminathan, "Nodal Order Reduction via Bilinear Conformal Transformation," 14th IEEE Workshop on Signal Propagation on Interconnects, 2010.

- Narayanan T.V. , Madhavan Swaminathan, "EM/Lumped-Circuit Element Co-simulation using Z-domain Krylov Subspace Model Order Reduction," Semiconductor Research Council TECHCON, 2010.

- Narayanan T.V., Madhavan Swaminathan, "On the choice of laguerre parameter in nodal order reduction via bilinear conformal transformation," 19th conference on Electrical Performance of Electronic Packaging and Systems, 2010.

CHAPTER VIII

FUTURE WORK

While the work in this thesis addresses concerns of fast electromagnetic simulation, it also provides scope for future work in various aspects described below:

8.1 Domain Decomposition

When dealing with multiscale structures, meshing the entire volume of discretization, with fine and large geometries, at the same time and then applying the reduction methods is ineffcient. This can be improved by using domain decomposition technique. The idea being to separate the different scales of geometries in different regions of analysis. Each region is then solved separately, the crucial part being accounting for the solution at the interface of these regions. The process is illustrated in Fig. 100.
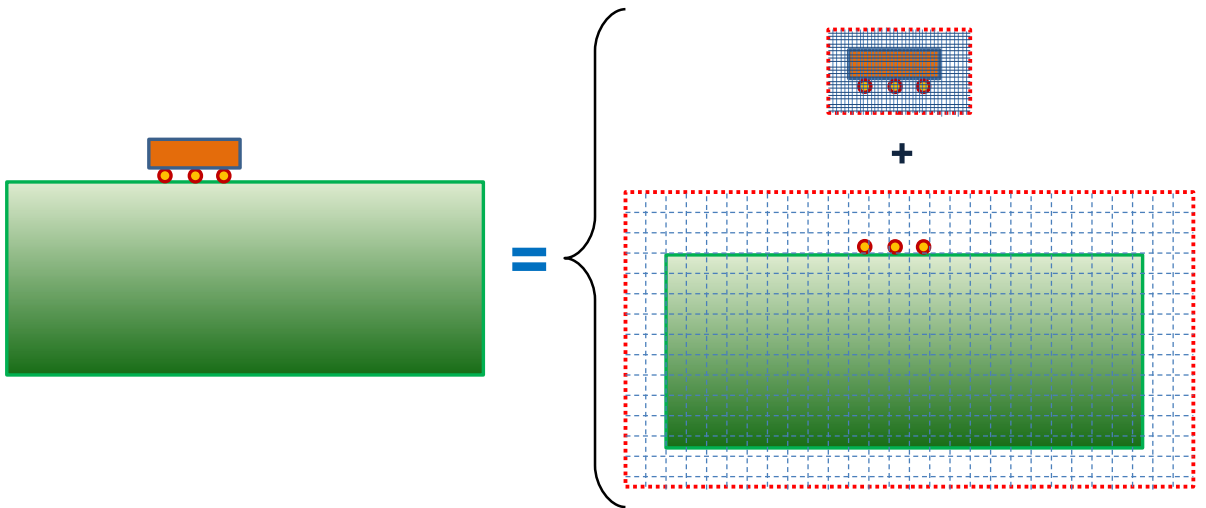
Figure 100: The concept of domain decomposition for multiscale structures.

8.2 Low Frequency Solution

As described earlier, the second order equations face a problem in solving for the fields at low frequencies (in the order of a few kilo Hertz or lower). While there is work in existing literature, which rely on quasi-static simulations [7] or on the co-tree splitting technique for the finite element scheme [39], these methods face issues with respect to generality of their applications. In this respect, a recent work based on an eigenvalue solution for overcoming the low frequency breakdown issue [81] showed improved performance, both in terms of accuracy and generality. This was implemented for the purely lossless case for the SEEC model. A 16 mm × 16 mm thin metal plane was considered, placed at the center of a dielectric box of dimensions 24 mm × 24 mm × 60 μm, similar to the structure shown in Fig. 31. The dielectric constant of the homogeneous medium enclosed in the PEC box is 3.8. Fig. 101 shows the reponse obtained though this implementation, seamlessly joining with the normal SEEC simulation at higher frequencies. To improve on the generality of the SEEC model, a similar effort could be made to solve the SEEC model at lower frequencies for problems involving conductor and dielectrics.

8.3 Three Dimensional Structures

To truly capture the three dimensional nature of future packages, the simulation of through silicon vias (TSV) becomes imperative. However, the meshing of these structures would result in a large increase in the number of unknowns. To over come this computational burden, a hybrid approach is proposed, wherein, an in-house solver based on cylindrical conduction mode basis function [25] is used in combination with the SEEC model. Once the two-port network of the TSV is obtained, the aim is to map the data to equivalent current density sources in the SEEC model. This is illustrated in Fig. 102, where these current density terms are added to the SEEC model. The simulation of a transition of a microstrip line through a TSV was carried
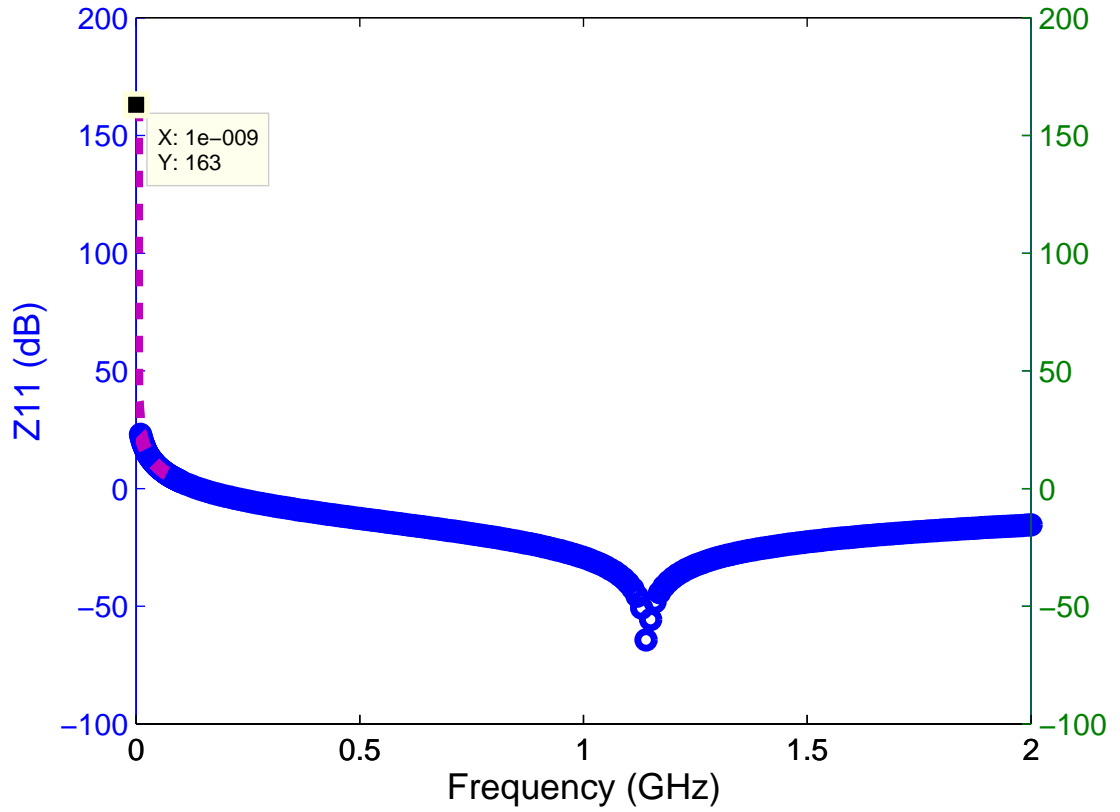
Figure 101: The response of the structure using the low frequency eigenvalue based solver (solid) seemalessly joining the SEEC model response (circles).

out as proof-of-concept. The structure is the same as shown in Fig. 102. The structure is enclosed in a PEC box of dimensions 2 mm × 1.2 mm × 340 μm, where above and below the microstrip line, there is air for 100 μm. The through silicon via has dimensions of 20 μm radius and 100 nm oxide thickness. The thickness of the silicon layer ($\epsilon_r = 11.9$ and $\sigma = 10$ S/m) is 100 μm and the dielectric RXP layer ($\epsilon_r = 2.5$) is 20 μm and the response obtained is shown in Fig. 103. However, to use model order reduction on these structures is not straightforward due to the associated losses. Therefore,to account for frequency dependent losses in the framework of the reduction methods presented in this thesis, parametrization needs to be introduced. Parametric model order reduction has been applied to account for the skin effect losses in [2]. A conceptual illustration of the future work is shown in Fig. 104, where
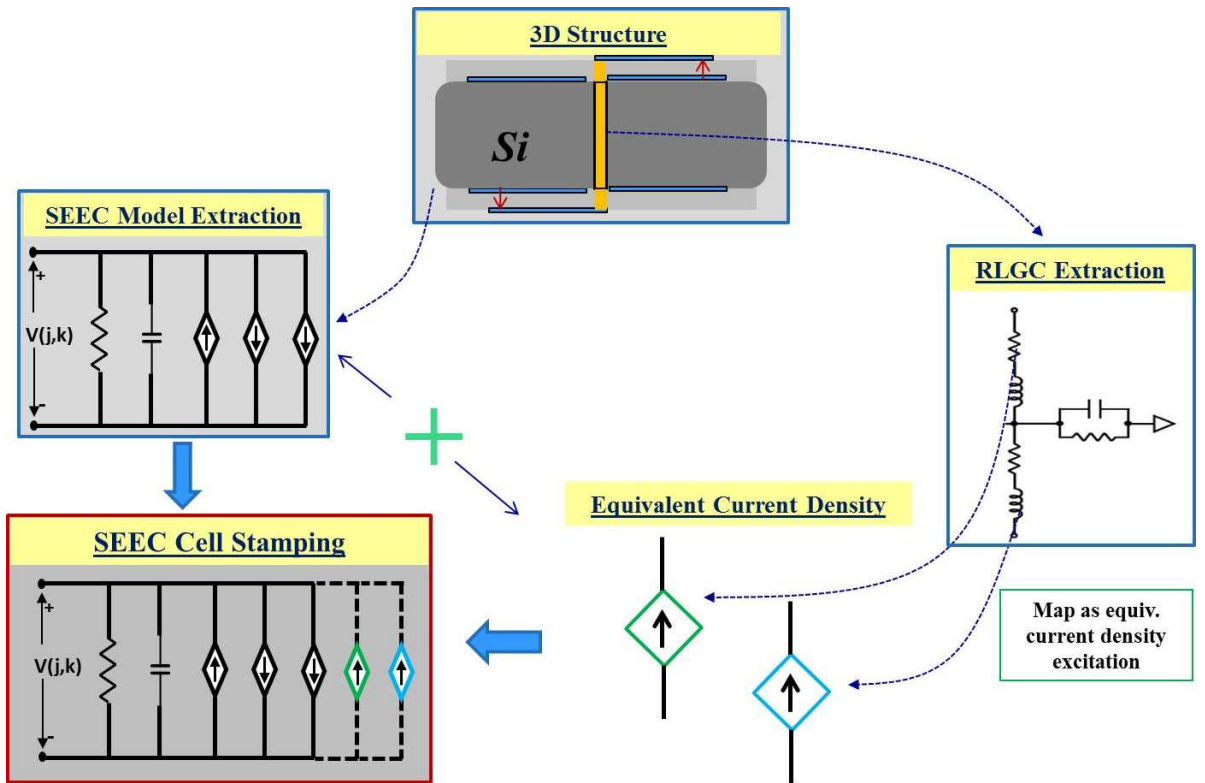
Figure 102: The stamping of TSV conduction mode basis solver [25] in the SEEC model.
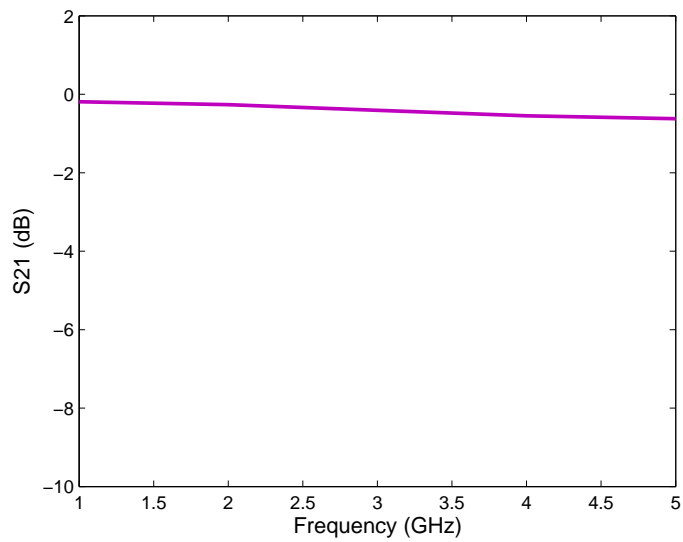
Figure 103: The response of the microstrip to microstrip transition through a TSV.

λ represents the set of variables being parametrized.
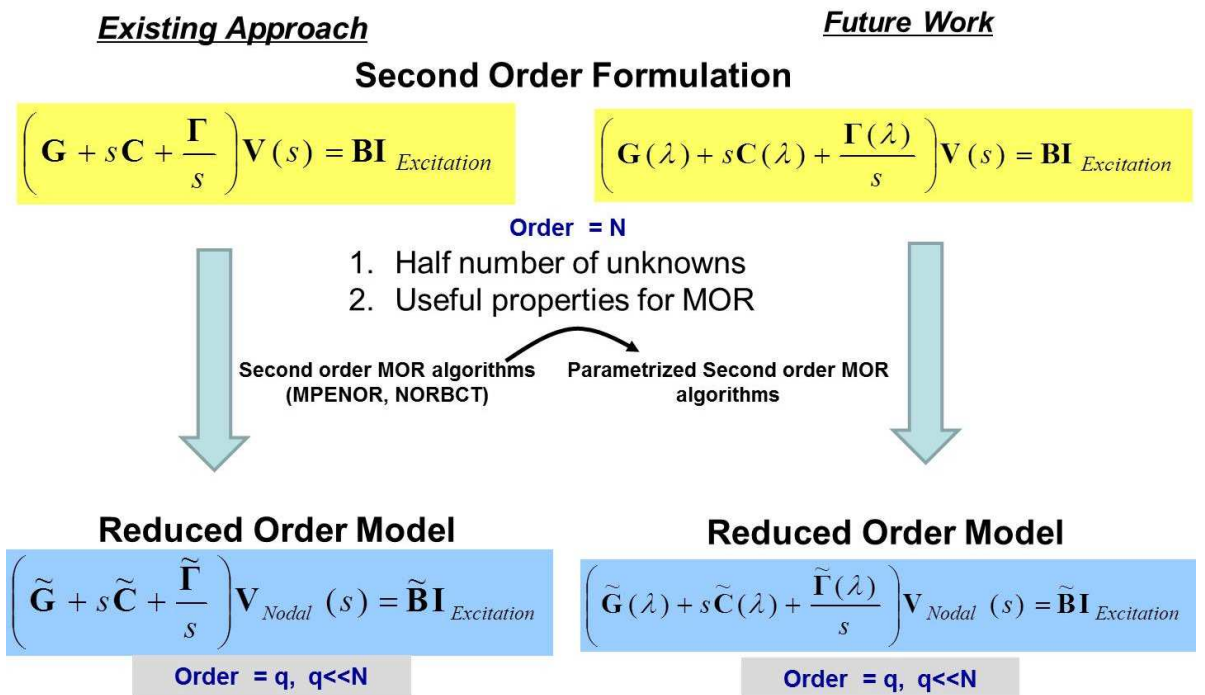
Figure 104: The conceptual flow of the parametrized model order reduction, as compared to the work in the present thesis.

APPENDIX A

LUMPED ELEMENT MODELING OF EMBEDDED PASSIVES

A.1   Introduction

During the initial phase of this dissertation, numerical methods to model embedded passives simulation results obtained from a commercial tool were explored. The idea was to move from electromagnetic simulation results to a physical lumped element model, capturing the inherent parasitics accurately. In view of the development of the SEEC model, it is proposed that the two methodologies be suitably combined. The following text discusses the lumped element modeling technique.

Modeling of embedded passives has been explored in recent past, with special significance attached to spiral inductors. Since spiral inductors form an important component in many RF applications - filters, baluns, voltage controlled oscillators, etc., the design of such modules requires an accurate spice-compatible model over a wide range of frequencies. Traditionally, the methodology for modeling has been either a physics-based lumped-element modeling or a state-space based "black-box" macromodeling, as shown in Fig. 105.
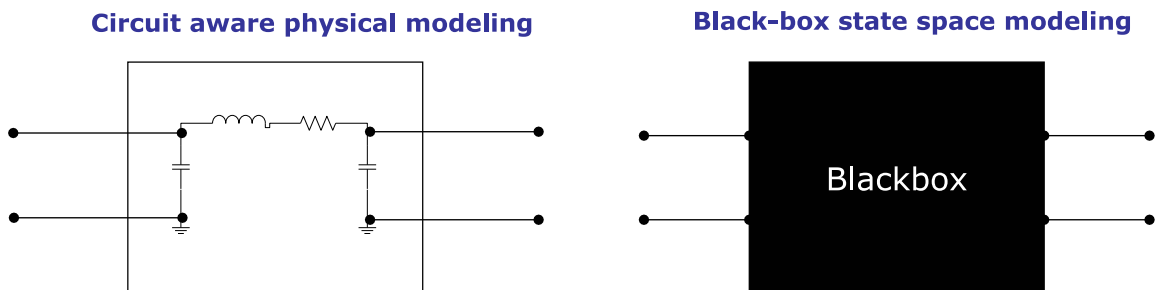
Figure 105: The two types of modeling techniques for embedded passives.

A.1.1 Physics-based Element Modeling

A.1.1.1 Lumped Element Models

Simple lumped element models have been used for modeling embedded passive components. Such schemes basically start by modeling the physical phenomena present in embedded components in terms of lumped elements, e.g, modeling the conductor by means of a resistor and inductor, and the dielectric part through a capacitor. The main disadvantage of such models is an inability to account for variations, especially in terms of substrate and conductor loss parasitics. Simple lumped element models are unable to model effects like current crowding, substrate coupling etc.

A.1.2 Black-box Modeling

The idea behind black-box modeling is to treat the simulation/measured response as a black-box, and then model it purely by approximating the terminal network parameters through a suitable mathematical technique, finally resulting in a circuit equivalent representation. However, this equivalent circuit has no correspondence to the physical phenomena of the structure, and is purely a realization of the mathematical approximation obtained.

A.1.2.1 Simple Augmentation

At the very basic level, both the simple lumped element model obtained as discussed in the previous section, and the structure being modeled are taken as black boxes. To model for the extra parasitics which may not be captured by the simple lumped element models, terminal augmentation is added. This is represented in Fig. 106. The idea here is to account for any difference between the two port network parameters of the simple model and the simulation/measured response by adding more lumped components at the model terminations to account for the difference.

Conventional Augmentation
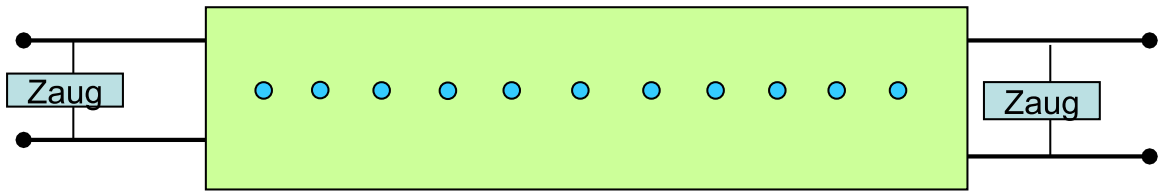
Figure 106: A simple augmentation technique working only on the terminal entries.
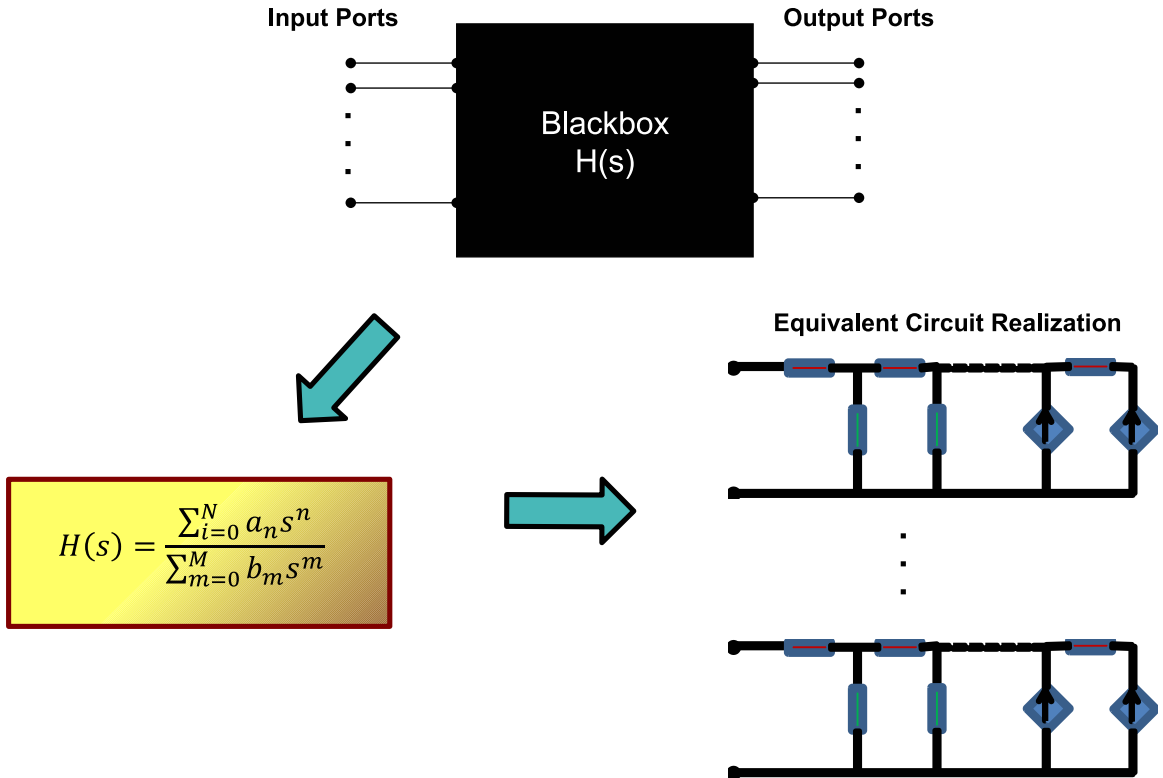
Figure 107: The concept of rational modeling for generation of equivalent circuit models for embedded passives.

A.1.2.2   Rational Function Method

There is considerable literature devoted to the area of macromodeling [1] [40]. Fig. 107 shows the basic concept of rational function modeling.

114

Augmentation with Circuit Partitioning
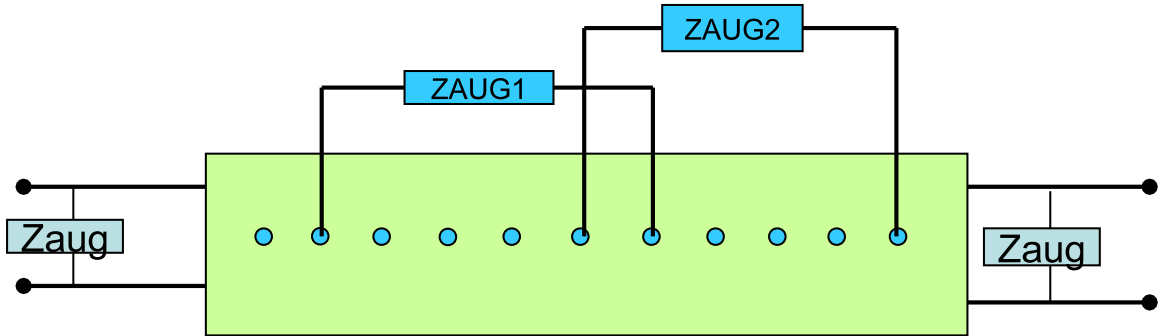
Figure 108: The concept of augmentation showing the ability to add lumped elements at any arbitrary node.

A.2   Linear-least squares Augmentation

The circuit augmentation technique has been recently proposed as an effective means of modeling embedded passives [49]. The augmentation method itself is based on circuit-partitioning or tearing scheme [55]. The technique followed in this paper is similar to the method outlined in [49], but the difference is in the lies the way augmentation elements are synthesized by selecting from a from a pre-designed SPICE-equivalent library, thus avoiding the explicit need for a causality and passivity check. The fundamental idea behind the approach is to find the perturbing element, which when introduced into the simple-lumped circuit model (S-LCM), closes the gap between the measured/electromagnetic solver results and the lumped circuit model. The augmentation approach has been previously demonstrated as an effective technique limited, in its choice of augmented nodes, to the ports of the S-LCM. The approach taken here affords augmentation at arbitrary nodes in the LCM, thus providing a means for faster convergence.

The technique is based on a modified nodal analysis (MNA) framework, wherein an electrical network is represented in a matrix equation form as

$$\mathbf{A}\mathbf{x} = \mathbf{B}\mathbf{v} \tag{89}$$

where, $\mathbf{A} \in C^{N \times N}$ is the MNA matrix, $\mathbf{x} \in C^{N \times 1}$ is the column vector containing the unknown variables, $\mathbf{B} \in R^{N \times m}$ is the binary selector matrix mapping the network port voltages to the MNA space, and $\mathbf{v} \in C^{N \times 1}$ contains the terminal voltages in the network. The algorithm works next by extracting Y-parameters from the (1) as

$$\mathbf{Y} = \mathbf{B}^T \mathbf{A}^{-1} \mathbf{B}. \tag{90}$$

The addition of an element added between two arbitrary nodes m and n, represented by z_{mn}^{AUG}, should minimize the difference between the extracted and target parameters. Therefore, an error function is defined in terms of the target Y-parameters and the updated LCM Y-parameters (after the inclusion of augmented element), as shown below

$$\epsilon = \left\| \mathbf{Y}_{target} - \mathbf{Y}' \right\| = \left\| \mathbf{Y}_{target} - \mathbf{B}^T \mathbf{A}'^{-1} \mathbf{B} \right\|. \tag{91}$$

where $\mathbf{Y}'$ and $\mathbf{A}'$ represent the admittance parameters and the MNA matrix with the inclusion of the augmentation element. Thus, by establishing a direct relation between the augmentation impedance z_{mn}^{AUG} and the error function the model is able to better represent the frequency response of the passive component , in each successive iteration.

A.2.1   Calculation of augmentation impedance

The augmentation impedance value is calculated as shown in [4] by calculating the open circuit voltage and then determining the change in MNA variable matrix x due to the introduction of an element between nodes m and n,

$$\Delta x = -textbf{A}^{-1} \xi \frac{\xi^T \mathbf{A}^{-1} \mathbf{B} \mathbf{v}}{z_{AUG} - \xi^T \mathbf{A}^{-1} \xi} \tag{92}$$

where ξ is a connection vector with values of +1 and -1 at its m_{th} and n_{th} row respectively, and zeros elsewhere in case of a shunt augmentation and it has a +1 in the mth row and zeros elsewhere in case of a series augmentation at the mth node, similar to introducing an inductive element in the MNA matrix [71].

The change in the Y parameters with the augmentation is given by the expression

$$\Delta \mathbf{Y} = \mathbf{B}^T \mathbf{A}^{-1} \xi (\xi^T \mathbf{A}^{-1} \mathbf{B}) \gamma_{AUG} \tag{93}$$

where γ_{AUG} is related to the augmentation impedance as

$$\gamma_{AUG} = z_{AUG} \xi^T \mathbf{A}^{-1} \xi \tag{94}$$

for the shunt augmentation, and

$$\gamma_{AUG}^{-1} = \xi^T \mathbf{A}^{-1} \xi z_{AUG}^{-1} \tag{95}$$

in case of series augmentation. Furthermore, for a 2-port network it can be derived that

$$\Delta \mathbf{Y} = \mathbf{B}^T \mathbf{A}^{-1} \xi_1 (\xi_1^T \mathbf{A}^{-1} \mathbf{B}) \gamma_{AUG}^1 + \mathbf{B}^T \mathbf{A}^{-1} \xi_2 (\xi_2^T \mathbf{A}^{-1} \mathbf{B}) \gamma_{AUG}^2 + \mathbf{B}^T \mathbf{A}^{-1} \xi_3 (\xi_3^T \mathbf{A}^{-1} \mathbf{B}) \gamma_{AUG}^3 \tag{96}$$

where γ_{AUG}^i represents the Γ_{AUG} column vector corresponding to the network parameters Y_{pq}, p, and q indexing the ports of the network. Since we are solving for a passive component, due to the symmetric nature of the network parameters, the number of augmentation elements that can be simultaneously solved for, is limited by the rank of the Y matrix.

The basic crux of the approach may be summarized in the following steps:

1. The SLCM and the target results serve as inputs.

2. A set of nodes are selected for augmentation

3. The type of augmentation is selected - series/shunt.

4. The augmentation impedance value is calculated.

5. The Y parameter matrix of the model is updated

6. The error criterion is checked. If it is not met, the process is repeated from step 1 with the new augmented model serving as the simple lumped circuit model.

117
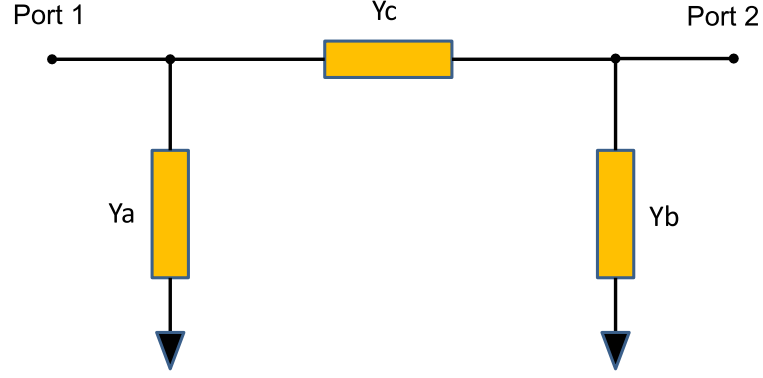
Figure 109: The inductance of the augmented equivalent circuit model of a multi-level embedded spiral inductor compared with that of the simulation.

A.2.2 Simple Lumped Element Model

To construct the augmented model of an embedded passive component, however, first the simple lumped element model needs to be constructed. A way to extract simple model from the network parameter data was shown in [41]. Consider the two port network shown in Fig. 109 with admittance elements Y_a, Y_b, and Y_c. For this network, the two port admittance parameters can be written as

$$Y_{11} = Y_a + Y_c, \tag{97a}$$

$$Y_{12} = Y_{21} = -Y_c, \tag{97b}$$

$$Y_{22} = Y_b + Y_c. \tag{97c}$$

Based on the above, the constitutive elements of the admittance parameters may be extracted easily. For example the inductive component,L_c, of Y_c can be extracted from measurement/simulation data as

$$L_c = \frac{imag(\frac{1}{Y_{21(meas)}})}{2\pi \times f} \tag{98}$$
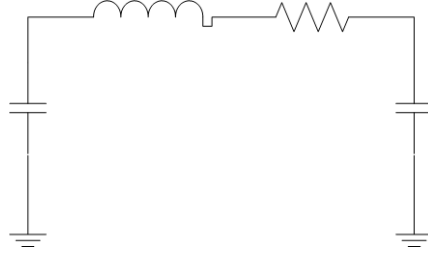
Figure 110: A simple equivalent circuit model of a spiral inductor.
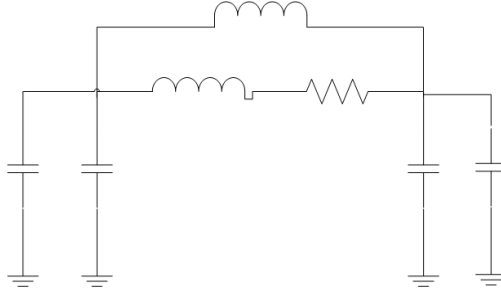
Figure 111: The augmented equivalent circuit model of an embedded spiral inductor.

where, f is the frequency of the measurement/simulation data, $Y_{21}(meas)$. Similarly the resistive component, R_c of Y_c is given as

$$R_c = real(\frac{1}{Y_{21}(meas)}) \tag{99}$$

The capacitive component of Y_a and Y_c are given as

$$C_a = \frac{imag(Y_{11}(meas) + Y_{21}(meas))}{2\pi \times f}, and \tag{100}$$

$$C_b = \frac{imag(Y_{22}(meas) + Y_{12}(meas))}{2\pi \times f}, \tag{101}$$

respectively. This approach can be easily modified to generate the one port lumped element model. Thus a simple equivalent model of any embedded passive component can be built.

119
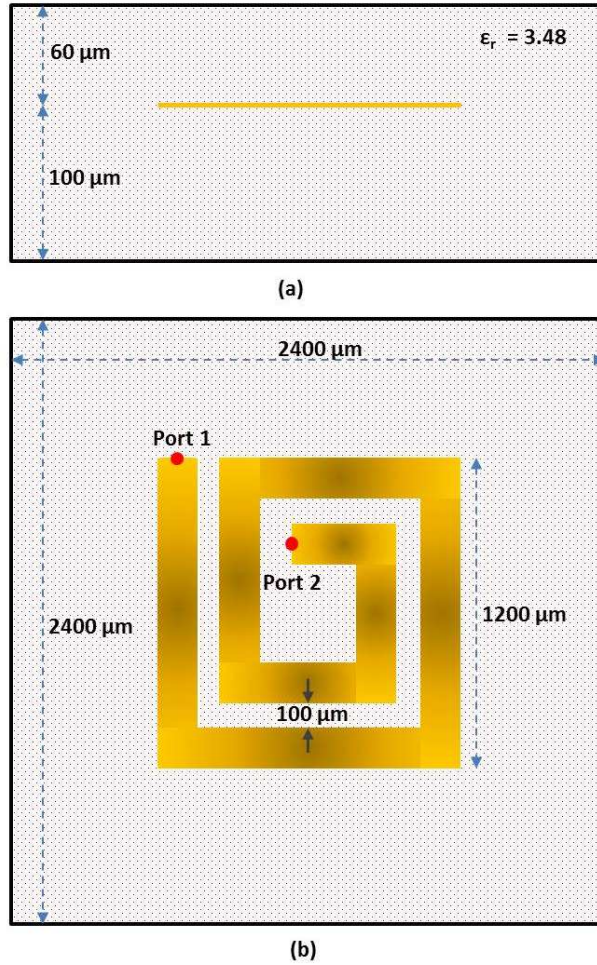
Figure 112: The layout of the embedded spiral inductor.

A.2.3 SEEC Model and Lumped Element Modeling

It is proposed that the augmentation approach described earlier in this chapter be combined with the SEEC model. This would then provide for a fast method characterizing an embedded passive component. As proof-of-concept, simulations of an embedded spiral inductor with a linewidth of 150 μm, as shown in Fig. 112, were carried out using the SEEC model. The plot of inductance in Fig. 113 shows an accurate match between the SEEC model and the lumped element model obtained through augmentation.

120
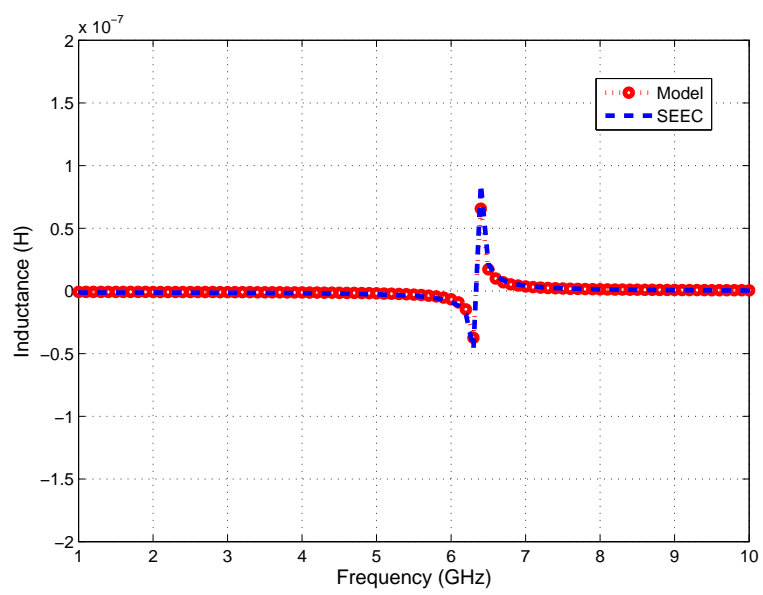
Figure 113: The inductance of the augmented equivalent circuit model of the embedded spiral inductor compared with that of the original SEEC model.

REFERENCES

[1] ACHAR, R. and NAKHLA, M., "Simulation of high-speed interconnects," *Proc.in IEEE*, vol. 89, no. 5, pp. 693–728, 2001.

[2] AHMADLOO, M. and DOUNAVIS, A., "Parameterized model order reduction of electromagnetic systems using multiorder arnoldi," *IEEE Trans. Advanced Packaging*, vol. 33, no. 4, pp. 1012–1020, 2010.

[3] BAI, Z. and SU, Y., "Dimension reduction of second-order dynamical systems via a second-order arnoldi method," *SIAM J. on Scientific Computing*, vol. 26, no. 9, pp. 1692–1709, 2005.

[4] BANERJEE, K. and MEHROTRA, A., "Analysis of on-chip inductance effects for distributed rlc interconnects," *IEEE Trans. Computer-Aided Design*, vol. 21, no. 8, pp. 904–915, 1997.

[5] BEATTIE, M. and PILEGGI, L., "Efficient inductance extraction via windowing," *Proc. Design Automation and Test in Europe*, pp. 430–436, 2001.

[6] BEGGS, J., LUEBBERS, R., YEE, K., and KUNZ, K., "Finite-difference time-domain implementation of surface impedance boundary conditions," *IEEE Trans. Antennas and Propagation*, vol. 40, pp. 49–56, 1992.

[7] BEKER, B., COKKINIDES, G., and TEMPLETON, A., "Analysis of microwave capacitors and ic packages," *IEEE Trans. Microwave Theory Tech.*, vol. 42, no. 9, pp. 1759–1764, 1994.

[8] B.YOUNG, *Digital Signal Integrity: Modeling and Simulation with Interconnects and Packages*. Prentice Hall PTR, 2000.

[9] CANGELLARIS, A., CELIK, M., PASHA, S., and ZHAO, L., "Electromagnetic model order reduction for system-level modeling," *IEEE Trans. Microwave Theory and Tech.*, vol. 47, no. 6, pp. 840–850, 1999.

[10] CHEN, C.-P. and WONG, D., "Error bounded pade approximation via bilinear conformal transformation," *Proc. of 36th Annual ACM/IEEE Design Automation Conference*, pp. 7–12, 1997.

[11] CHIPROUT, E. and NAKHLA, M. S., "Analysis of interconnect networks using complex frequency hopping," *IEEE Trans. Computer-Aided Design*, vol. 14, no. 8, pp. 186–200, 1995.

[12] CRADDOCK, I. J., RAILTON, C. J., and McGEEHAN, J. P., "Derivation and application of a passive equivalent circuit for the finite difference time domain algorithm," *IEEE Microwave and Guided Wave Lett.*, vol. 6, no. 1, pp. 40–42, 1996.

[13] DARVE, E., "The fast multipole method: Numerical implementation," *Journal of Computational Physics*, vol. 160, no. 1, pp. 195–240, 1997.

[14] DAVIS, J. A. and MEINDL, J. D., "Compact distributed rlc interconnect models - single line transient, time delay, and overshoot expressions," *IEEE Transactions on Electron Devices*, vol. 47, no. 11, pp. 2068–2077, 2000.

[15] DE MENEZES, L. and HOEFER, W., "Accuracy of tlm solutions of maxwell's equations," *IEEE Trans. Microwave Theory and Tech.*, vol. 44, no. 12, pp. 2512–2518, 2006.

[16] DEVGAN, A., JI, H., and DAI, W., "How to efficiently capture on-chip inductance effects: Introducing a new circuit element k," *Proc IEEE International Conference on Computer Aided Design*, pp. 150–155, Nov. 2000.

[17] DONEPUDI, K., JIN, J.-M., and CHEW, W. C., "A higher order multilevel fast multipole algorithm for scattering from mixed conducting/dielectric bodies," *IEEE Trans. on Antennas and Prop.*, vol. 51, no. 10, pp. 2814–2821, 2003.

[18] ENGIN, A. E., BHARATH, K., and SWAMINATHAN, M., "Multilayered finite-difference method (mfdm) for modeling of package and printed circuit board planes," *IEEE Trans. Electromagnetic Compatibility*, vol. 49, no. 2, pp. 441–447, 2007.

[19] FELDMANN, P. and FREUND, R. W., "Efficient linear circuit analysis by pade' approximation via the lanczos process," *IEEE Trans. Computer-Aided Design*, vol. 14, pp. 639–649, 1995.

[20] FREUND, W. R. and NACHTIGAL, N. M., "Qmr: A quasi-minimal residual method for non-hermitian linear systems," *SIAM Journal: Numer. Math.*, vol. 60, pp. 315–339, 1991.

[21] GAL, L., "On-chip crosstalkthe new signal integrity challenge," *Proc. CICC*, pp. 251–254, 1995.

[22] GALLIVAN, K., GRIMME, E., and DOOREN, P. V., "A rational lanczos method for model reduction," *Numerical Algorithms*, vol. 12, no. 8, pp. 33–63, 1996.

[23] GREENGARD, L. and ROKHLIN, V., "A new fdtd algorithm based on alternative direction implicit method," *J. Comput. Phys.*, vol. 73, pp. 325–348, 1987.

[24] GRIMME, E., *Krylov projection methods for model reduction*. PhD thesis, University of Illinois at Urbana-Champaign, 2007.

[25] HAN, K. J., SWAMINATHAN, M., and BANDYOPADHYAY, T., "Electromagnetic modeling of through-silicon via (tsv) interconnections using cylindrical modal basis functions," *IEEE Trans. Advanced Packaging*, vol. 33, no. 4, pp. 804–817, 2010.

[26] HARRINGTON, R. F., *Field Computation by Moment Methods*. Wiley-IEEE Press, 1993.

[27] HEEB, H., RUEHLI, A. E., BRACKEN, J. E., and ROHRER, R. A., "Three dimensional circuit oriented electromagnetic modeling for vlsi interconnects," *IEEE International Conf. on Computer Design*, vol. 17, no. 8, pp. 645–=653, 1992.

[28] HOEFER, W. J. R. and ITOH, E. T., *The transmission line matrix (TLM) method, in Numerical Techniques for Microwave and Millimeter Wave Passive Structures*. New York: Wiley, 1989.

[29] HOEFER, W., "The transmission-line matrix method–theory and applications," *IEEE Trans. Microwave Theory and Tech.*, vol. 33, no. 10, pp. 882–893, 1985.

[30] I.M.ELFADEL and LING, D., "A block rational arnoldi algorithm for multipoint passive model-order reduction of multiport rlc networks," *Proc. of IEEE/ACM International Conf. on Computer-Aided Design*, pp. 66–71, 1997.

[31] ISMAIL, Y., FRIEDMAN, E., and NEVES, J., "Equivalent elmore delay for rlc trees," *IEEE Trans. Computer-Aided Design*, vol. 19, pp. 83–97, Jan. 2000.

[32] JIN, J., *The Finite Element Method in Electromagnetics*. Wiley, 1993.

[33] KAHNG, A. B. and MUDDU, S., "An analytical delay model for rlc interconnects," *IEEE Trans. Computer-Aided Design*, vol. 16, no. 12, pp. 1507–1514, 1997.

[34] KAMON, M., TSUK, M. J., and WHITE, J., "Fasthenry: A multipole-accelerated 3-d inductance extraction program," *Proc. Design Automation Conference*, pp. 678–683, 1993.

[35] KAO, W., LO, C.-Y., BASEL, M., and SINGH, R., "Parasitic extraction: Current state of the art and future trends," *Proc. of IEEE*, vol. 89, pp. 729–739, May 2001.

[36] KECHROUD, R., SOULAIMANI, A., SAAD, Y., and GOWDA, S., "Preconditioning techniques for the solution of the helmholtz equation by the finite element method," *Mathematics and Computers in Simulation*, vol. 56, no. 4–5, pp. 303–321, 2004.

[37] KNOCKAERT, L. and ZUTTER, D. D., "Laguerre-svd reduced-order modeling," *IEEE Trans. on Microwave Theory Tech.*, vol. 48, no. 9, pp. 1469–1475, 2000.

[38] KULAS, L. and MROZOWSKI, M., "Reduced order models of refined yee's cells," *IEEE Microwav. Comp. and Lett.*, vol. 13, no. 4, pp. 164–166, 2003.

[39] LEE, S. and JIN, J., "Application of the tree-cotree splitting for improving matrix conditioning in the full-wave finite-element analysis of highspeed circuits," *Microwave Optical Technol. Lett.*, vol. 50, no. 6, pp. 1476–1481, 2008.

[40] MIN, S. H. and SWAMINATHAN, M., "Efficient construction of two-port passive macromodels for resonant networks," *IEEE Proc. of 10th Topical Meeting of Electrical Performance of Electronic Packaging*, pp. 229–232, 2001.

[41] MIN, S.-H., SEO, C.-S., LAPUSHIN, S., CARASTRO, L., DALMIA, S., WHITE, G., and SWAMINATHAN, M., "Parasitic-aware rf design via parameterization of embedded passives on multilayer organic substrates," *IEEE Proc. of Conf. on Electrical Performance of Electronic Packaging*, pp. 107–110, 2007.

[42] MONGA MADE, M. M., BEAUWENS, R., and WARZEE, G., "Preconditioning of discrete helmholtz operators perturbed by a diagonal complex matrix," *Communications in Numerical Methods in Engineering*, vol. 16, no. 11, pp. 801–817, 2000.

[43] NABORS, K. and WHITE, J., "Fastcap: A multipole accelerated 3d capacitance extraction program," *IEEE Trans. Computer-Aided Design*, vol. 10, pp. 1447–1459, 1991.

[44] NAMIKI, T., "A new fdtd algorithm based on alternative direction implicit method," *IEEE Trans. Microwave Theory Tech.*, vol. 47, pp. 2003–2007, Aug. 1999.

[45] NAMIKI, T. and ITO, K., "Accuracy improvement technique applied to non-uniform fdtd cells using high-order implicit scheme," *Proc. of IEEE Antennas and Propagation Society International Symposium*, vol. 1, pp. 56–59, 2001.

[46] NARAYANAN, T. V., MIN, S.-H., and SWAMINATHAN, M., "Nodal order reduction via bilinear conformal transformation," *Proc. of IEEE 14th Wkshp. on Signal Propagation on Interconnects*, pp. 73–76, 2010.

[47] NARAYANAN, T. V., MIN, S.-H., and M., S., "Accelerated frequency domain analysis by susceptance-element based model order reduction of 3d full-wave equations," *Proc. of IEEE 18th Conference on Electrical Performance of Electronic Packaging and Systems*, pp. 141–144, 2009.

[48] ODABASIOGLU, A., CELIK, M., and PILEGGI, L., "Prima: passive reduced order interconnect macromodeling algorithm," *IEEE Trans. Computer-Aided Design*, vol. 17, no. 8, pp. 645–653, 1998.

[49] PAUL, D., NAKHLA, M. S., ACHAR, R., and WEISSHAAR, A., "A passive algorithm for modeling frequency-dependent parameters of coupled interconnects,"

IEEE Proc. of 10th Topical Meeting of Electrical Performance of Electronic Packaging, pp. 185–188, 2006.

[50] PHILLIPS, J. R., CHIPROUT, E., and LING, D. D., "Efficient full-wave electromagnetic analysis via model-order reduction of fast integral transforms," *Proc. of 33rd ACM/IEEE Design Automation Conference*, pp. 377–382, June 1996.

[51] PHILLIPS, J., DANIEL, L., and SILVEIRA, L. M., "Guaranteed passive balancing transformations for model order reduction," *Proc. of 39th Design Automation Conference*, pp. 52–57, 2002.

[52] PHILLIPS, J., DANIEL, L., and SILVEIRA, L., "Guaranteed passive balancing transformations for model order reduction," *IEEE Trans. Computer-Aided Design*, vol. 22, no. 8, pp. 1027–1041, 2003.

[53] PIERANTONI, L., TOMASSONI, C., and ROZZI, T., "A new termination condition for the application of the tlm method to discontinuity problems in closed homogeneous waveguide," *IEEE Trans. Microwave Theory and Tech.*, vol. 50, no. 11, pp. 2513–2518, 2002.

[54] PILLAGE, L. T. and ROHRER, R. A., "Asymptotic waveform evaluation for timing analysis," *IEEE Trans. Computer-Aided Design*, vol. 9, pp. 352–366, 1990.

[55] ROHRER, R. A., "Circuit partitioning simplified," *IEEE Trans. Circuits and Systems*, vol. 35, no. 1, pp. 2–5, 2002.

[56] RUEHLI, A. E. and CANGELLARIS, A. C., "Progress in the methodologies for the electrical modeling of interconnects and electronic packages," *Proceedings of the IEEE*, vol. 89, no. 5, pp. 740–771, 2001.

[57] RUEHLI, A., "Equivalent circuit models for three dimensional multiconductor systems," *IEEE Trans. Microwave Theory and Tech.*, vol. 22, pp. 216–221, 1974.

[58] SAAD, Y. and SCHULTZ, M. H., "Gmres: A generalized minimal residual algorithm for solving nonsymmetric linear systems," *SIAM J. Sci. Stat. Comput.*, July 1986.

[59] SAKURAI, T., "Closed-form expressions for interconnection delay, coupling, and crosstalk in vlsis," *IEEE Trans. Electron. Devices*, vol. 40, pp. 118–124, 1993.

[60] SHEEHAN, B. N., "Enor: model order reduction of rlc circuits using nodal equations for efficient factorization," *Proc. of 36th Annual ACM/IEEE Design Automation Conference*, pp. 17–21, 1999.

[61] SILVEIRA, M., KAMON, M., ELFADEL, I., and WHITE, J., "A coordinate-transformed arnoldi algorithm for generating guaranteed stable reduced-order models of rlc circuits," *Proc. of 33rd Annual ACM/IEEE Design Automation Conference*, pp. 288–294, 1996.

[62] Song, J., Lu, C.-C., and Chew, W. C., "Multilevel fast multipole algorithm for electromagnetic scattering by large complex objects," *IEEE Trans. on Antennas and Prop.*, vol. 45, no. 10, pp. 1488–1493, 1997.

[63] Srinivasan, K., Yadav, P., A.E., E., M., S., and Ha, M., "Fast em/circuit transient simulation using laguerre equivalent circuit (sleec)," *IEEE Trans. Electromagnetic Compatibility*, vol. 51, no. 3, pp. 756–762, 2009.

[64] Sullivan, D. M., "Exceeding the courant condition with the fdtd method," *IEEE Microwave and Guided Wave Lett.*, vol. 6, no. 8, pp. 289–291, 1996.

[65] Sun, D.-K., Lee, J.-F., and Cendes, Z., "Alps-a new fast frequency-sweep procedure for microwave devices," *IEEE Trans. Microwave Theory and Tech.*, vol. 49, no. 2, pp. 398–402, 2001.

[66] Swaminathan, M. and Engin, E., *Power integrity modeling and design for semiconductors and systems.* Prentice Hall PTR, 2007. 1st ed.

[67] Sylvester, D. and Hu, C., "Analytical modeling and characterization of deep submicrometer interconnect," *Proc. of IEEE*, vol. 89, pp. 634–664, 2001.

[68] Taflove, A. and Hagness, S. C., *Computational electrodynamics: The finite-difference time-domain method.* Artech House, 2000.

[69] Triverio, P., Grivet-Talocia, S., Nakhl, M., Canavero, F., and Achar, R., "Stability, causality, and passivity in electrical interconnect models," *IEEE Trans. on Advanced Packaging*, vol. 30, no. 4, pp. 795–808, 2007.

[70] Tutuianu, B., Dartu, F., and Pileggi, L., "An explicit rc-circuit delay approximation based on the first three moments of the impulse response," *Proc. of 33rd ACM/IEEE Design Automation Conference*, vol. 89, pp. 611–616, June 1996.

[71] Vlach, J. and Singhal, K., *Computer methods for circuit analysis and design.* New York: Van Nostrand Reinhold, 1983. 1st ed.

[72] White, M. J., Iskander, M. F., and Huang, Z., "Development of a multigrid fdtd code for three-dimensional applications," *IEEE Trans. Antennas and Prop.*, vol. 45, no. 10, pp. 1512–1517, 1997.

[73] White, M. J., Yun, Z., and Iskander, M. F., "A new 3d fdtd multigrid technique with dielectric traverse capabilities," *IEEE Trans. Microwave Theory and Tech.*, vol. 49, no. 3, pp. 422–430, 2001.

[74] Wu, D. and Chen, J., "Application of model order reduction techniques to compact fdfd method for guided wave structures," *IEEE Antennas and Propagation Society International Symposium*, vol. 2, pp. 636–639, 2003.

[75] Wu, H., Cangellaris, A., and Kuo, A.-Y., "Application of domain decomposition to the finite-element electromagnetic modeling of planar multi-layered interconnect structures and integrated passives," *Proc. of IEEE Conf. on Electrical Performance of Electronic Packaging*, pp. 281–284, 2004.

[76] Wu, H. and Cangellaris, A. C., "Model-order reduction of finite-element approximations of passive electromagnetic devices including lumped electrical-circuit models," *IEEE Trans. Microwave Theory and Tech.*, vol. 52, no. 9, pp. 2305–2312, 2004.

[77] Xu, F., Wu, K., and Hong, W., "Domain decomposition fdtd algorithm combined with numerical tl calibration technique and its application in parameter extraction of substrate integrated circuits," *IEEE Trans. Microwave Theory and Tech.*, vol. 54, no. 1, pp. 329–338, 2006.

[78] Yee, K. S., "Numerical solution of initial boundary value problems involving maxwell's equations in isotropic media," *IEEE Trans. on Antennas and Propagation*, vol. 17, pp. 585–589, 1996.

[79] Zheng, H., Krauter, B., Beattie, M., and Pileggi, L., "Window-based susceptance models for large-scale rlc circuit analyses," *Proc. Design Automation and Test in Europe*, pp. 628–633, 2002.

[80] Zheng, H. and Pileggi, L., "Robust and passive model order reduction for circuits containing susceptance elements," *Proc. of IEEE/ACM International Conf. on Computer-Aided Design*, pp. 761–766, 2002.

[81] Zhu, J. and Jiao, D., "A theoretically rigorous full-wave finite-element-based solution of maxwell's equations from dc to high frequencies," *IEEE Trans. Advanced Packaging*, vol. 33, no. 4, pp. 1043–1050, 2010.

VITA

Narayanan T.V. was born in Ghatshila, Jharkhand (then Bihar) and did his schooling in Kendriya Vidalayas - Surda (in Ghatshila) and Ballygunj (in Kolkata). He completed his Bachelors in Electrical and Electronic Engineering from Sri Venkateswara College of Engineering, University of Madras. He then completed a Master of Science in Advanced Materials for Micro- and Nano- Systems in Singapore-MIT Alliance. During this time, he completed his Masters project in Institute of Microelectronics, Singapore. After working as a Research Associate with the Singapore-MIT Alliance Innovation in Manufacturing Science and Technology program, he joined doctoral studies in the School of Electrical and Computer Engineering at Georgia Institute of Technology. After graduation, he will join Intel as a Packaging Engineer.